MESOSCOPIC CORRELATION WITHIN TRANSMITTED SPECKLE PATTERN AND WAVE LOCALIZATION

by

Bing Hu

A dissertation submitted to the Graduate Faculty in Physics in partial fulfillment of the requirements for the degree of Doctor of Philosophy, The City University of New York

2006

INFORMATION TO USERS

The quality of this reproduction is dependent upon the quality of the copy submitted. Broken or indistinct print, colored or poor quality illustrations and photographs, print bleed-through, substandard margins, and improper alignment can adversely affect reproduction.

In the unlikely event that the author did not send a complete manuscript and there are missing pages, these will be noted. Also, if unauthorized copyright material had to be removed, a note will indicate the deletion.

ProQuest Information and Learning Company
300 North Zeeb Road
P.O. Box 1346
Ann Arbor, MI 48106-1346

This manuscript has been read and accepted for the
Graduate Faculty in Physics in satisfaction of the
dissertation requirement for the degree of Doctor of Philosophy.

Prof. Azriel Genack

Date — Chair of Examining Committee

Prof. Sultan Catto

Date — Executive Officer

Prof. Alexander Lisyansky

Dr. Lev Deych

Dr. Victor Kopp

Dr. Vinod Menon

Supervision Committee

THE CITY UNIVERSITY OF NEW YORK

Abstract

Mesoscopic Correlation in Transmitted Speckle Pattern and Wave Localization

by

Bing Hu

Advisor: Professor Azriel Z. Genack

This thesis is an experimental study of the statistical character of the field distribution within one-dimensional and transmitted through quasi-1D random samples.

We measured the spatial extent of the field for extended, evanescent, and localized wave in random single-mode waveguide. We find that spectrally and spatially overlapping modes in a nominally localized region of an open dissipative system can be decomposed into quasi-normal-modes.

Microwave field measurements of the near-field transmitted speckle pattern through random quasi-one-dimensional samples were carried out with polarization rotation, along a line, on a tight grid covering the full output surface. The field spectrum is Fourier transformed to give the temporal evolution of the speckle pattern. Field and intensity correlation versus displacement, frequency shift, and polarization rotation were studied to exhibit

the growing impact of mesoscopic fluctuation and photon localization with time delay from a exciting pulse. The variation of key distributions and correlation functions with delay time were examined. We find a universal expression for the intensity correlation function which is valid for localized and diffusive waves in steady-state and in the time domain. It is a function only of the field correlation function which is the same in steady state and in the time domain and the degree of correlation, κ, which also indicates the closeness of the random system to the localization transition. We also studied the microstatistics of the transmitted field in individual sample realizations, as opposed to the traditional focus on fluctuations relative to the ensemble average. We find that the field distribution in each configuration is Gaussian and that mesoscopic correlation arises as a result of fluctuation of the total transmission. The degree of correlation κ is just the variance of total transmission normalized by its ensemble average.

Other aspects on phase statistics of the speckle pattern are also reported. The distributions and correlations of phase, the first spatial derivation of the phase, and the transverse current density, which may be expressed as the product of the intensity and the first spatial derivative of phase, are all determined by a parameter derived from spatial correlation function of the field.

ACKNOWLEDGMENTS

First and foremost, I am deeply indebted to my supervisor, Professor Azriel Z. Genack from Queens College of CUNY, whose insight of the problem, encouragement and stimulating suggestions helped me in all the time of research and writing of this thesis.

I would like to express my gratitude to Dr. Patrick Sebbah and Dr. Andrey Chabanov for their great contribution to parts of works present in this thesis and lots of valuable discussion I had with them during the course of research. Also thank Dr. Victor Kopp for providing the nice software for 1D simulation and patiently making changes on my request. I wish to thank Dr. Jerome Klosner for long time discussion and keep asking detailed question throughout the work. I also want to thank Dr. Bart van Tiggelen from CNRS/ University of Joseph Fourier and Professor Gabriel Cwilich from Yeshiva University for their theoretical supports and numerical calculation for some results in Chapter 5.

I would like to thank Professor Alexander Lisyansky, Dr. Lev Deych, Dr. Vinod Menon, and Dr. Victor Kopp for having served in my thesis supervisory committee. A special thanks goes to Prof. Melvin Lax for his valuable advices and for being my committee member on my second exam.

The technical assistance on machinery and electronics I received from Howard, Ziggy, Bob, Yelfim, and Gregory are gratefully acknowledged here.

At this point, I am grateful to my husband Kungang for the inspiration support he provided throughout my research work and his fully understanding during a long period of separation. I would also extend my appreciation to my friends, who are always there whenever I need help.

Finally, I want express my appreciation to my parents and my to-be-born baby who are my sources of strength.

TABLE OF CONTENTS

LIST OF FIGURES

CHAPTER 1

INTRODUCTION

1.1 General Introduction

Classical and quantum mechanical waves are used to transmit energy and information and to control, probe and image our environment. Wave propagation in diverse complex media, either natural or manmade, such as electronic and photonic devices, metamaterials fabricated to highlight the characteristics of the wave interaction with structural elements on the scale of the wavelength, is therefore of fundamental and applied interest. The particularities of wave interactions between different type of wave and different systems are the basis of our rich experience of the world, but their common characteristics provide a framework for understanding transport and often point to new applications.

The study of classical wave transport in random [1-5] and periodic [6-9] media has been stimulated by the analogies [10] between electron localization [11-13], universal conductance fluctuations in conductors [14-18], and forbidden band gaps in semiconductors and insulators. A wave in a random medium may

follow innumerable trajectories with a wide distribution of path length called partial waves. Some trajectories encompass the pairs of time-reversal closed loops that return to the same coherence volume within the sample. A coherence volume inside the medium is $V_c \sim(\lambda/2)^3$. As a result of constructive interference between trajectories with closed loops, the return probability is enhanced leading to a narrow cone in backscattered light [19]. This effect is called weak localization effect [20-24]. In the weak scattering limit, weak localization is small and average transport can be well described by the diffusion equation for intensity, which corresponds to the random walk model of photons. In strong scattering samples, weak localization modifies average transport and eventually leads to the breakdown of diffusion and to Anderson localization. Localization in three-dimensions occurs when the Ioffe-Regel criterion [25] is fullfilled $k\ell \leq 1$, , where ℓ is transport mean free path in which the wave direction is totally randomized. Thus, weak localization is the precursor of Anderson localization. Both weak localization and Anderson localization are known as "mesoscopic" [26,27], indicating the multiple-scattered wave is temporally coherent through the static sample. This condition can be achieved at ultra-low temperatures in electronic samples with dimensions intermediate between the microscopic atomic size comparable to the wavelength and the macroscopic size of everyday objects. In contrast, classical waves are ordinarily coherent on the time scale in which the wave traverses

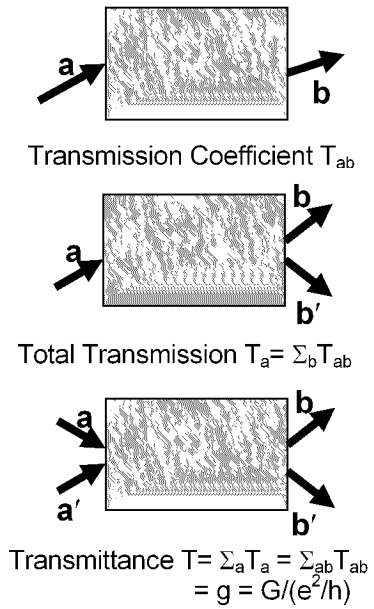

Fig. 1-1: Illustration of three principle transmission quantities

the sample. Unlike electronic systems, in which the only measurable quantity is the conductance, a variety of local and spatially averaged parameters can be studied for classical waves. Three principle transmission quantities that can be measured are shown in Fig.1-1. T_{ab} is the transmission coefficient of an outgoing channel *b* with respect to an incoming channel *a*. Summing over all outgoing channels gives the total transmission T_a. Further summing over all incoming channels gives the transmittance, which is associated with the dimensionless conductance *g* in electron system by Landauer formula [28],

$$g = G/(e^2/h) = \sum_{a,b} < T_{ab} > = \sum_{a} < T_a > = < T > . \quad (1\text{-}1)$$

The existence of interference between waves containing time-reversal loop trajectories results in long-range correlation [29,30] of intensity with frequency shift, spatial displacement or polarization rotation. This leads to dramatically enhanced fluctuations in the total transmission and transmittance even in weak scattering samples.

From the experimental point of view, optical [19,31,32] and microwave [33,34] measurements in disordered systems have been fruitful because of the high spatial, spectral and temporal resolution that can be obtained in collections of statistically equivalent samples. Interference between multiple scattered waves gives rise to the granular intensity variation on output boundary, known as the "speckle pattern". Just as the bright-dark line pattern gives the slit width and distance between slits in Young's double-slit experiment of wave interference, the speckle pattern is a finger print of a particular realization of the random sample though uncovering the sample structure remains a formidable challenge. However, the statistical study on a random ensemble of speckle patterns and microstatistics performed on a single speckle pattern, leads to a better understanding of statistical aspects of wave transport in random samples.

This thesis investigates the microstatistics of single sample realizations and the statistics for random ensembles. The impact of weak localization on the statistics of both static and dynamic transport properties will be examined

for single-channel transmission and total transmission. Our goal is to make the link between mesoscopic fluctuation and correlation on the one hand and photon localization on the other. We measured the microwave field on the output surface of quasi-1D random samples to gain a deeper insight into localization and correlation. In the quasi-1D geometry the transverse size W is much smaller than the sample length L (W<<L). The structure of spatial intensity correlation within the transmitted speckle pattern is determined experimentally. We find that the spatial intensity correlation can be expressed as a sum of terms which are either multiplicative, additive, or constant with respect to complex square of the field correlation function with displacement of the source and detector. When the source is fixed the intensity correlation function can be expressed in terms of the field correlation function and a single parameter κ, the degree of correlation which equals the value of intensity correlation function at points at which field correlation vanishes. We find that $\kappa = 2/3g$, where g is the dimensionless conductance in the absence of absorption. However, the measured transmittance by itself no longer indicates the closeness to the localization threshold, but κ still serves as a localization parameter in both steady state and the time domain. Non-local intensity correlation, as well as the fluctuation of total transmission, may be described in terms of a parameter that gives the closeness to the threshold of the Anderson localization transition. When localization occurs, waves are trapped

within a finite region with intensity exponentially decaying away from the region. Though absorption is ubiquitous it is often neglected in theoretical studies. By examining transport as a function of time following pulsed excitation, the affect of absorption can be removed while the growing impact of localization can be clearly discerned. We obtain the pulse response respect to an incident Gaussian pulse from our steady-state measurements of field spectra measurements by Fourier transforming the product of a Gaussian envelope and the measured spectrum. We find that the functional forms of the probability distributions of intensity and total transmission, and of the intensity correlation functions in the time domain are the same as found in the frequency domain.

Localization is directly reflected by the spatial extent of the wave. We have carried out measurements of the field spectrum at points along the entire length of a sample constructed by randomly juxtaposing dielectric slabs within a single-mode waveguide. This allows us to distinguish the extended, evanescent, localized waves as well as to discover the underlying modes which overlap in space and frequency. The overlapped modes can be decomposed into several quasi-normal modes and enhance the transmission particularly in the presence of absorption. This work allows us explore the nature of modes in open dissipative system.

1.2 Signatures of photon localization

The wave character of electron is neglected in classical electron transport theory in metals and semiconductors. In general, it is reasonable to disregarding the interference effect since the typical coherence length of an electron, which is around 10nm at room temperature, is much smaller than the typical size of electronic system [1]. Indeed classical transport theory may fail completely when the conductor is cooled down to the low enough temperature (~1K). Since the electron wave is dephased by thermally activated inelastic processes, lowering the temperature below 1K freezes out inelastic collisions so that the phase coherence length can reach the scale of several microns. Electronic systems of size comparable to the phase coherence length are called mesoscopic since they are in size intermediate between the microscopic and the macroscopic. In the mesoscopic regime, interference leads to large fluctuations that do not self-averaged. In strongly scattering samples, Ohm's law may fail and electron transport may be suppressed by weak localization. We will give a brief review of wave localization below.

In 1958, Anderson proposed that electrons can be localized by sufficiently strong disorder. Electrons are trapped by quantum interference. When Anderson localization occurs, the diffusion coefficient drops to zero and conductance vanishes. This explains the metal-insulator transition in semiconductors. However, it was not until the mid 1980s the Anderson

localization of classical waves became an attractive field based on the common wave nature of electrons and electromagnetic (EM) radiation. Because of the differences between photons and electrons, this posed entirely new experimental and theoretical challenges for finding convincing evidence of localization, and for investigating the characteristics of the transition from diffusive to localized waves. Many new EM phenomena were introduced such as weak localization, short- and long-range intensity correlation, and strong localization. And many experiments excited great interest in the localization of photons such as the coherent backscattering of light, microwave transmission measurement in quasi-1D and 3D system, optical transmission measurements in slabs, and lasing in random media.

In unbounded three-dimensional random systems, Anderson localization is predicted to occur where Ioffe-Regal criterion [25], $k\ell \sim 1$ is satisfied, where $k=2\pi/\lambda$ is the wave number and ℓ is the transport mean free path. The diffusion constant approaches zero at the localization threshold in large samples. For real systems, the sample length L and cross sectional area A are of importance. Three key indicators of localization are the Thouless number [13], the dimensionless conductance g, and the variance of total transmission [35] with a single incident channel. The relationship between these

parameters and the explicit connection between mesoscopic fluctuations and localization described below.

The Thouless number, δ [13], is the ratio of the average linewidth and line space between energy states, which can be written as $\delta=\delta E/\Delta E$ where ΔE is inverse of the density of states, in electron system energy spectra. For classical wave transport, δ is the ratio of the spectral width and spacing of quasi-states in the random medium, $\delta = \delta\nu/\Delta\nu$. The linewidth $\delta\nu$ in the absence of absorption and dephasing is due to leakage through the boundary. When $\delta<1$, $\delta\nu < \Delta\nu$, the poor spectral overlap of quasimodes from different spatial regions of the sample suppresses the transport and waves becomes localized in space. When $\delta>1$, quasimodes overlap spectrally and transport is uninhibited. Therefore, $\delta\sim1$ gives the threshold of localization in the absence of absorption. For electron systems, the direct proportionality relation between the conductivity and the diffusion coefficient is known as the "Einstein relation", $\sigma = \frac{e^2}{h} Dn(\nu)$ where $n(\nu)=(dn/d\nu) =(dN/d\nu)/AL$ is the density of states (DOS) per unit volume and frequency shift at frequency ν, and D is the diffusion coefficient. The conductance can then be written as $G= \sigma A/L= (e^2/h) Dn(\nu)A/L$. For weak scattering, the linewidth of the state corresponds to the width of the field correlation function with frequency shift [36] and is given as

$\delta\nu = D/L^2$ [13] . The line spacing is the inverse of the density of states of the sample as a whole, and may be written as $\Delta\nu = 1/(n(\nu)AL)$. The equality of the dimensionless conductance g and the Thouless number δ in absence of absorption can be seen from the follows: $g \equiv G/(e^2/h) = Dn(\nu)A/L = \delta\nu/\Delta\nu = \delta$. The average over an ensemble of statistically equivalent samples of the conductance $\langle g \rangle$, where $\langle \ldots \rangle$ represents the average over an ensemble, act as a scaling parameter [11,37] of the localization transition. In the weak scattering limit in the absence of absorption, the variance of relative fluctuations of the total transmission normalized by its ensemble average for an incident wave a, $var(s_a)$, is inversely proportional to the average value of the dimensionless conductance g [30,35,38-40], $var(s_a) = 2/3g$. In this thesis, the study of the structure of field and intensity correlation in quasi-1D random sample introduces the degree of correlation κ, which is the fractional correlation of fluctuations in intensity at points at which the field correlation function vanishes. Fluctuation of total transmission $var(s_a)$ and the degree of correlation are directly linked, $\kappa = var(s_a)$ [41-44]. The localization transition between waves that extend throughout the sample and waves that are exponentially peaked within it occurs at $g \sim 1$. And the probability distribution of total transmission may be expressed in terms of a single parameter g in the absence of inelastic scattering. How does the absorption change the picture? The explicit

connection between mesoscopic statistics and average transport via the parameter g breaks down in the presence of absorption. Indeed, g can no longer serve as a localization parameter in absorbing samples since its value decreases with increasing absorption, while the wave, if anything, is more removed from the localization transition since the contribution of waves follows longer trajectories in which the trajectories are more likely to cross is reduced. However, $var(s_a)$ is relatively insensitive to absorption, and may still serve as a localization parameter. Microwave experimental studies in quasi-1D samples show that the probability distribution of transmission depends only on the variance of total transmission normalized by its ensemble average, $var(s_a)$ [40, 35].

1.3 Speckle pattern through random medium

1.3.1 Spatial correlation of intensity in speckle pattern

Since the invention of the laser as the coherent light source in early the 1960s, there has been growing interest in the speckle pattern. The speckle patterns in transmission or reflection show large spatial intensity fluctuations. The transmitted speckle is the main concern of this thesis. The short-range correlation of intensity is seen in the bright spots of speckle pattern with size the order of the wavelength. The probability distribution of intensity follows the Rayleigh statistics [2,45] when localization effects can be neglected. The

distribution for a single polarization component of intensity is a negative exponential. With increasing scattering strength or sample length, interference between waves following time reversal looped path cannot be neglected. This leads to the deviations from the diffusion model in the suppressed average transport and enhanced long-range correlations. The intensity probability distribution deviates from Rayleigh statistics. This thesis focuses on long-range spatial correlation in steady state wave transport and its dynamics, which is beyond the diffusion approach.

In field the factorization approximation, the theoretical expression of the spatial intensity correlation function inside a random sample is $C(\Delta x) = (\sin k\Delta x/k\Delta x)^2 e^{-\Delta x/l}$ [46], where k is the wave number, l the mean free path, and Δx the spatial displacement. Later Freund derived the spatial intensity correlation function on the output surface [47]. Indeed this intensity correlation in the field factorization approximation exponentially decays on the scale of the mean free path and vanishes in short distance, so called short-range intensity correlation but there are other terms. Stephen and Cwilich [48] considered long-range correlation in intensity by including mesoscopic corrections. This approach gives rise to enhanced fluctuations on the total transmission. Microwave measurements found long-range correlation in the intensity with spectral, spatial or temporal shift. Feng *et al.* expanded the intensity correlation in three terms in terms of the parameter $(1/g)$, $C = C_1 + C_2$

+ C_3 [29]. The C_1 term is short-range and is seen in the scale of speckle spot. The C_2 term decays slower and has a magnitude is proportional to $(1/g)$. The C_3 term is proportional to $(1/g)^2$. Long-range correlation can be explicitly related to the variations of total transmission with frequency and sample configuration. The C_3 term is the optical analog of universal conductance fluctuation in electron transport due to the quantum interference.

This thesis reports the experimental study of the structure of intensity correlation with the coordinate shift and gives a more complete expression based on a simple functional form, which involves the field correlation function. By unscrambling the intensity spatial correlation in the time-domain, we find the time dependence of κ. The short-range correlation function is invariant with time. The measurement of the full speckle patterns through random samples gives a map of key wave aspects including intensity, phase, phase singularities, and 2D polarization singularities.

1.3.2 Observations of full speckle pattern map

We have measured the near field transmitted speckle pattern through random sample for two perpendicular polarizations. The random quasi-1D sample consists of randomly mixed 1.27-cm-diam polystyrene spheres. The detector is a 100 micron diameter and 4-mm-long antenna mounted on a four-dimensional motion stage includes X-Y-Z 3D translation stage. The Arrick

Robotic stage has two MD2 dual step motor controllers, and one Hurst rotation step motor controlled by the bi-polar stepping Motor Control board. The stepping motors have 0.9^{o} angular step to give a spatial resolution 0.05mm. The different orientations of the detector couple to various polarization components of the wave. The length of the detector should be sufficient to pick up different polarization waves, as well as to obtain sufficient coupling strength, but short enough to have low spatial resolution along the x and y direction due to the detector orientation. This setup allows us to achieve the speckle pattern measurements by moving the detector along x-y plane parallel to the sample output surface with 1mm spacing mesh to cover the entire79-mm-diameter tube cross section and rotating the orientation of detector 90 degree back and forth. The alignment of the detector is crucial for making sure the distant from the sample surface is constant. The frequency range 16.8 – 17.8 GHz is swept with 625 kHz resolution by using vector network analyzer for each spatial point and each polarization.

The 2D maps of intensity and phase within $[-\pi, \pi]$ of the field are shown in Fig. 1-2. The phase map (right) reveals the striking feature of the topological singularities by means of the invalidation of some quantities used to describe the complex field pattern. The phase singularities, also called topological charges, dislocations, or optical vertices, are points at which the phase is ill-defined since both the real and imaginary parts of the field

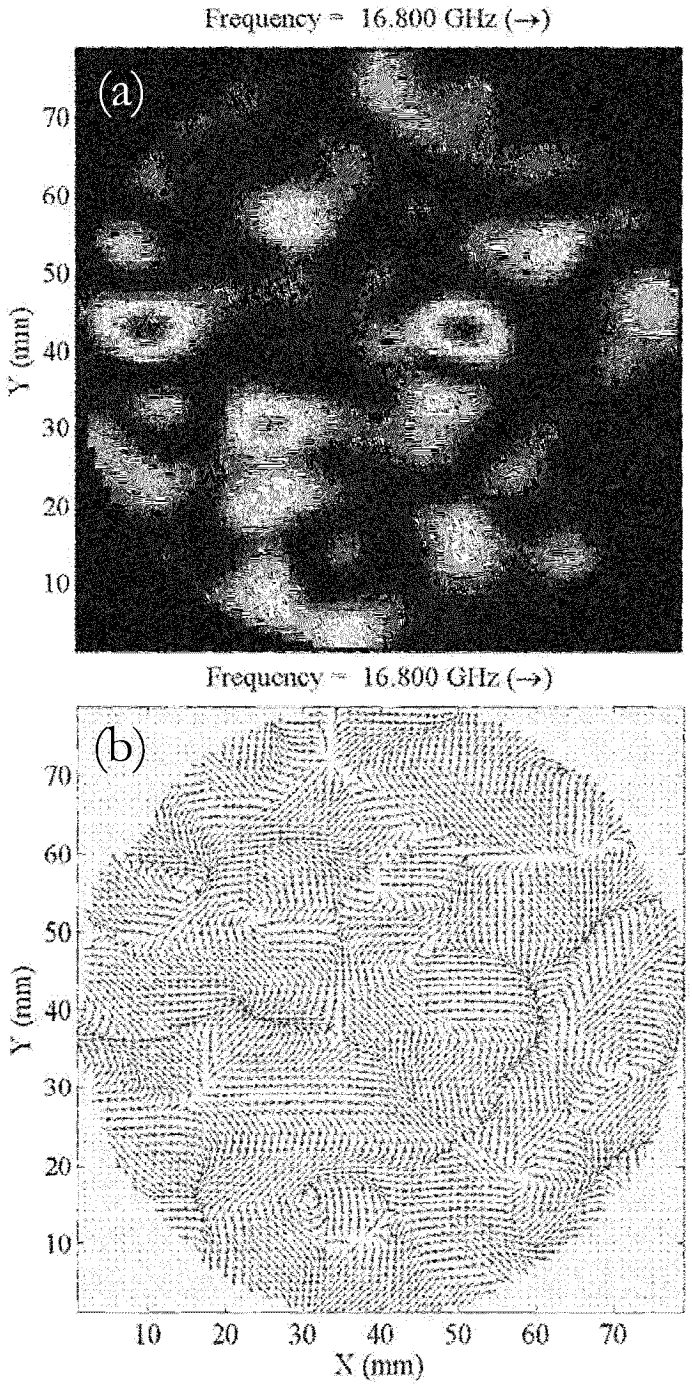

Fig. 1-2: Two-dimensional map of intensities obtained by squaring the amplitudes (a) and phase (b) of measured microwave fields for one polarizations component and single frequency.

Later in this section, we will also show the other type of singularity, polarization singularities indicate the vanishing of the polarization ellipse. We searched the 2D field maps for points at which the zero contours of real and imaginary part of field cross to precisely locate the positions of phase singularities in each speckle pattern. It is noteworthy that apparently disparate zeros of real and imaginary parts of the field in the two-dimensional plane are

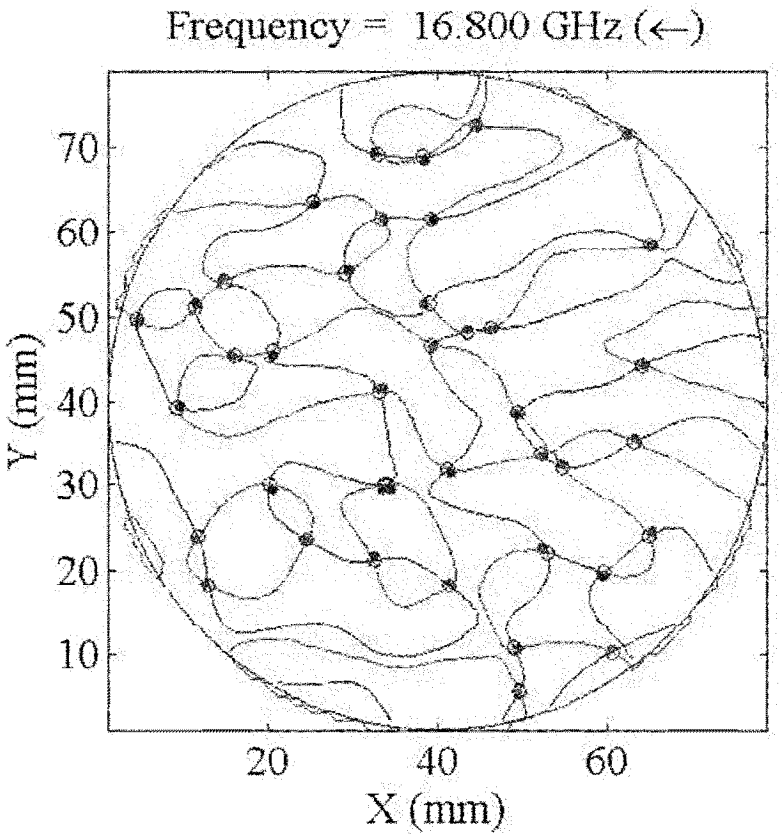

Figure 1-3: Positions and sign of phase singularities in speckle pattern of single polarization component and single frequency. Blue and red curves are zero contours for real and imaginary parts of field. Blue and red dots are positive and negative phase singularities or topological charge.

indeed continuous in three-dimensions. In terms of topological charge, $Q \equiv \frac{1}{2\pi} \oint_c < \phi < d\vec{l}$, where ϕ is the local phase, and the line integral is taken over the path on the close curve *c*. Phase change around a given phase singularity is ±2π, where the sign gives either positive or negative topological charge corresponding to the phase increase clockwise or counterclockwise. Fig. 1-3 shows the positions of positive and negative phase singularities within the single speckle pattern.

The full description of the electromagnetic field should consider its vector character. Chapter 4 deals with polarization correlation. The intensity correlation between wave fields with perpendicular polarizations reveals the mesoscopic correlation in the system. As a result of random phasor in the wave superposition of the field at a specific position and component of linear polarization, each spatial point has its own degree of elliptical polarization, which is given by the polarization ellipse. Two parameters are used to describe the polarization ellipse at each point, the angle between the longer semi-axis of the ellipse and the x-axis θ and the eccentricity *e*, defined as the ratio of the two semi-axis. A plot of the polarization ellipses in the two-dimensional plane of near-field speckle pattern respect is shown in Fig. 1-4.

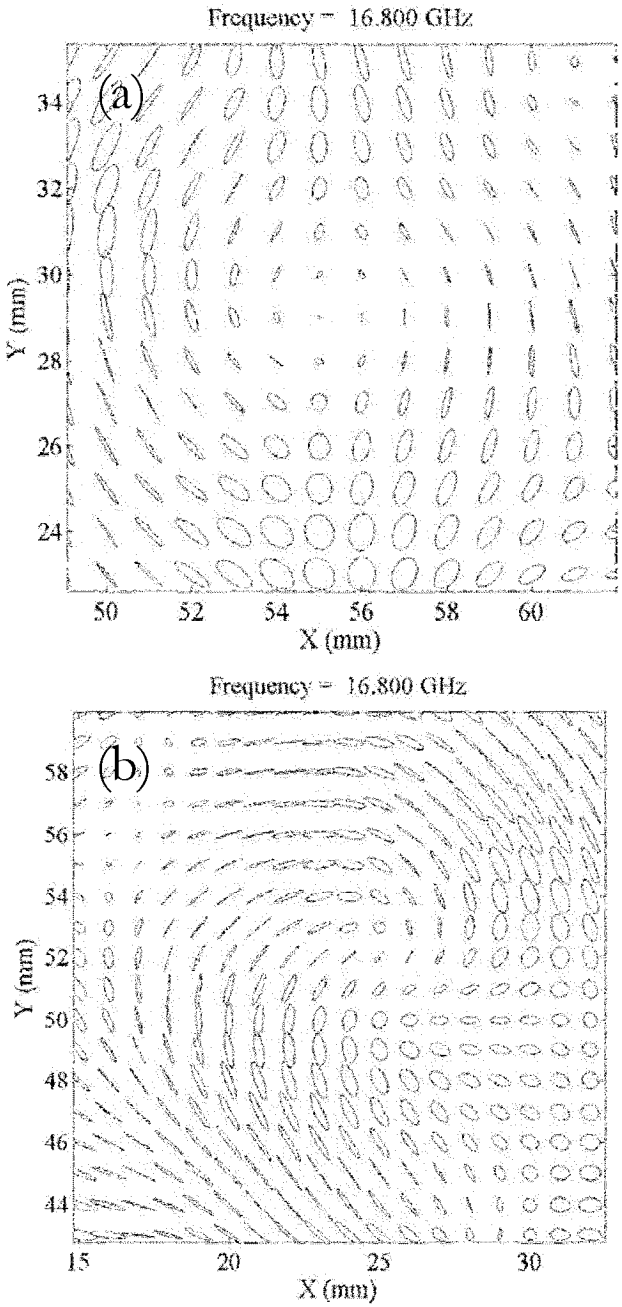

Fig. 1-4: Measured polarization ellipses in a microwave field in different parts of speckle pattern with single frequency 16.8 GHz.

1.4 Quasi-1D geometry

In the past two decades, much effort has focused on achieving localization of classical waves in three-dimensional samples. To date, photons have only been localized in samples without residual long-range order in one-[49,50], two- [34], quasi-1D [33,35] samples and in layered samples [51-53]. As mentioned before, waves are always localized in sufficiently large 1D and 2D system. One way to localize radiation is to reduce the sample dimensionality. The quasi-1D geometry is in fact three-dimensional locally but confined in the transverse directions with reflecting boundaries of length L, considerably exceeding the sample's transverse dimension, L>> W. As a result, there are only finite number of modes $N= 2\pi A/\lambda^2$. Because of reflected boundaries, the return of waves to any region of the sample is enhanced and the probability of returning to a typical coherent volume consequently with increases with sample length. As a result, the wave can be localized as the sample length is increased, while the cross section area remains fixed. Since all modes may be assumed to be mixed, the statistics of propagation are the same at any point on the output surface. This can be achieved experimentally, in samples contained in a long metallic cylinder. The methods of random matrix theory [54,55] are well suited to such systems and have provided nonperturbative results in the weak scattering limit[16,30].

1.5 Outline of this thesis

This thesis deals with wave transport in one-dimensional random waveguides and in multiple scattered quasi-1D systems. Chapter 1 reviews key concepts and presents a broad overview of the thesis. It also presents our observations of the speckle pattern and reveals its essential structure. In Chapter 2, we explore the character of waves in an open dissipative one-dimensional random waveguide. When the field distribution is not a single peak and the corresponding spectrum is not Lorentzian, we are able to decompose the field into a sum of quasimodes. These modes are multi-peaked in space and have Lorenztian linewidths. Transmission is dominated by these overlapping quasimodes. This is particularly the case when absorption is present since long-lived localized modes are more strongly suppressed than quasi-extended quasimodes. In Chapter 3, we show that the intensity correlation function may be expressed in terms of the complex square of the field correlation functions with respect to displacements of the source and detector. The correlation function is a sum of three types of terms - multiplicative, additive and constant with respect to displacements of the source or detector. When the source position is fixed, the correlation function takes on a universal form in terms of a single parameter, the degree of correlation. In the last part of this chapter, we present a preliminary study of microstatistics of the two-dimensional speckle pattern of single sample

realizations measured in scan of the field transmitted through a quasi-1D random sample over the output surface. In chapter 4, we consider the pulse response by appropriately Fourier transforming the measured spectrum. We investigate the time dependence of field and intensity correlation with displacement and polarization rotation. This allows us to view the growth of weak localization and mesoscopic fluctuations in the time domain. Chapter 5 addresses the statistical properties on the phase, the first derivative of phase in frequency and space, and the transverse current, which is the product of the intensity and the first derivative of phase with spatial coordinate x. An important experimental consideration is the effect of the finite spatial step size upon the probability distribution of the first derivative of phase and the transverse current. Our findings and conclusions are summarized in Chapter 6. Most of the results of this thesis are presented in Refs. [42,43,56-58].

CHAPTER 2

WAVE TRANSPORT IN PERIODIC AND RANDOM SINGLE MODE WAVEGUIDE

2.1 Introduction

Periodic structures of dielectric material exhibit the band structure similar to that for quantum-mechanical electron, waves in the band in which propagation for forbidden [6,7]. This so called photonic band gap (PBG) can be used to control wave propagation through inhomogeneous dielectric contrast. The periodicity of such photonic crystals (PCs) can be disrupted to create localized modes. These confined modes are high quality factor cavities within the disordered PC, which can be used as optical resonators. The most obvious application for imperfect PCs is to provide laser cavity for random laser or for single-defect of photonic band gap lasers [59-61]. With manipulating disorder, we can change our system from ordered PC, single defect PC to completely random media in one dimensional waveguide geometry.

Though the nature of wave propagation in disordered samples reflects the spatial extent of wave within the medium [12,13], in part because of the inaccessibility of the interior of multiple-scattering samples, the problem of

transport in the presence of disorder has been treated as a scattering problem with the transition from being extended in space to localized charted in terms of characteristics of conductance and transmission. In the presence of disorder, waves undergo the transition from extended to localized in space. However, in systems of lower dimension like 1D, multiple scattering leads to wave localization since the wave will always return upon itself leading to closed loops of wave trajectories for which interference leads to suppression of transport.

In general, The Thouless number, which is the degree of level overlap, is used to determine the onset of localization in the absence of absorption. It is the ratio of the average width and spacing of states of an open random medium, $\delta = \delta\nu/\Delta\nu$. When $\delta > 1$, resonances of the sample overlap spectrally and the wave spreads throughout the sample. When $\delta < 1$, however, coupling of the waves between deferent portions of the sample is impeded. Well resolved Lorentzian lines in transmission spectra of localized 1D system, known as Azbel resonance[62], originate from the resonances associate with exponentially peaked localized modes in space. However, even in the regime for which $\delta < 1$, modes may occasionally overlap and become extended over space. Mott argued that interactions between closely clustered levels in the range of energy in which $\delta < 1$ would be associated with two or more centers of localization within the sample[63]. Pendry predicted that when modes overlap,

they create a quasi-extended field distribution referred to as a necklace states. These states play an outsized role in transport since waves may then flow through the sample via regions of high intensity which appear to be strung together like beads in the necklace [64,65].

In this chapter, we present measurement of the spatial and spectral dependence of the field for microwave radiation inside an open absorbing single-mode waveguide filled with dielectric slabs either arranged periodically, with single defect, or randomly. In the spectral region in which the density of states vanishes, defect or disorder induced localized modes may appear. In this region, the average level spacing exceeds the typical level width, thus $\delta < 1$. Measurement along the entire length of the waveguide reveals spectral regions in which the energy sometimes exponential peaked at a single localized center, and sometimes peaked at a number of points in the sample. These studies add to our understanding the nature of overlapped modes in region for which $\delta < 1$.

Section 2 of this chapter produces details of the experimental setup and the sample fabrication. We present comparisons between measured spectra with numerical simulation based on the transfer matrix method has been performed.

In section 3, we discuss results from three types of sample. Those are a periodic sample, a sample with single defect, and ensemble of 100 realization of random sample. These experiments allows us to explore the wave transport

properties and spatial distribution for PBG band edge mode, band gap exponentially decay evanescent mode, single defect mode, disorder-induced exponential decay mode due to Anderson localization, and overlapped modes. Special concern is on the decomposition of overlapped modes in which $\delta < 1$ into quasi-normal modes.

Our conclusions are summarized in section 4.

This investigation of microwave propagation in 1D random samples leads to a deeper understanding of the connections between key aspects of wave propagation, localization, and absorption. It has advantages that samples are relatively easy to fabricate with good control of the defects introduced, and to compare measured results with one-dimensional analytical and numerical results.

2.2 Experimental setup and samples

Field spectra are taken along a slotted WR-42 rectangular microwave waveguide with cross section (10.67×4.32 mm^2). The empty waveguide support only a single mode in the frequency range from 13.5GHz to 19.5GHz The ceramic block milled to form the main binary structural element of length $a = 7.74 \pm 0.04$ mm. The ceramic material has index of refraction $n_H = 2$ and the cross section (10.42×3.25 mm^2) $\pm$ 0.2 mm^2. The first half of the block is a

solid piece and the second half has two projecting thin walls of thickness 0.8 mm on either side, shown in the inset of Fig. 2-1. Since the cross section of the

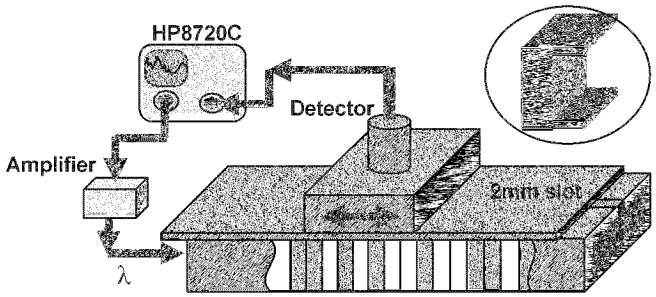

Fig. 2-1: Schematic of experiment setup. Inset shows the structure element of the random sample inside the waveguide.

structural element only fills 67% that of the waveguide, we can estimate the effective index of refractions as $n_1 \sim 1.67$ and $n_2 \sim 1.08$ respect to high and low index of refraction of the structure by using volume filling factor, *f*, for two halves of block, $n = f\, n_H + (1-f)\, n_L$. In above expression, $n_L = 1$ is the index of refraction of air. This result is in agreement with the value obtained from a comparison between the measured and simulated band gap position as we form the periodic structure by applying the binary element described above, see Fig. 2-2.

One hundred realizations of random sample are composed of randomly juxtaposed dielectric elements in two steps. First, orientations of thirty-one binary elements toward or away from the front of the waveguide are randomly selected. Then, five high dielectric ceramic material single blocks and five low

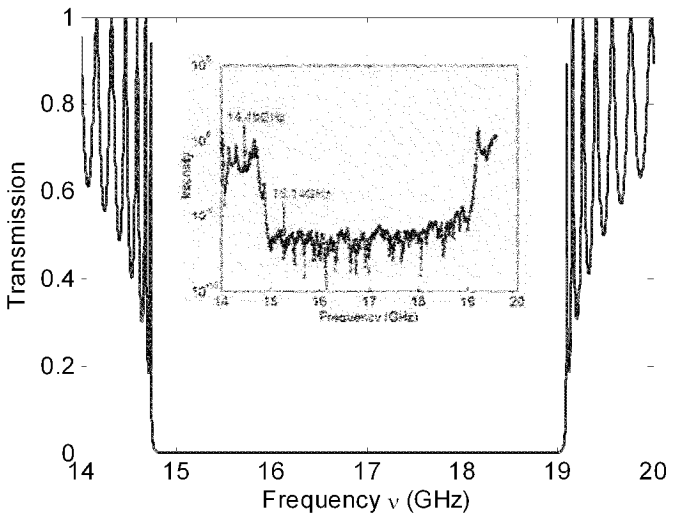

Fig. 2-2 Photonic Band Gap (PBG) comparison between measurement and simulation. The simulation result of transmission through 36 binary elements with $n_1 = 1.67$, $n_2 = 1.08$ gives PBG between 14.7GHz and 19.1GHz. Inset shows the measured transmission for the same structure which exhibits PBG between 14.65 GHz to 19.15 GHz.

dielectric Styrofoam single blocks, each of length 4mm, randomly inserted into the sample from step one. The purpose of the second step is to break the AB pair structure so that localized modes can be created deep in the band gap, where the density of states is low, and the waves is strongly localized. Thus, the total sample length is 28.8 cm. A 2 mm slot was milled along the length of the top of the waveguide to allow us to measure the microwave field. The experiment setup is shown schematically in Fig. 2-1. In order not to distort the

field by the measurement process, the field was weakly coupled to the detector. The core of coaxial adapter, which measures the field to the network analyzer through the cable, was coupled to the sample through a 2 mm-diameter hole in the enclosure where the cable terminated. This enclosure was mounted on the computer-controlled translation stage. In order to reduce the leakage from the open slot, two 5mm thick copper bars were attached to both sides of the box and moved along with it. In addition, many springy copper fingers uniformly applied along the waveguide assured covers maintained good electrical contact with the waveguide. The connector through which the incident field is coupled to the waveguide is a standard waveguide adaptor located 60cm apart from the front of the random slabs. For each random realization of the sample, the detector was translated to 350 points spaced by 1mm. The first sixty-two points correspond to the empty waveguide before the sample. This allows us to normalize the field within the sample by the incident wave, which is obtained by analyzing the standing wave spatial distribution in this empty regime.

Complex field spectra are collected at each position with use of a HP8720C vector network analyzer. Each spectrum covered a 6 GHz-range with 1601 points, giving a frequency step of 3.75MHz, which is considerably smaller than the linewidth of the narrowest modes observed, which is approximately 20MHz. This frequency resolution allows us to study the time

response of a broad band Gaussian incident pulse by applying a Fourier transform technique, which will described in chapter 4. By using smaller integrate frequency bandwidth as 100 kHz for the field spectrum measurement, we achieved low noise result yet much time consuming than the measurement with large integrated frequency bandwidth.

2.3 Results and Discussion

2.3.1 Observation of band gap and Bloch waves in periodic sample

In late 1980's, it was shown experimentally and theoretically the existence of certain propagation forbidden frequency ranges in three dimensional periodic dielectric structures[66-68]. However, design and fabrication of such 3D photonic crystal with omni-direction band gap is drastically arduous and sensitive to manufacturing imperfections. For simplifying the complication and still grasping the key feature of PBG, we consider the one dimensional PC, discovered as omni-directional Bagg-reflector [68]. Our sample is a periodic arrangement of slabs of alternating indices of refraction n_1 and n_2 inside the single mode waveguide. For an infinite sample length, the dispersion relation between wave vector K and frequency ν can be estimated by solving the following transient equation by using the scalar Kronig-Penney model for 1D periodic structures [69].

$$\cos(\frac{k_1 a}{2})\cos(\frac{k_2 a}{2}) - \frac{k_1^2 + k_2^2}{2k_1 k_2}\sin(\frac{k_1 a}{2})\sin(\frac{k_2 a}{2}) = \cos Ka,$$

where a is the period of the structure, $k_1 = n_1 2\pi\nu/c$, $k_2 = n_2 2\pi\nu/c$, c is the light speed in vacuum, ν is the frequency and K is the complex wave vector. In the

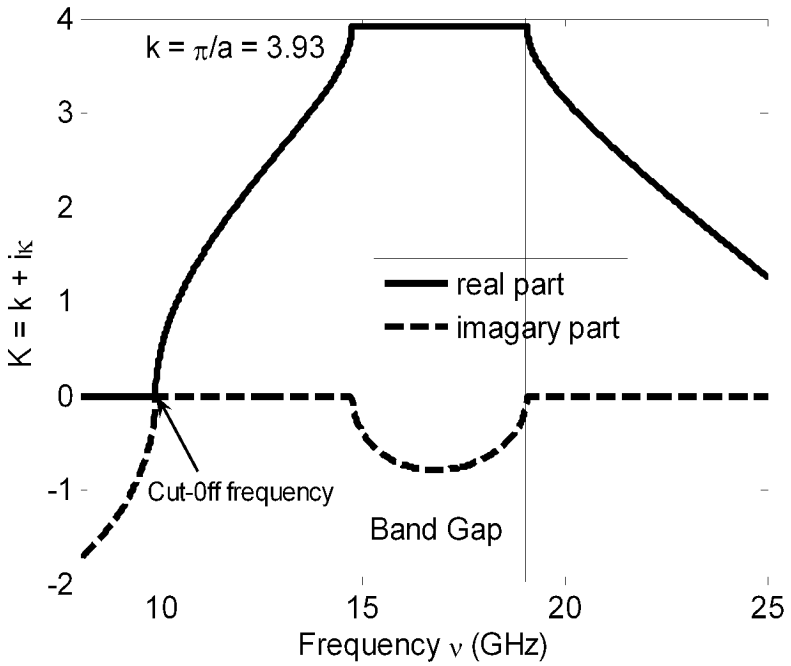

Fig. 2-3 Complex wave vector K for our periodic structure in single-mode waveguide in unit of cm^{-1}. Solid line is the real part and dash line is the imaginary part.

formula, n_1 and n_2 correspond to two indices of refraction of the two materials. Since the sample is enclosed in a waveguide with a single-mode TE_{10} mode, the waveguide dispersion relation $n = \sqrt{n_0^2 - \frac{\pi^2}{(\omega^2/c^2)W^2}}$ must be applied. In this way the effective indices of the two materials in the waveguide, n_1 and n_2, are determined based on the indices of the two materials n_{10} and n_{20}. The W is

the width of the waveguide cross section. A plot the dispersion relation of our 1D PBG for the lowest band gap is shown in Fig. 2-3. As we traverse the gap, the real part of wave vector $k = Re(K) = \pi/a \sim 3.93cm^{-1}$ does not change and is determined by the period of structure.

Fig. 2-4 shows the 3D plot of measured field amplitude and a top view of the same data. The gap occurs between the edges of the allowed Brillouin zones between 14.65GHz and 19.15 GHz in frequency. Fig. 2-4(b) shows that waves within the band gap cannot propagate through the sample but decay exponentially with decaying length equal to the inverse of imaginary part of wave vector. The plot of the field amplitude shows parallel ridges with period a over the whole band gap. This corresponds to half the wavelength of standing waves corresponding to the real part of the wave vector, $\lambda = 2a$. Thus, the phase change along the sample is given by: $\phi = k\ L = (\pi/a)L = \pi L/(\lambda/2) = N\pi$ where N is the number of ridges in space. Each time tune frequency through a Lorentzian mode, the phase increases by π. Since there are no modes in the band gap, as we traverse the gap, N is invariant thus there is no additional phase change along the length of the sample. However, the envelope of the field amplitude decays exponentially corresponding to the imaginary part of wave vector, κ. The decay length, $1/\kappa$, increases as the

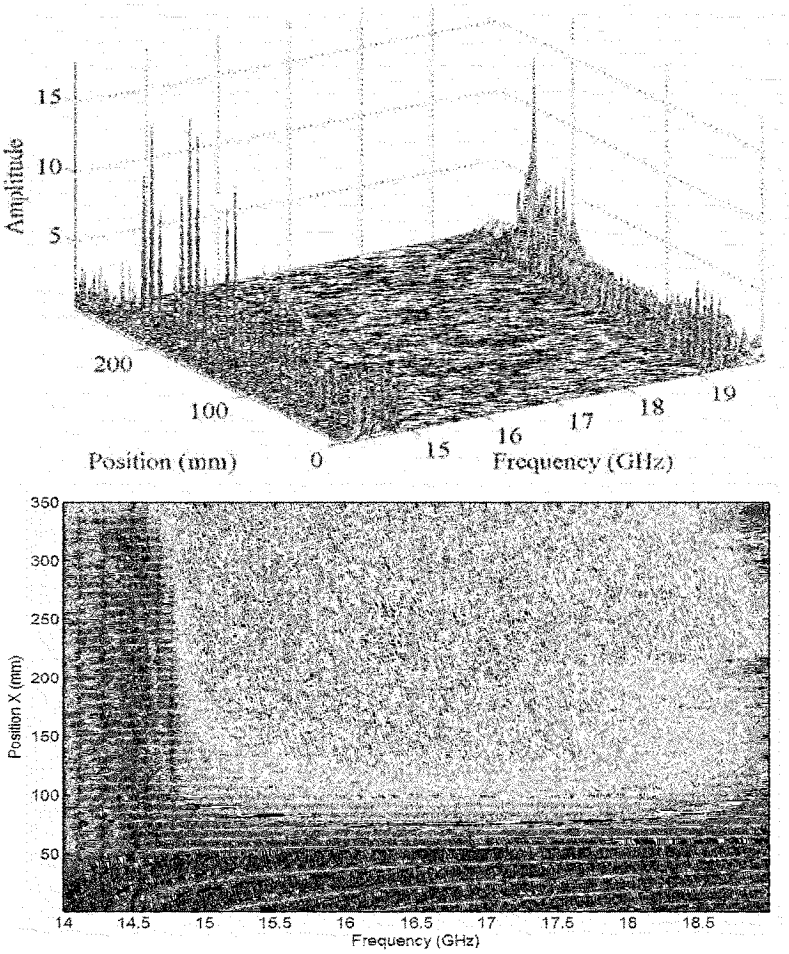

Fig. 2-4. a) 3D plot of the measured field amplitude inside 1D PBG structure in waveguide over 6 GHz frequency range. b) The top view of Fig.2-4 (a).

frequency is tuned from the edge of the gap to the center of gap, then disappears at the other side of edge.

More details of wave propagation and energy penetration into the sample are directly observed from the spatial profiles. Though band theory of photonic crystal is for the ideally infinite structure, the sample in reality is

always finite. This introduces a series of band edge modes which we observe experimentally.

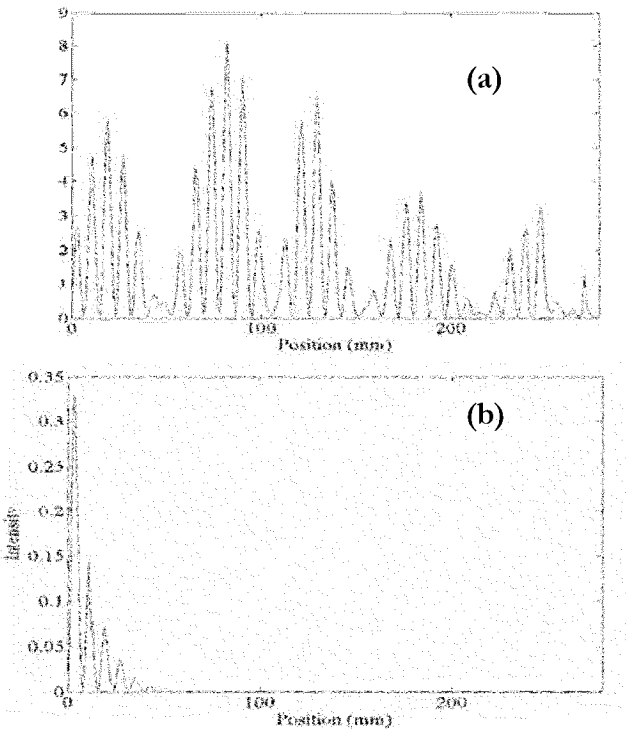

Fig. 2-5. Show the spatial profiles of 5th band edge traveling wave (a) and evanescent waves when incident waves excites frequency with band gap.

Fig. 2-5 (a) shows the spatial profile of the 5th band edge mode. Energy is transported all the way through the sample. The variation of the peak of the envelope is due to the imperfections in the structure. Band edge modes closer to the band gap are more significantly distorted since coherence of the structure must be maintained over a longer length scale for these longer lived

modes. Fig. 2-5 (b) also shows the spatial profile of evanescent wave when the incident wave excites the frequency within band gap.

2.3.2 Observation of defect modes

In the perfect periodic structures, waves are evanescent and decay exponentially within the band gap. Thus the density of states, which is related to the spatial average of the integrated intensity in the sample, tends to zero as the sample length increase. However, a single defect or distributed disorder will introduce long-lived localized modes into the gap. Fig. 2-6 (a) shows the top view of the defect mode as the function of frequency and space. Energy peaks at the position where the single defect introduced. In the spectrum shown in fig. 2-6 (b), a narrow peaked Lorentzian line appears within the gap.

The corresponding resonant frequency of this defect mode depends on the length of the defect. The flow of energy out of the sample and dissipation in the system, such as absorption or gain, broaden the linewidth. Thus, the width of the Lorentzian line, Γ, is the sum of two terms one associated with leakage, and the other with absorption, $\Gamma = \Gamma_l + \Gamma_a$. When the single defect is moved deeper into the center of the sample, the effect of leakage has lesser impact while the impact of absorption increases. When the sample length is much larger than the localization length with the defect at the center of the sample, where far from the sample boundaries, width of Lorentzian line

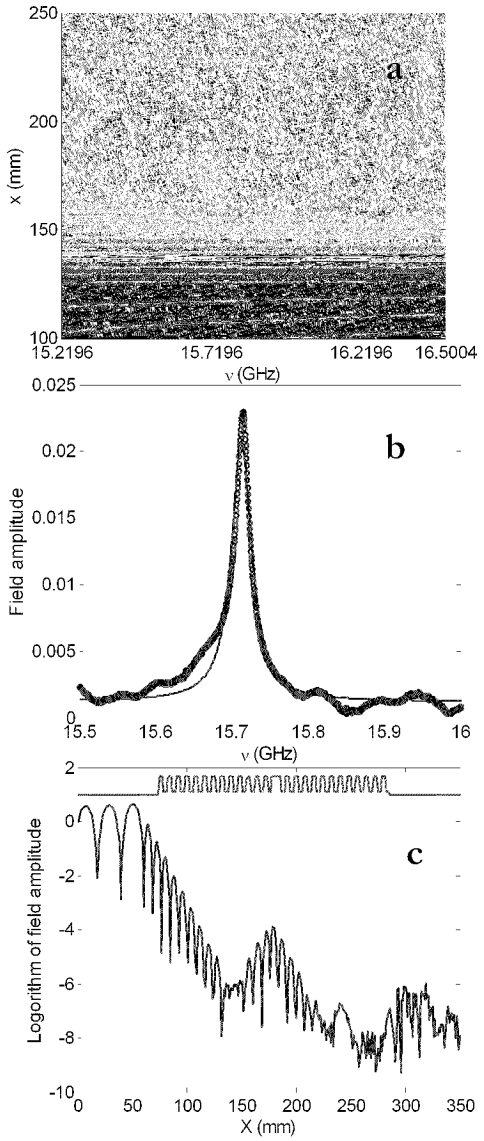

Fig.2-6 a) Top view of field amplitude as function of frequency and space. In the circle is the localized mode due to the single defect at the middle of 26-pair periodic structure, which has sample length 21.2 cm. b) spectral lorentzain line for defect mode. c) spatial distribution of defect mode.

saturates to Γ_a. Fig. 2-6 (c) shows a semi-logarithmic plot of the spatial

variation of intensity.

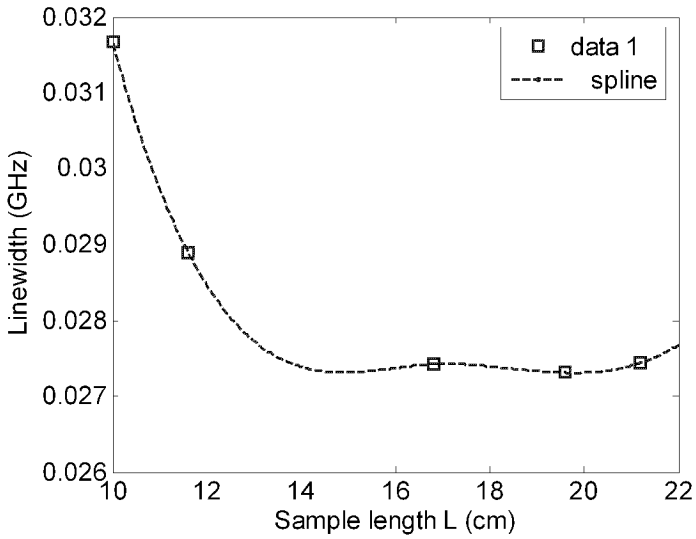

Figure 2-7: Linewidth of defect mode as the function of sample length when keeping defect at middle of the sample.

We carried out two additional experiments to study single defect modes. One is that single defect is kept at the middle of the sample while sample length is varied from 10cm to 21.2 cm. The exponential decay length of intensity near the defect is about 1.3 cm. We found that the linewidth of the defect mode saturate to a value of about 27 MHz. Comparison to simulation suggests this is the contribution of absorption. Fig. 2-7 shows the linewidth as a function of sample length L. In the second experiment, the sample length is fixed at 24.4 cm, but the position of single defect, x, is changed from 2.6 cm to 12.2 cm into the sample. The linewidth saturates to about 27 MHz while the peak intensity decay exponentially with increasing x,(Fig. 2-8).

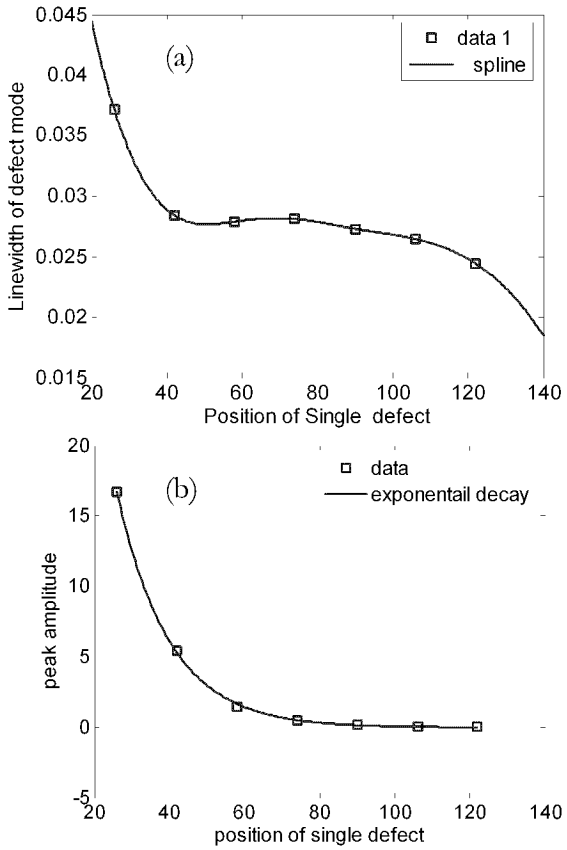

Fig. 2-8: a) Linewidth of defect mode as the function of position of defect for fixed sample length. b) Peak amplitude in space of defect mode as the function of position of defect for fixed sample length. (Unit for x-axis is mm)

2.3.3 Isolated and overlapping modes in random waveguide

In all random samples, spectrally isolated Lorentzian lines associated with localized waves were observed. Only when the field displays overlapping

spatial and spectral peaks, however, does the field penetrate substantially beyond the first half of the sample as a result of absorption at the frequency less than 18.7GHz. Thus frequency range, which is smaller than 18.7 GHz, gives the work regime of localization where $\delta > 1$. Above 18.7 GHz, modes typically overlapped, so that $\delta > 1$ and wave are extended. The exponential decay in space defines the localization length ξ of the mode as a function of

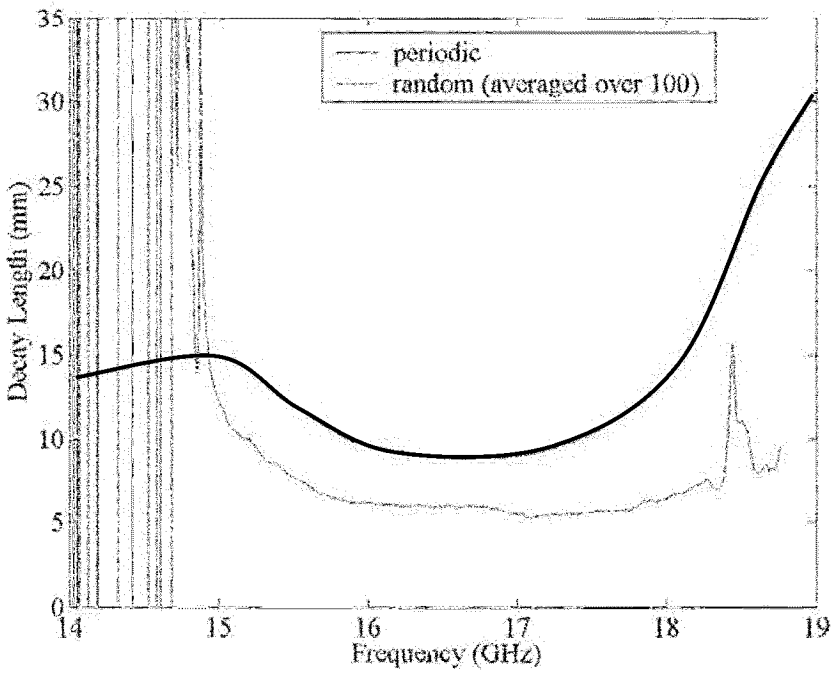

Fig.2-9. Exponential decay length in space shows the localization length of the random ensemble as function of frequency. Thin curve is for periodic structure and it shows the band gap.

frequency, see Fig.2-9. The thin curve is for periodic structure and shows the small decay length within band gap for exponential decay. The thick curve is for random sample and shows the residual of the band gap.

In the regime, in which the wave is generally localized, that is typically the linewidth $\delta\nu$, is shown to be smaller than the space between successive localized mode, $\Delta\nu$, we found that whenever modes overlapped in spectra, they are also overlapped in space and exhibit enhanced transmission. Fig. 2-10 shows two projections of the field amplitude of the spectrally overlapped mode. When the frequency is tuned through a Lorentzian line, which corresponds to a localized mode (e.g. ν = 15.3 GHz), the phase of field increases by π *rad* and an additional peak in the amplitude variation across the sample is introduced. This is shown in the top view of the logarithm of the amplitude plotted in Fig. 2-8 (b).

In the frequency interval between 15.6 GHz to 15.8 GHz in which multiple peaks are observed in the field amplitude, the number of ridges in space is increased by three, corresponding to three successive π phase shift. This suggests that three Lorentzian shaped modes are superposed to form the field in the sample.

2.3.4 Decomposition of quasi-normal modes and impact of structural perturbation

The idea that the field can be expressed as the superposition of quasi-modes in this region can be tested by fitting the measured field spectrum excited by the incident wave at each position to the sum of three Lorentzian

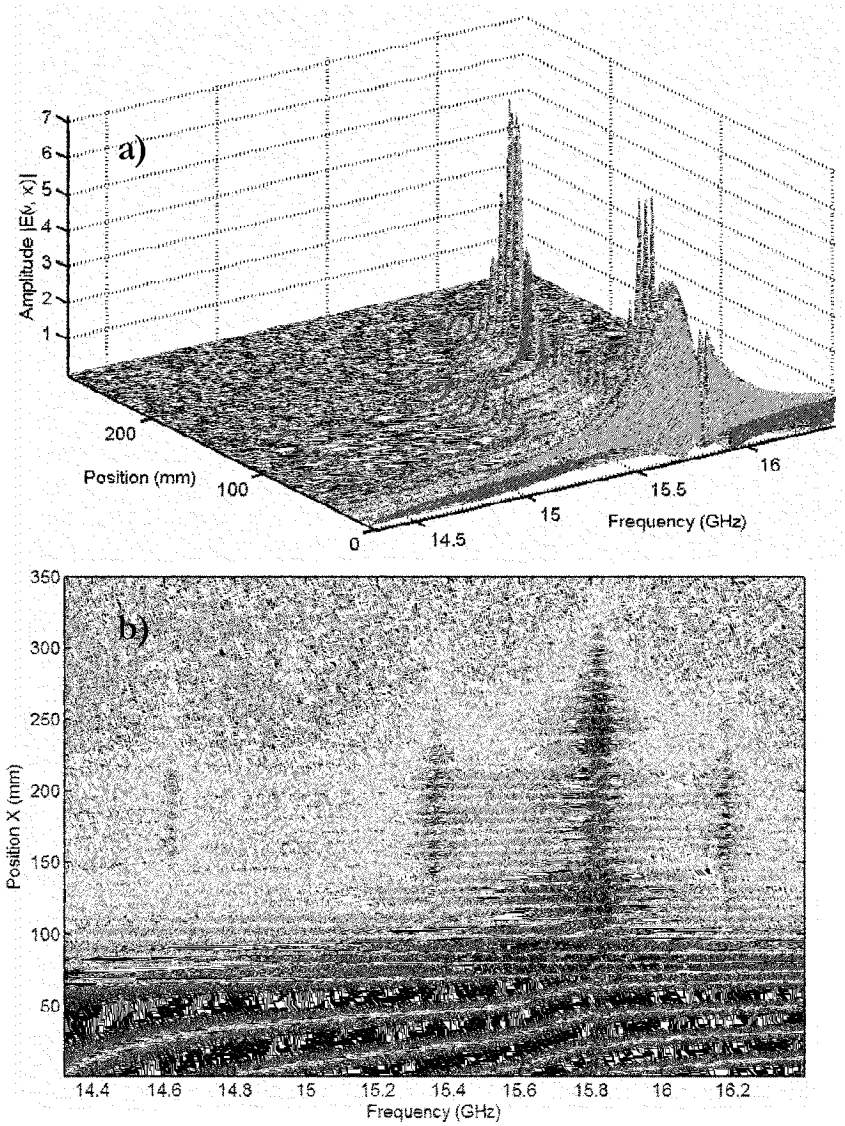

Fig 2-10 (a) Field amplitude of mode overlapped in spectrum and in space. (b) Top view of field amplitude to see the ridges across the sample which shows the π shift for each mode.

lines for overlapped modes, and a slowly varying polynomial of the second degree centered at ν_0 representing the sum of the evanescent wave and the tail

of the response of distant lines. In the following expression, two "satellite" lines at 15.3 GHz and 16.06 GHz are also included,

$$E(\nu,x)=\sum_{n=1}^{5}\frac{A_n(x)+iB_n(x)}{\Gamma_n(x)+i(\nu-\nu_n)}+\sum_{m=0}^{2}C_m(x)(\nu-\nu_0)^m \qquad (2\text{-}1)$$

where ν_0 is the center of our frequency range and n = 1,2,3,4,5 stand for three quasi-modes. $C_m(x)$ is the complex coefficient. Therefore, fields of five decoupled quasi-modes can be given by $A_n(x)+i\,B_n(x)$. Here, ν_0 = 15.66 GHz,

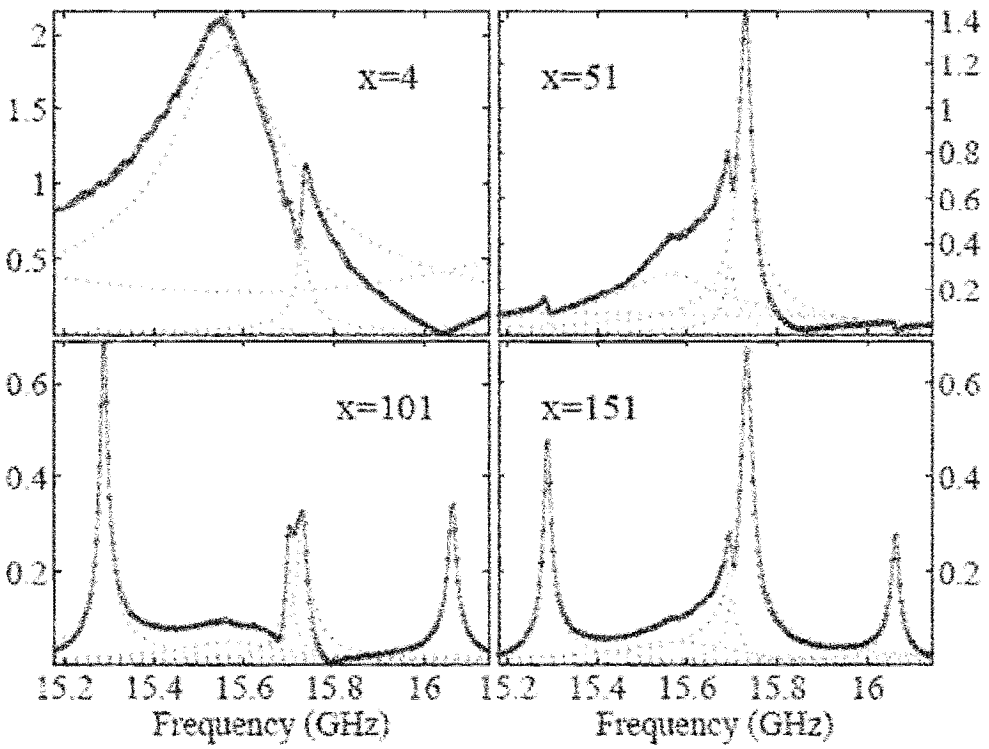

Fig. 2-11: Comparison of the measured field magnitude (dots) to Eq.2-1 (full line) at four different locations. The Lorentzian lines and the polynomial in Eq. 2-1 are represented in dotted lines.

which is the center of the frequency interval considered. An iterative double least-square fit procedure is applied independently at each position x within the sample as follows: first guesses for the central frequencies, ν_n and linewidth Γ_n from the measured peaks used to fit the spectrum at each position x to Eq. 2-1 with the amplitude coefficient $A_n(x)$, $B_n(x)$ and $C_n(x)$ as fitting parameters. These values are used in a second step in which, only the $\nu_n(x)$ and $\Gamma_n(x)$ are fitting parameters with a bounded spectral range. This double fitting procedure can be repeated to improve the fit. The quality of the fit can be seen in Fig. 2-11. Indeed, the chi-square normalized by the product of the integrated spectrum and degrees of freedom (the number of point minus the number of free parameters), remains below 2×10^{-3} over 90% of the sample length. The noise is higher near the sample output where the signal is generally close to the noise level. The central frequencies, $\nu_n(x)$ and linewidths $\Gamma_n(x)$, found in the fit are shown in Fig. 2-12. Fig. 2-13 shows plots of the field magnitudes $\sqrt{A_n^2(x)+B_n^2(x)}$ associate with corresponding $\Gamma_n(x)$ and $\nu_n(x)$. Fluctuations in $\nu_n(x)$ and $\Gamma_n(x)$ are large only at positions for which the peak magnitude of the terms for the n^{th} mode are low, as can be seen by comparing Fig. 2-12 and Fig. 2-13. In the domain in which fluctuations in the central frequencies and linewidths for a particular quasimode are low, these quantities are virtually independent of position and the field amplitude is given to good accuracy by

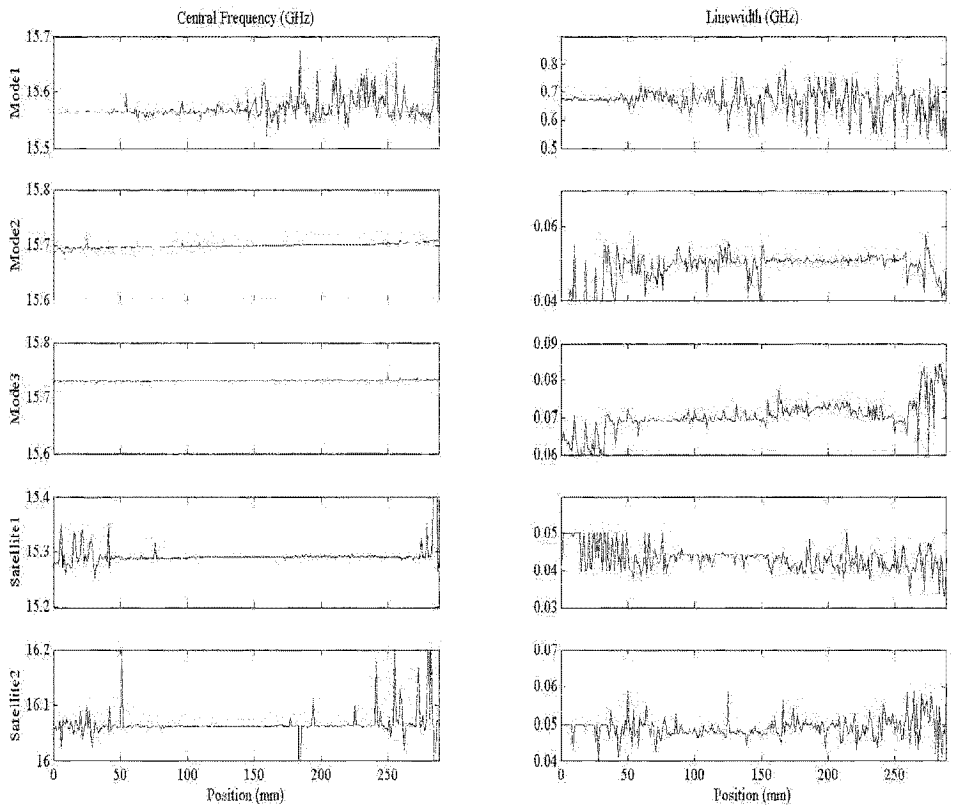

Fig. 2-12: Spatial dependence of central frequency and linewidth for the five modes shown in Fig. 2-10.

substituting the average values of $\nu_n(x) = \nu_n$, and $\Gamma_n(x) = \Gamma_n$ in Eq. 2-1. The drift is greatest in mode 2, where the variation in $\nu_2(x)$ is less than 20% of Γ_2.

With ν_n and Γ_n specified, each of the Lorentzian terms in Eq.2-1 corresponds to a quasimode. The Fourier transform of each term gives the response to an incident pulse in which the temporal and spatial variation factorize, $f_n(x,t) = f_n(x)\exp(-i(2\pi\nu_n - i\Gamma_n)t)$ corresponding to a sum of exponentially decaying quasimodes. The independent decay of the quasimodes

indicates that they are orthogonal. For the three spectrally overlapping modes, "mode1" ($\nu_1 \approx$ 15.56 GHz, $\Gamma_1 \approx$ 0.67GHz) is broad as a result of its closeness to the input. "mode2" ($\nu_2 \approx$ 15.70 GHz, $\Gamma_2 \approx$ 0.051GHz) and "mode3" ($\nu_3 \approx$ 15.73GHz, $\Gamma_3 \approx$ 0.07GHz) are spatially extended and multi-peaked in a spectral range in which quasimodes are otherwise strongly localized. In fact, "satellite modes" are not strictly localized due to the overlap with other modes. The sharply defined modes appearing in the expansion of Eq.2-1 in the regions in which the amplitude of specific modes is greater than the noise in the measured field is consistent with these modes representing a complete set even when they overlap.

Due to dissipation in and leakage from the random sample, the system has non-Hermitian but still symmetric Hamiltonian since reciprocity is preserved. Thus, such Hamiltonian has complex orthogonal eigenvalues when the appropriate inner product is used[70,71]. If the amplitude given by fit are orthogonal, the linewidths of quasimodes would equal to the sum of the absorption rate, Γ_a, and the leakage rate for specific modes, $\Gamma_{ln,}$ for nth quasimodes. The sample dissipation rate is given by the ratio of the net flux into the sample, which is the difference between the incident flux and the sum of the reflected and transmitted fluxes, and the steady-state electromagnetic energy in the sample, which is proportional to $\int_0^L \varepsilon(x)E^2 dx$, where $\varepsilon(x)$ is the

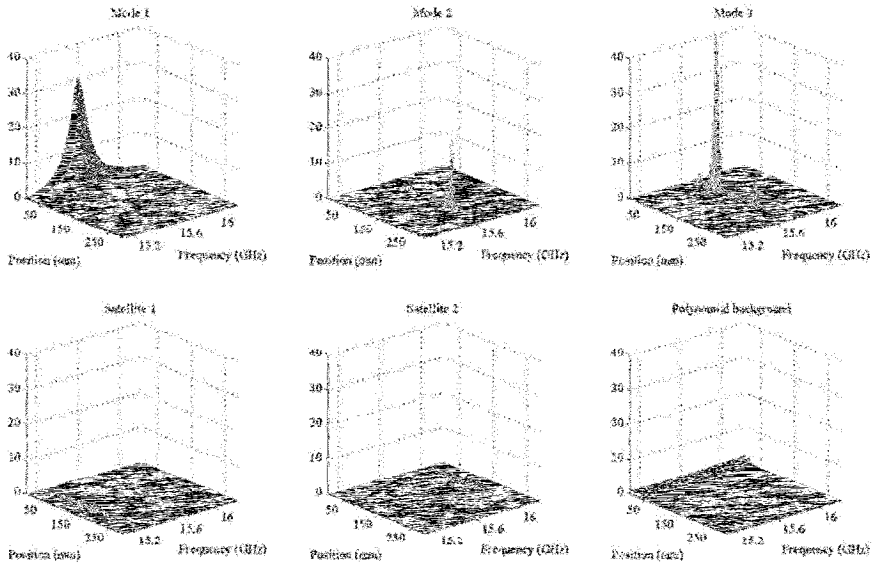

Fig. 2-13: Field magnitude for quasimodes and slowly varying polynomial term in Eq. 2-1.

effective relative permittivity found from measurements in the periodic structure, which make it possible to take account of waveguide dispersion. $\Gamma_{ln,}$ is determined from the ratio of flux away from the sample for a given quasimode to the energy in the sample for this quasimode for steady-state excitation. The leakage from the sample for a given quasimode is obtained by decomposing the scattered wave in the empty waveguide surrounding the random sample into a sum of Lorentzian lines as given in the first sum on the right hand side of Eq. 2.1. The flux is then proportional to the product of the square of the amplitude of this field component and the group velocity in the waveguide. Within experimental uncertainty of 25%, we found that the mode linewidths are equal to the sum of the absorption and the leakage rates.

2.4 Conclusion

We have measured the microwave field inside periodic, single defect, and random configurations of dielectric elements in an open dissipative single-mode waveguide. We observed the different kinds of wave propagation. The deeper penetration of energy associates with the overlapped states with presence of absorption. Decomposition of such overlapped states gives quasi-normal modes with multiple peaked spatial field distribution. The linewidths of quasimodes are equal to the sum of the absorption and leakage rates within experimental uncertainty. The demonstration that quasimodes are well-defined when the spacing between their central frequencies is comparable to their linewidth, suggests that a quasimode description may also be appropriate for diffusing waves in samples with $\delta > 1$.

CHAPTER 3

STEADY STATE SPATIAL CORRELATION IN QUASI-1D RANDOM SAMPLE

3.1 Introduction

A wave propagating in a random medium undergoes multiple scattering. And within a static sample, transmitted waves respect to a monochromatic incident wave is temporally coherent. As a result, a complex interference speckle pattern arises in the transmitted field. This spatially granular structure of intensity manifests large fluctuation with a correlation length on the scale of wavelength in transmission[46]. The intensity within the speckle pattern exhibits long-range correlation[29,72], which results in enhanced fluctuations in total transmission and transmittance.

When waves enter an inhomogeneous sample, the original direction is randomized after a transport mean free path. Waves then undergo different sequences of scattering events, which we refer to as trajectories of partial waves, which have a wide distribution of path length s. The field at a given point on the outgoing boundary of the sample is the superposition of randomly

phased contributions of all partial waves reaching that point and can be represented by the complex field amplitude with magnitude A and phase ϕ:

$$E(\nu,r)=\sum_n A_n e^{i\phi_n} = A(\nu,r)e^{i\phi(\nu,r)}, \qquad (3\text{ -}1)$$

where A_n and ϕ_n are respectively the magnitude and phase of the field amplitude associate with the n^{th} trajectory through the sample. Figure 3-1

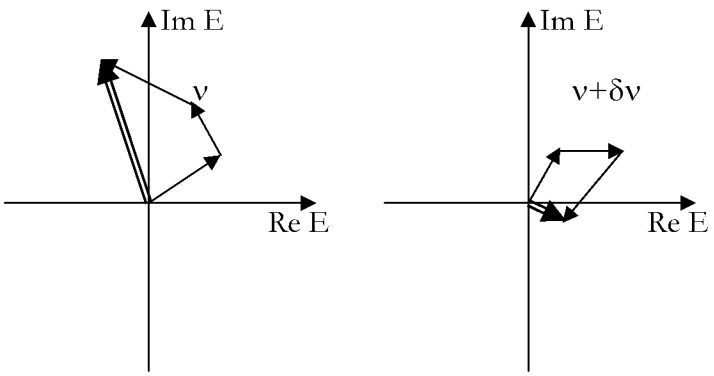

Fig. 3-1. Schematic graph for the total field as superposition of partial waves associated with different trajactories.

schematically illustrates the partial waves and the resultant field at given point for incident monochromatic waves at two frequencies. Each partial wave is represented by an arrow or phasor with length proportional to the magnitude and at an angle to x-axis equal to its phase. The fluctuations in the field with frequency shift at a given point are mainly due to changes in the phase associated with similar trajectories, $\Delta\phi = 2\pi s/(\lambda+\Delta\lambda) - 2\pi s/\lambda = 2\pi s\Delta(1/\lambda)$, since $c/\lambda = \nu$, $\Delta\phi = (2\pi s/c)\Delta\nu$. The study of laser speckle patterns is ordinarily

based on the assumption, that all partial waves are statistically independent. This is satisfied for weak scattering sample. Many statistical properties of the complex field, the intensity, the phase and derivative of phase can be derived under this assumption [2]. Since a large number of partial waves are added to produce the resultant field, the real and imaginary parts of field are asymptotically Gaussian as a result of the central limit theorem. The field amplitude $Ae^{i\phi}$ is referred to as a circular complex Gaussian random variable. The phase of the field, modulus 2π, is uniformly distributed over the interval [-π,π], while the magnitude of field amplitude follows the Rayleigh distribution. The intensity transmission coefficient into channel b for a wave incident in channel a, T_{ab}, is given as the square of the field, $T_{ab}(\nu,r) = |A_{ab}(\nu,r)|^2$. For the single polarization component in the weak scattering limit, the probability distribution of normalized intensity obeys negative exponential statistics, $P(s_{ab}) = e^{-s_{ab}}$, where $s_{ab} = T_{ab} / < T_{ab} >$ is the intensity normalized by its average over an ensemble of random sample realizations represented by the brackets, <…>. In this case, intensity correlation within the speckle pattern is short ranged, which is given by the modulus squared of the field correlation function. The intensity correlation length, $\delta r \sim \lambda/2$, gives the size of the speckle spot. For quasi-1D systems which are transversely confined, number of transverse modes can be estimated by the number of statistically

independent coherence area, $N = 2\pi A/\lambda^2$, where A is the cross-section area of the sample.

However, the assumption of statistically independent partial waves is not satisfied in multiple scattering systems. This can be observed experimentally. First, the large fluctuations in the transmission coefficient, total transmission in microwave and optical measurements are beyond the prediction of Gaussian statistics and waves deviate from Rayleigh distribution. Second, coherent backscattering [20,73] shows the enhanced probability of returning on average, known as weak localization effect for diffusive samples for which, $g>>1$. Third, long-range spatial correlation of transmission coefficient is observed in microwave measurement. All above are generated by the constructive interference of time-reversed path which cross to form a loop within a sample. These effects called "mesoscopic", which is in between macroscopic and microscopic regime, since the average transport modified explicitly by the wave interference within the sample of temporally coherent waves. As the scattering strength increase, the probability of finding crossed paths in a finite sample increases and weak localization effects increase. Consequently, the long-range intensity correlation grows. Feng, Kane, Lee and Stone calculated the correlation of transmission coefficients for scalar waves in the diffusive regime and identified three contributions[29] by perturbation theory. In an expansion of the cumulant intensity correlation function, denoted

by C, C is the sum of three distinguished terms, short-range correlation C_1, long-range correlation C_2, and infinite-range correlation C_3:

$$C = C_1 + C_2 + C_3, \qquad (3-2)$$

The C_2 term dominates the fluctuations [29] in total transmission and C_3 term leads to the universal conductance fluctuation [74].

In this chapter, we report the microwave measurements of the field and intensity spatial correlation function for the field transmitted through a quasi-1D random sample with displacement of the source and detector, ΔR and Δr, respectively. The measurement, confirmed by diagrammatic theory, allows us to analyze each individual contribution to the intensity correlation function with distinctive spatial dependence. Each term only depends upon the sum or product of the square of field correlation function, $F \equiv F_E^2$ or a constant. Short-range correlation is the multiplicative term $F(\Delta R)F(\Delta r)$. Long-range correlation, C_2, is shown to be the additive term, $F(\Delta R) + F(\Delta r)$. The infinite-range term, C_3, is a mixed term consisting of a constant, multiplicative term, and additive term, $F(\Delta R)F(\Delta r) + F(\Delta R) + F(\Delta r) + 1$. This spatially extended correlation, C_2 and C_3, is essential in approaching the statistics of steady-state wave transport in random media with monochromatic sources. This detailed study suggests that the intensity correlation function can be organized into multiplicative, additive and constant terms and leads us to introduce the degree

of long-range correlation, κ, defined as the value of the intensity correlation when field correlation vanishes. κ is then shown to be equal to the variance of total transmission normalized to its ensemble average value, $var(s_a)$, $s_a = T_a/\langle T_a \rangle$, where $T_a = \sum_b T_{ab}$ and var(s_a) serve as a robust localization parameter [35]. In the next chapter, we will discuss the time dependence of κ in the transmitted pulse response through random sample, thus, the dynamics of κ provides a useful tool for understanding features of dynamics of wave transport from diffusive to localized system.

3.2 Samples and measurement

The samples studied are random mixtures of 1.27-cm-diameter polystyrene spheres at a volume filling factor of 0.52. Randomly positioned scatterers are contained within an OFHC (oxygen-free-high-conductance) 99.999% purity copper circular waveguide with a diameter of (7.62 ± 0.01) cm and length of 100 cm, capped with thin Plexiglass plates. The high purity copper reduces the absorption from the metal wall. The Polystyrene scatterers have a relative dielectric constant ε = 2.35 compared to the air background (ε = 1). The spectral field correlation function for quasi-one-dimensional geometry is calculated to be as[75-77]:

$$C_E(\Delta\nu) = \frac{\sinh q_0 a}{\sinh q_0 L'} \frac{\sinh \alpha L'}{\sinh \alpha a}, \qquad (3\text{-}3)$$

Where $L' = L + 2z_b$ is effective length corrected by the extrapolation length $z_b = \frac{2\ell(1+R)}{3(1-R)}$, R is the reflection coefficient at boundary average over internal incident angle which is measured as 0.13[78], $\alpha = 1/L_a$ where L_a is absorption length, $a = 5\ell/3$ is the randomization distance from the plane in which the intensity inside the medium extrapolates to zero. $q_0 = \gamma_+ + i\gamma_-$, where $\gamma_\pm^2 = \frac{1}{2}(\sqrt{\alpha^4 + \beta^4} \pm \alpha^2)$ and $\beta = \sqrt{2\pi\Delta\nu / D}$. A fit of the spectral correlation function with three parameters (Fig. 3-2) to the measured function

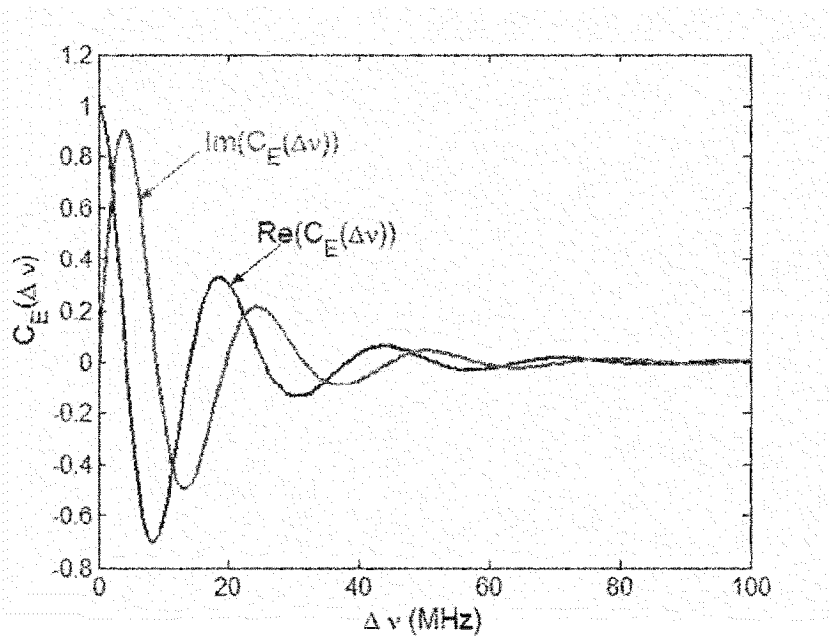

Fig. 3-2: Real (blue line) and imaginary part (red line) for spectral correlation function.

gave an absorption length, L_a = 33.3 cm, a diffusion coefficient. D = 3.3×10^{10} cm^2/s, and a = 18.3 *cm* [43]. Thus, the mean free path ℓ =3a/5 is approximately 11cm and z_b is about 9.5cm. Field and intensity spectra are obtained in the frequency range from 16.8 GHz to 17.8 GHz with sweep step size of 625 kHz using a Hewlett-Packard 8722C vector network analyzer. Measurement are taken in an ensemble of 690 random samples by tumbling the tube to create new realizations of scatterers after each set of spectra are taken. The output power from network analyzer is 10dBm (10mw).

Fig. 3-3 shows a scheme of experimental set up and sample. To

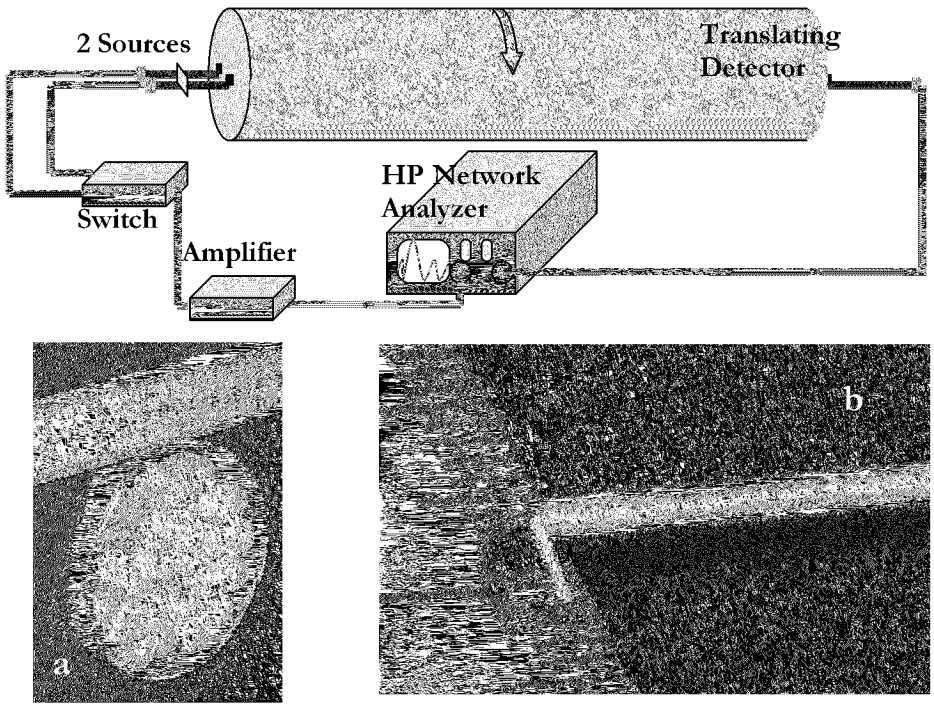

Figure 3 – 3: Scheme of experimental setup and sample.
(a) show the picture of the cross-section of sample (b) show the detector

compensate for losses due to cables, connectors and sample, the microwave system amplifier HP83020A is applied to provide about 30dB gain with noise figure about 10. Field spectra are obtained for each realization by translating a vertical antenna detector along a horizontal line cross the center of the output surface to 50 locations separated by 1.06 mm responding to each of two fixed antenna sources at the incident surface, which are separated by $\Delta R = 3 \pm 0.1$ *cm* $\equiv$ d. The detector and sources antennas have 1mm thickness and about 5mm length. They are aligned perpendicular to the line of translation and are held about 3mm away from the surface. A PC-driven microwave switch (Narda SEM123D) was used to switch from one source to another. Intensity spectra are obtained by squaring the field spectra. To measure the symmetric property of the spatial correlation function with respect to the source and detector, a similar measurement has been carried out by translating the source along a line for each of two fixed detectors at the output surface separated by Δr = d. The separation distance d is much greater than the field correlation length, and the field correlation is no larger than 0.01 at this distance.

In this setup, several technical points are worth mentioning: 1) both the source and detector are isolated in the absorbing chamber from the environment to eliminate noise in the measurement; 2) the moving detector or source were carefully aligned to keep its distance from the surface at a fixed value; 3) the cable length and number of connectors were minimized and all

elements were solidly attached to the optical stage. This assures the relative low noise and large dynamic range measurement.

3.3 Results and discussions

3.3.1 Spatial Field Correlation

Radiation of frequency ν emitted by a source antenna at $\vec{R}$ from one end of the tube and detector set at point $\vec{r}$ at the other end. Intensity is then denote by $I_\nu(\vec{R},\vec{r})$. We consider the normalized cumulant intensity correlation function defined as:

$$C(\Delta r,\Delta R)\equiv\frac{<\delta I_\nu(r,R)\delta I_{\nu'}(r',R')>}{<I_\nu(r,R)><I_{\nu'}(r',R')>}, \qquad (3-4)$$

Where δI_ν is the deviation of the intensity from its ensemble average value, $\Delta r=\left|\vec{r}-\vec{r}'\right|$ and $\Delta R=\left|\vec{R}-\vec{R}'\right|$ are the displacements across the output and input surface, respectively, and <…> denote the average over an ensemble of random realizations. The leading contribution to C is obtained by factorizing the field is [46,48,79]:

$$C_1(\Delta r,\Delta R)\equiv\frac{\left|<E_\nu(r,R)E^*_{\nu'}(r',R')>\right|^2}{<I_\nu(r,R)><I_{\nu'}(r',R')>}, \qquad (3-5)$$

which is the square of field-field correlation function.

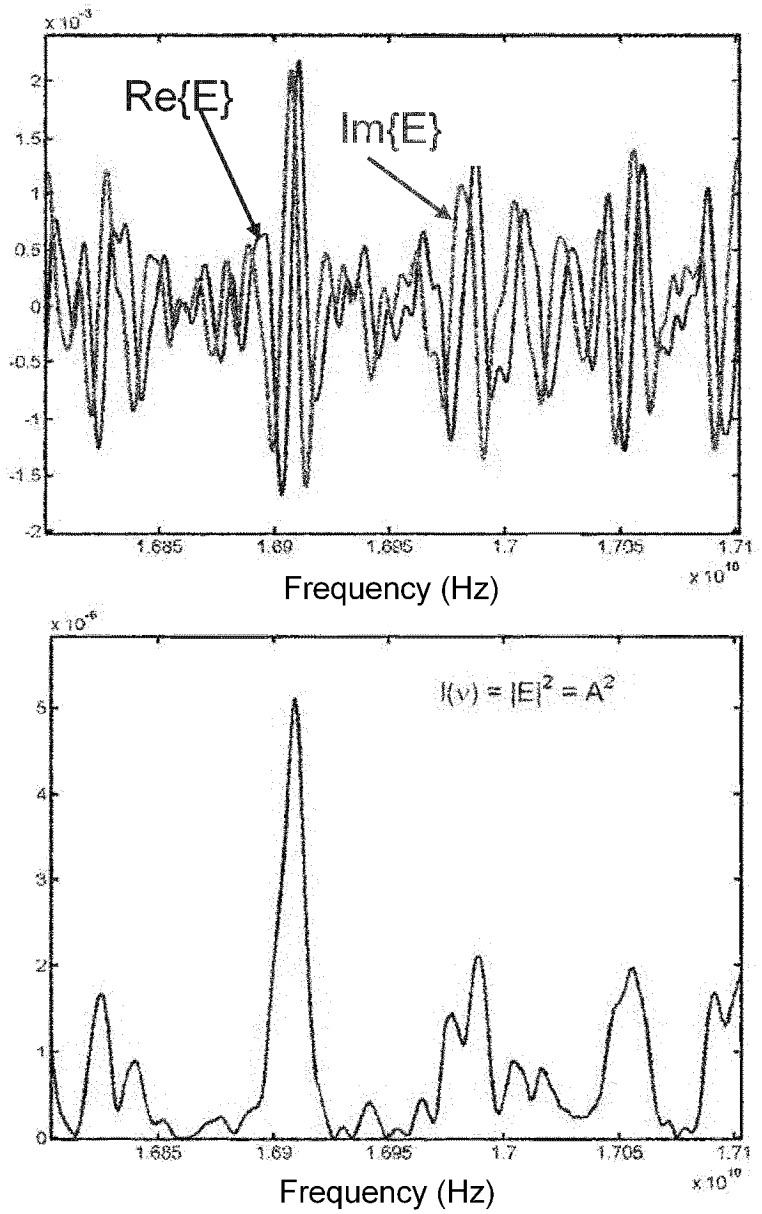

Fig.3-4: Typical normalized field and intensity spectra from the measurement at a fixed point. Blue and red curve corresponding to the real and imaginary part of field. Intensity obtains from the square of the magnitude of field, $I = |E|^2$.

We first present the observation of the transmitted field correlation

function <EE′*> in the spatial domain, whose corresponding Fourier transformation gives the angular distribution of intensity in the far field [80]. In order to remove the instrumental response in the measurements of field and intensity, the field is normalized by the square root of the ensemble averaged intensity and the intensity is normalized by the ensemble averaged intensity at each position and frequency. Figure 3-4 shows the typical normalized field and intensity spectra from measurement at a fixed observation point. Intensity is taken as the square of the magnitude of field $I = |E|^2$.

The real and imaginary parts of the spatial field correlation function,

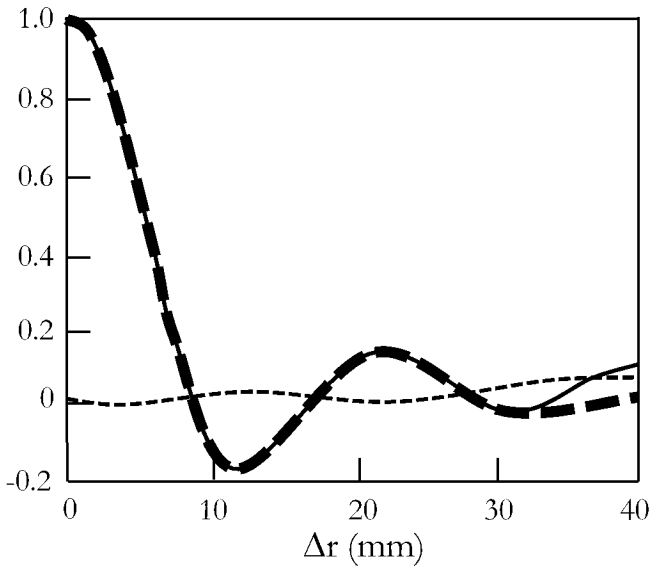

Figure 3 -5: Real and imaginary part of spatial field correlation function averaged over 690 configurations and frequency between 16.8 ~ 17.8 GHz

$F_E(\Delta r) = \langle E(r,\nu)E^*(r+\Delta r\ ,\ \nu)\rangle$, and the fit to the theoretical form are shown in Figure 3-5. Results obtained from averaging over all 690 configurations, frequency ν between 16.8~17.8 GHz, where transport parameters do not change quickly [81]. The real part of the field correlation function is unity due to the field normalization. The imaginary part of the field correlation function is very small. As shown below, this is the consequence of the isotropic random sample. From definition, $F_E(\Delta r) = \langle E(r,\nu)\ E^*(r+\Delta r,\nu)\rangle = \langle\ E^*(r-\Delta r,\ \nu)\ E\ (r,\nu)\rangle = F_E^*(-\Delta r)$. Since the sample is isotropic, Δr and $-\Delta r$ can be exchanged. It gives $F_E(\Delta r) = F_E^*(\Delta r)$. Since the complex conjugate of field correlation function is equal to itself, the imaginary part vanished. In contrast, for the spectral correlation, $C_E(\Delta\nu) = C_E^*(-\Delta\nu)$. However, frequency shift to higher or lower frequency, $\Delta\nu$ or $-\Delta\nu$ respectively, can not be exchanged. So, $C_E(\Delta\nu) \neq C_E^*(\Delta\nu)$, the imaginary part does not vanish.

The first theoretical study on the short-range correlation inside a bulk medium, C_1 contribution, was based on diagrammatic methods within the factorization approximation [46]. As result, C_1 is the square of field correlation function, given as:

$$F_E(\Delta r) = \frac{\sin k\Delta r}{k\Delta r}\exp(-\Delta r / 2\ell)\,, \quad (3-6)$$

where k is the wave vector within the medium, and ℓ is the scattering mean free path. This yields the short-range correlation in the bulk. However, the

equivalent field correlation function at the surface directly derived from diffusion theory and accounting for the non-isotropic distribution of k and surface was carried out and gives the following expression [47]:

$$F_E(\Delta r) = \frac{1}{1+2\Delta}\left(\Delta \frac{\sin k_0 \Delta r}{k_0 \Delta r} + \frac{J_1(k_0 \Delta r)}{k_0 \Delta r}\right), \quad (3-7)$$

where k_0 is the wave vector in free space and $\Delta = z_b/l$. The solid curve in Fig. 3 -5 is the two parameter fit of the field spatial correlation function to Eq. 3-7. It gives good agreement up to 30 mm displacement with $\Delta = 0.73$, and $k_0 = 3.6\ cm^{-1}$. This near-field correlation is indeed the Fourier transform of the angular distribution of the scattered intensity in far-field predicted to be the following expression [47]:

$$I(\theta) = \Delta \cos\theta + \cos^2\theta, \qquad (3-8)$$

where θ is the scattering angle measured from normal direction.

For later use, we define the modulus square of field correlation function as a form factor $F(x) = |F_E(x)|^2$, where x may be either ΔR or Δr.

3.3.2 Contributions to the intensity spatial correlation

Squaring the field gives the intensity which is used to compute the cumulant intensity correlation function, $C(\Delta R, \Delta r)$. Fig. 3-6 shows the comparison of the intensity correlation function and modulus square of the field correlation function, which gives the C_1 contribution, when either the

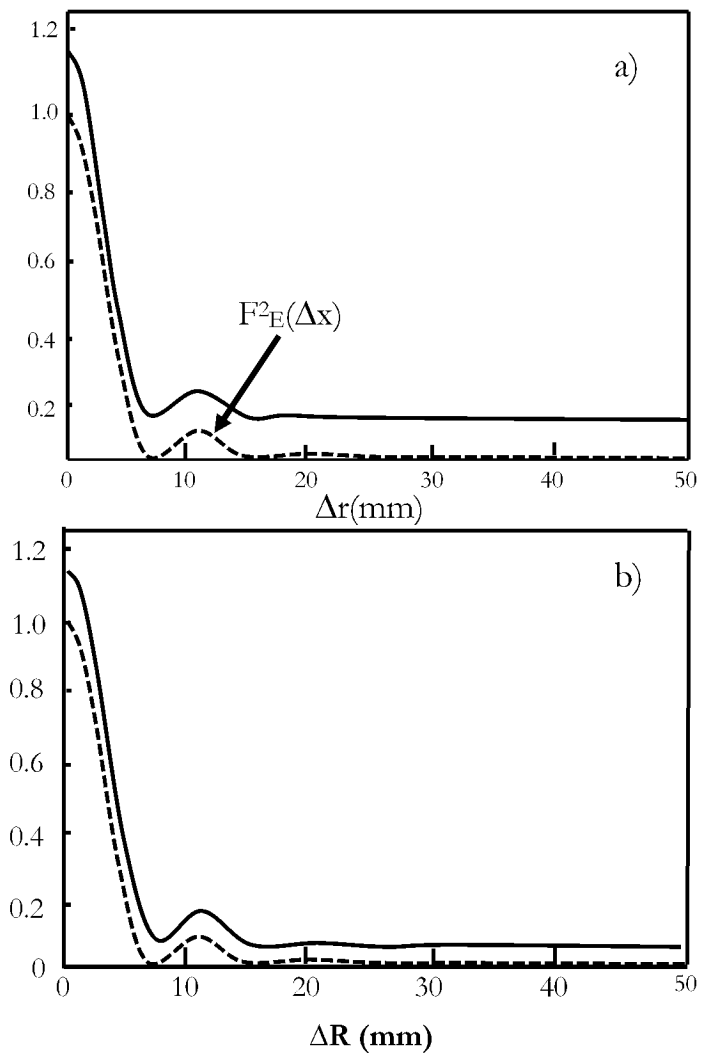

Fig.3 – 6: Spatial correlation of normalized intensity (solid curve) and the form factor function which is defined as the square of field correlation function (dotted curve) for fixed source (a) and fixed detector (b).

source or the detector is moved. Part (a) of the figure shows C(ΔR=0, Δr) and C_1(ΔR=0,Δr) as functions of detector displacement at the output surface corresponding to a single source. Part (b) of the figure shows C(ΔR, Δr=0) and C_1(ΔR, Δr=0) as function of source displacement at incident surface corresponding for a single detector. The first zero defines the correlation length, $\delta r = \pi/k = \lambda/2 \sim 7$ mm in our sample with effective index of refraction approximately 1.3. Compare to the half wavelength within the sample 6.5 mm for central frequency 17.3GHz, it suggests that even our measurement is carried out outside of the sample, sample properties still agree with those within the sample due to near-field. The short-range correlation function, $C_1(\Delta R, \Delta r=0)$, is nearly identical to $C_1(\Delta R=0, \Delta r)$. The solid line in the figure is the theoretical fit to the factorization functional form, $F(x)$. This shows that $C_1(\Delta R=0, \Delta r) = C_1(\Delta R, \Delta r=0) = F(\Delta R) = F(\Delta r)$. When either ΔR or Δr are larger than the correlation length, C_1 drops rapidly to the noise level.

Measurements of C_1 (ΔR, Δr) for ΔR=0 and ΔR=d is shown in Figure 3-7. Within the noise level of 10^{-4}, the two functions have the same variation with displacement, Δr, C_1 (d, Δr) = $2\times10^{-3}C_1$ (0, Δr). The difference between two curves in the figure seems larger, that is due to the rescale for the curve of C_1 (d, Δr) for comparison. This numerical factor, C_1 (d, 0), is approximately equal to the value of C_1 (0, d). These results, taken together with the symmetry

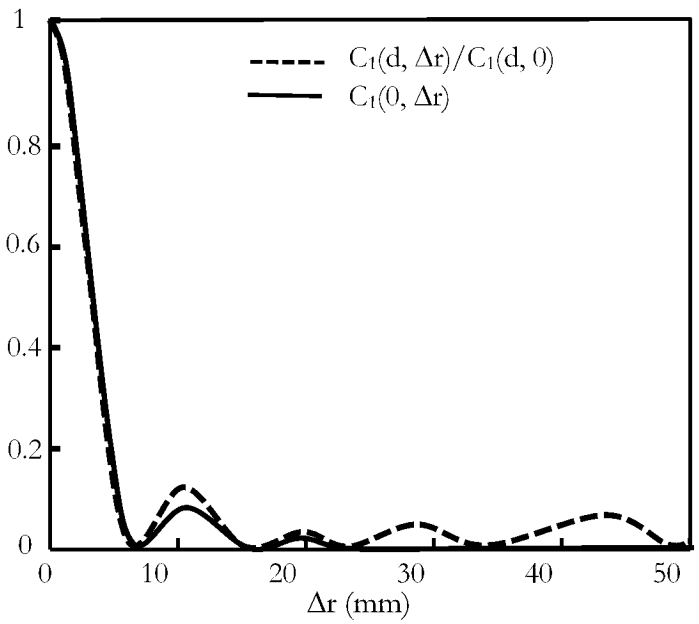

Figure 3 – 7: Comparison of $C_1(\Delta R = d, \Delta r)$ with factor 2×10^{-3}, which is equal to $C_1(\Delta R = 0, \Delta r=d)$, and $C_1(\Delta R = 0, \Delta r)$

with respect to interchange ΔR and Δr, suggest that C_1 can be written as the product of two identical function, $C_1(\Delta R, \Delta r) = F(\Delta R)F(\Delta r)$.

Actually, intensity is correlated at length considerably larger than the correlation length, δr, which defined from short-range correlation of intensity. This indicates that the intensities of spatially separated speckle spots are not statistically independent. Since when one speckle spot is brighter than the average, there is a tendency for all the speckle spots to be brighter. Consequently, the C_2 term produces an enhancement in total transmission

fluctuations over that given by the field factorization approximation by a factor of L/ℓ when absorption is absent.

We now examine the long range correlation by substituting the C_1 term from the cumulant intensity correlation function, $C(\Delta R, \Delta r) - C_1(\Delta R, \Delta r) \equiv (C - C_1)(\Delta R, \Delta r)$, which is dominated by C_2 in the our diffusive samples with $g = Ak_0 l/3\pi L \sim 7$ [79] (See Figure 3-8) for a single source ($\Delta R=0$) and for two sources separate by $\Delta R=d$. The functional forms of $(C-C_1)$ versus Δr for $\Delta R=0$ and $\Delta R=d$ have nearly the same functional form as $F(x)$. For a single source, $(C-C_1)(\Delta R=0, \Delta r)$ drops from the peak value of about 0.15 to a constant level

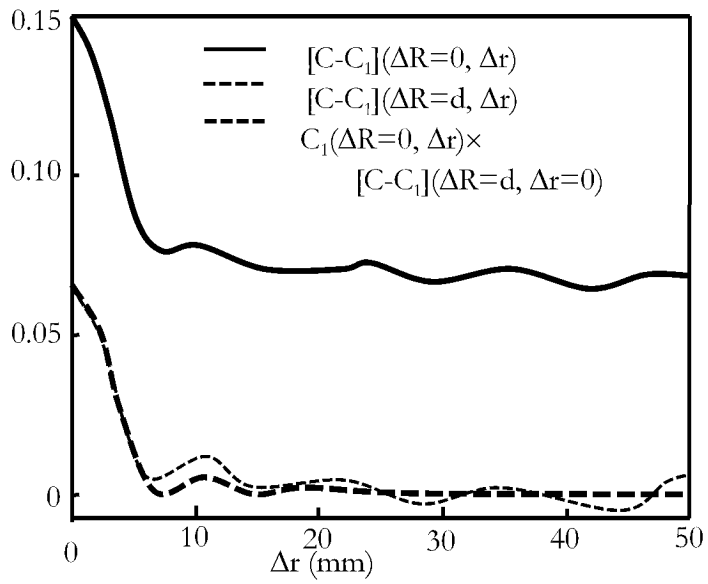

Fig. 3-8: The $(C - C_1)(\Delta R = 0, \Delta r)$ and $(C - C_1)(\Delta R = d, \Delta r)$ which is dominate by the C_2 term in our sample .

with approximately half of the peak value. Continuing to move detector, $(C-C_1)(\Delta R=d>>\delta r, \Delta r)$ drops to the noise level. In addition to the comparison of $(C-C_1)$ and C_1, shown as the dotted line in the Fig. 3-8, this suggests that the dominant term in $(C-C_1)$ is the addition of two identical functional forms F as function of ΔR and Δr, so that it is proportional to $(F(\Delta R) + F(\Delta r))$. Moreover, the residual of $(C-C_1)(\Delta R=d, \Delta r>\delta r)$ gives the evidence of a constant C_3 term. For $\Delta r>30$ mm, the correlation function becomes negative, but here the noise becomes larger than the signal because of the reduced number of pairs of points with increasing Δr.

The structure of the joint spatial and frequency dependences of C_1 and C_2 is obtained from measurements of the correlation functions $C_1(\Delta\nu, \Delta r)$ and $(C- C_1)(\Delta\nu, \Delta r)$ for $\Delta R = 0$, shown in Fig. 3-9a and 3-9b, respectively. The semilog representations in the figure show that, within the limits set by the noise level, C_i have the same frequency dependence for any Δr, while C_i have the same spatial dependence for any $\Delta\nu$ for $i = 1, 2$. Thus their spatial and spectral variations for a single source are given by $C_i(\Delta\nu, \Delta r) = A_i(\Delta\nu)C_i(\Delta r)$. The noise level found in C_1 is low compared to that in C_2 because the field correlation function, F_E, is computed and then squared to give C_1, giving a signal to noise ratio which is the square of that for the field correlation function. The form of the intensity correlation function suggested by

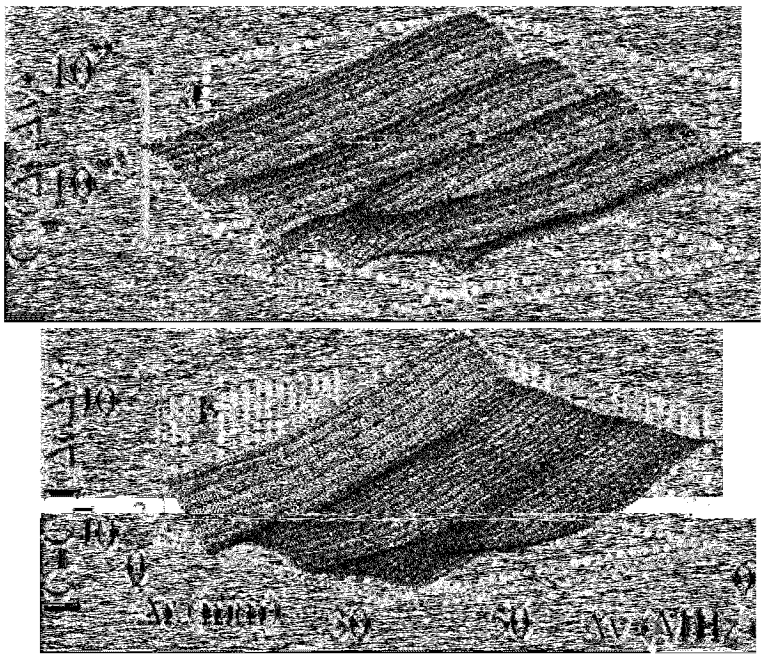

Figure 3 – 9: The structure of the joint spatial and frequency dependence of C_1 and C_2 terms. (a) $C_1(\Delta\nu, \Delta r)$ respect to single source, (b) $(C - C_1)(\Delta\nu, \Delta r)$ respect to single source.

experiment is borne out in the diagrammatic calculation summarized in the next section.

3.3.4 Expression of the spatial correlation of intensity

The three contributions to the cumulant spatial correlation of intensity can be represented diagrammatically. Considering scalar monochromatic wave, the wave function can be written as:

$$\left\{<^2 + k^2(1+\varepsilon(r)+i\alpha)\right\} E_\omega(r) = 0\,, \quad (3-9)$$

The field $E_\omega(r)$ is for the classical scalar wave. The wave vector is, $k = \omega / c$, where c is the speed of wave in the average medium. The imaginary part represents absorption in the average medium. The term $\varepsilon(r)$ representing the inhomogeneity of the medium is assumed to be a white-noise Gaussian random variable, with $< \varepsilon(r) >= 0$ and $< \varepsilon(r)\varepsilon(r') >= \varepsilon_0 \delta(r - r')$. The Green's function method can be used to solve the Helmholtz equation for a specific sample realization. In the weak disordered limit:

$$E_\omega(r) = E_0(r) + \int d^3 r_1 G_0(r, r_1) f(r_1) E_\omega(r_1), \quad (3-10)$$

where $E_0(r)$ corresponds to the field at position r in a homogeneous medium and $G_0(r, R)$ is the Green's function for homogeneous medium, which is a solution of the equation $(<^2 + k^2(1 + i\eta))G_0(r, R) = \delta(r - R)$. The term $f(r) = -k^2 \varepsilon(r)$ represents the spatial inhomogeneity of the medium. The full Greens function for the field at point r due to a point source at position R can be expressed through the following recursive expression:

$$G_\omega(r, R) = G_0(r, R) + \int d^3 r_1 G_0(r, r_1) f(r_1) G_\omega(r_1, R), \quad (3-11)$$

To calculate the ensemble averaged quantities, the above expression for $G_\omega(r, R)$ is first expanded in a Born series and averaged term by term. The procedure for the finding ensemble average of full Greens function can be described using diagram in Fig. 3-10. The thick solid line represents the

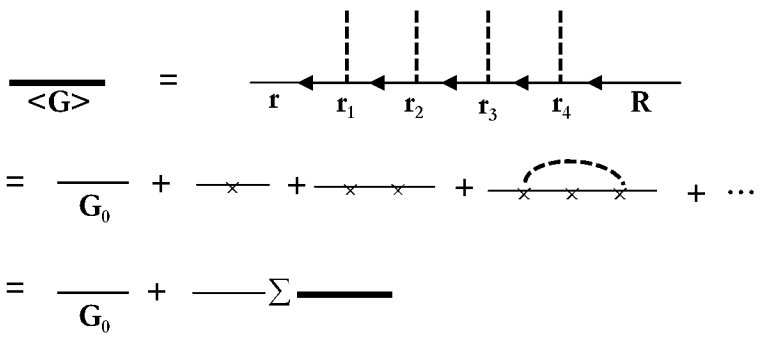

Figure 3- 10: Diagram for finding ensemble average of full Greens function.

ensemble average of the Green's function, whereas the thin solid line represents G_0. The dashed line includes all possible connection between r_i and r_j. The crosses stand for scattering events. The symbol, $\sum$, represents the self-energy operator and includes the sum of all scattering events associated with the scatterers. This gives Dyson's equation for the ensemble of field Green's functions: $<G> = G_0 + G_0 \sum <G>$. Consider the first term of $\sum$, the ensemble average of field at position r due to point source at R can be shown to be:

$$< G_\omega(r,R) >= -\frac{1}{4\pi |r-R|} e^{ik|r-R|} e^{-|r-R|/2\ell}, \quad (3-12)$$

where ℓ is the scattering mean free path.

The field correlation function can then be expressed as $<GG^*>= <G><G^*> +<GG^*>_c$, shown as the ladder diagram Fig. 3-11.

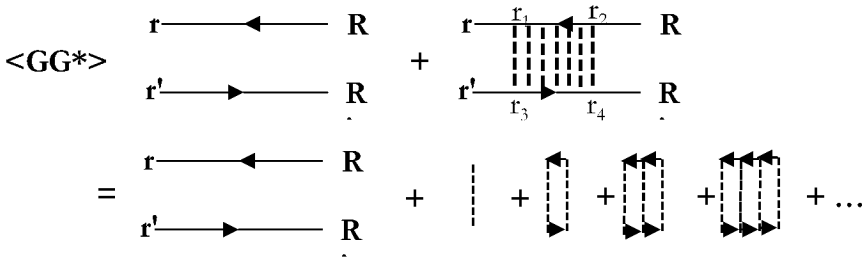

Fig. 3-11: Diagram corresponding to field-field correlation <GG*>. Solid line stands for averaged Green's function

This gives the field correlation function:

$$< E_\nu(\vec{r},\vec{R})E^*_{\nu'}(\vec{r}',\vec{R}') >= \int d^3r_1 \int d^3r_2\, G_\nu(\vec{r},\vec{r}_1)G_\nu{}^*(\vec{r}',\vec{r}_1) \times T_{\nu\nu'}(\vec{r}_1,\vec{r}_2)G_\nu(\vec{r}_2,\vec{R})G_\nu{}^*(\vec{r}_2,\vec{R}') \quad (3\text{-}13)$$

where $T_{\nu\nu'}(\vec{r}_1,\vec{r}_2)$ is called the diffusion ladder or diffuson. For the quasi-one-dimensional geometry, the diffuson is independent of its transverse coordinates, while the Green's functions decay rapidly on a scale of the mean free path. Take $\vec{R}=\vec{R}'$ and $\nu=\nu'$, we obtain:

$$< E_\nu(\vec{r},\vec{R})E^*_{\nu'}(\vec{r}',\vec{R}') >= \frac{4\pi}{\ell} \int d^3r_1 G_\nu(\vec{r},\vec{r}_1) \times G_\nu{}^*(\vec{r}',\vec{r}_1) < I_\nu(\vec{r}_1,\vec{R}) > \equiv F_E(\Delta r) \quad (3\text{-}14)$$

where $I_\nu(\vec{r},\vec{R})$ is the intensity at r, normalized to its average value at the output surface of the tube. The diagram for C_1 term factorizes into a product of two field functions. Thus, $C_1(\Delta R,\Delta r)=F_E^2(\Delta R)F_E^2(\Delta r)\equiv F(\Delta R)F(\Delta r)$.

The diagram for all three contributions to the intensity correlation is shown in Fig. 3-12. Part (a) is for C_1 correlation; (b) for C_2 correlation; (c) for C_3 correlation and (d) is the interaction vertex of the Hikami box, which represent crossing diffusons. In these diagrams, each pair GG* of external Green's functions contributes a spatial form factor F_E as in Eq. 3-11. The full expression of intensity correlation as following [82]:

$$\begin{aligned} C &= C_1 + C_2 + C_3 \\ &= F(\Delta R)F(\Delta r) + \frac{2}{3g} A_2 (F(\Delta R) + F(\Delta r)) \\ &+ \frac{2}{15g^2} A_3 (1 + F(\Delta R)F(\Delta r) + F(\Delta R) + F(\Delta r)) \end{aligned} \qquad (3-15)$$

It confirmed our experimental results on first two terms. As mentioned in the

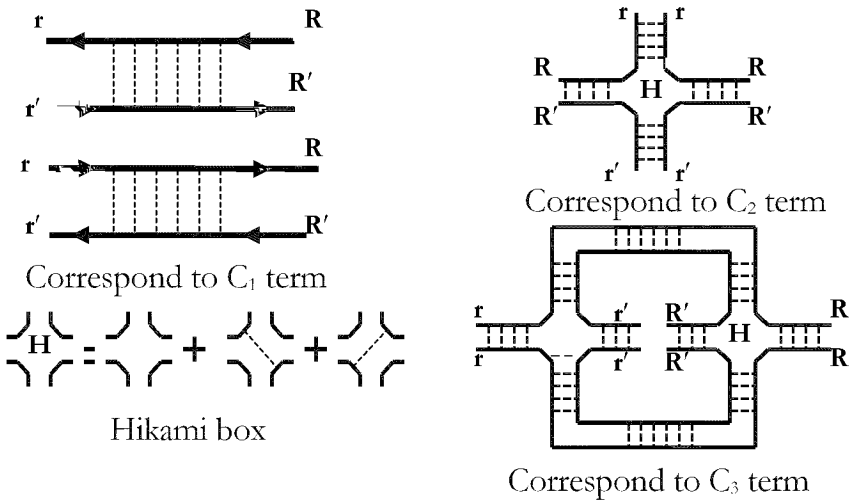

Figure 3 – 12: The diagram for all three contributions of intensity correlations

discussion of the experimental results, the functional form of F(x) is the square of field correlation function. C_1 term is normalized to unity when neither the source nor the detector is displaced, whereas C_2 term is smaller by a factor of order (1/g). For our diffusive sample g = 7, the C_1 term dominates. The C_3 term is of order $(1/g)^2$ and is given from theory as a sum of constant, multiplicative, and additive terms. The structure in Eq.3-15 is similar to that of the correlation in transmission, obtained in the multichannel formalism [29,30,72]. The coefficients A_i (i = 1, 2, 3) depend on the absorption coefficient $\alpha = L/L_a$, where L_a is absorption length obtained as 33.3 cm, and frequency shift, $\Delta\nu$. The field factorization term $A_1(\Delta\nu=0, \alpha)$ is unity and independent of absorption by definition, while $A_2(\Delta\nu,\alpha)$ is given by [47,82,83]:

$$A_2(\Delta\nu = 0,\alpha) = \frac{3}{16\alpha}\left[\frac{\sinh 2\alpha - 2\alpha(2-\cosh 2\alpha)}{\sinh^2\alpha}\right], \quad (3\text{-}16)$$

The $A_3(\Delta\nu,\alpha)$ coefficient depends weakly on α and its limiting values are $A_3(\alpha = 0) = 1$, $A_3(\alpha = \infty)=15/16$. For our sample, g~ 7 and α~ 3 [79]. From the measurement of $(C-C_1)$ at $\Delta r = 0$, we find $(2/3g)\ A_2 = 0.076$ giving $A_2 = 0.87$. This is in agreement with the theoretical prediction for A_2 in Eq. 3-16, which is equal to 0.8719.

3.3.5 Degree of long-range correlation

Let's consider C for ΔR = 0 and rearrange the Eq. 3-15 for the case of ΔR = 0, thus F(ΔR) = 1 in terms of multiplicative, additive and constant terms as following:

$$C(\Delta r) = F(\Delta r) + (\frac{2}{3g} A_2 + \frac{4}{15g^2} 2A_3)(1 + F(\Delta r)), \quad (3\text{-}17)$$

If define κ as the value of C when F = 0, with this definition we get the values of $\kappa = (\frac{2}{3g} A_2 + \frac{2}{15g^2} 2A_3)$. We can then write,

$$C(\Delta r) = F(\Delta r) + \kappa(1 + F(\Delta r)).$$

The parameter κ is the correlation when the detector is displaced considerably more than the correlation length,, Δr >> δr, for a monochromatic incident wave, where F vanishes. In this case, the short-range contribution to C, F(Δr), approaches zero. On the other hand, when Δr=0, F(Δr) =1, C(Δr=0) = 1 + 2κ = var(s_{ab}) gives the variance of normalized transmission coefficient. Random matrix theory (RMT) for quasi-1D geometry gives the variance of normalized total transmission var(s_a) = 2var(s_{ab}) – 1[38]. Combining two results, gives the degree of long-range correlation is equivalent to the fluctuation of total transmission, κ = var(s_a), in absence of absorption. Thus, the long-range intensity correlation of temporally coherent waves through a mesoscopic sample leads to a dramatic enhancement in fluctuations of total transmission.

Therefore, the spatial intensity correlation function depends only on the functional form of *F(x)* and the single parameter, κ for the single incident mode. It is noteworthy that localization and fluctuation are linked in many ways. In the absence of absorption, in the diffusive regime, var(s_a) is inversely proportional to the average of the dimensionless conductance g, which is the scaling parameter of the Anderson localization transition, var(s_a) = 2/3g. When g~1, var(s_a) ~ 2/3, Anderson localization occurs.

3.4 Conclusion

In conclusion, we have found the connection between the field and intensity correlation functions in the spatial structure of the three contributions to the cumulant intensity correlation functions. All terms can be expressed in terms of a single form factor, obtained from field correlation function. We have demonstrated the multiplicative character of C_1 and the additive character of C_2. Diagrammatic calculation predicts a mixed character for C_3 term, which includes a multiplicative, an additive, and a constant term of equal amplitude. From the feature of each term, reorganization the intensity correlation function in terms of multiplicative, additive and constant terms introduces the important localization parameter, the degree of long-range correlation, κ. We will further discuss this quantity by the correlation function in time domain and thereby unscrambling the effect of correlation and absorption.

We have carried out the measurement of full speckle pattern which allows us to study the statistics of total transmission normalized by ensemble average, $s_a = T_a/\langle T_a \rangle$. The distribution of the field in the random ensemble can be seen to be a mixture of Gaussian distribution weighted by the total transmission distribution $P(s_a)$ [38.84] written as:

$$P(r,i) = \int_0^\infty ds_a P(s_a) \frac{1}{\pi s_a} \exp(-(r^2 + i^2)/s_a), \quad (3-18)$$

where r and i are real and imaginary parts of field, respectively. Since $s_{ab} = r^2 + i^2$, the intensity distribution $P(s_{ab})$ is related with $P(s_a)$ [38] as $P(s_{ab}) = \int_0^\infty ds_a P(s_a) \frac{1}{s_a} \exp(-s_{ab}/s_a)$. This can be interpreted that if field E normalized by $\sqrt{s_a}$ in each configuration, defined as $E' = E/\sqrt{s_a}$, then the conditional distribution of the normalized field is independent of s_a. Letting r' and i' real and imaginary parts of E', $P(r', i' \mid s_a) = \frac{1}{\pi} \exp[-(r'^2 + i'^2)]$. This implies that E' and s_a are statistically independent and the probability distribution of E' is Gaussian. Therefore, the field correlation function of E with frequency shift can be written as the product of the field correlation function of E' and the correlation function of $\sqrt{s_a}$ with frequency shift:

$$F_E(\Delta\nu) = F_{E'}(\Delta\nu) \times C_{\sqrt{s_a}}(\Delta\nu), \quad (3-19)$$

Above expression suggests that the mesoscopic fluctuation from configuration

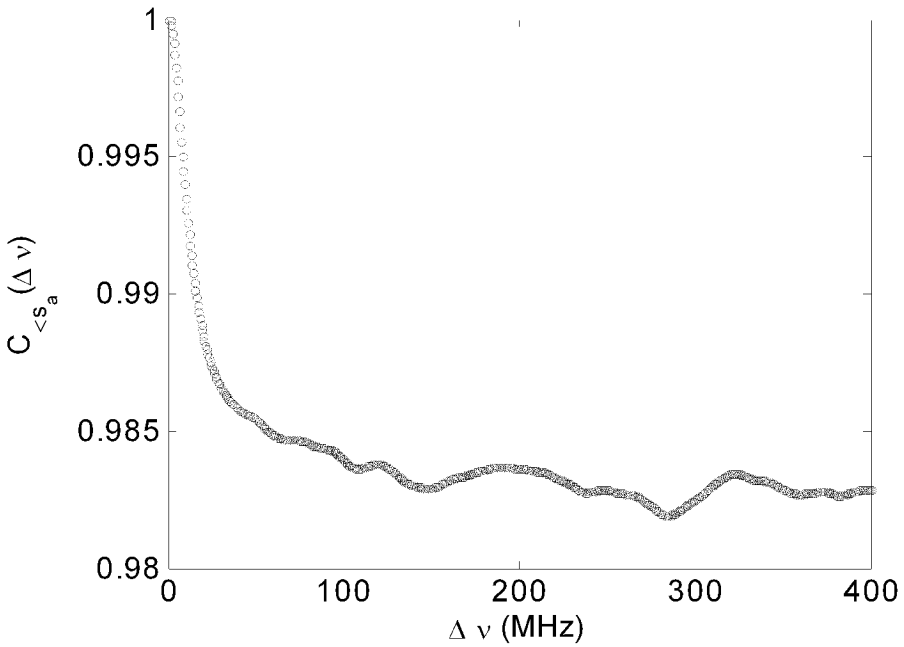

Figure 3-13: The spectral correlation of the square root of normalized total transmission, $C_{\sqrt{s_a}}$ for polystyrene sample

to configuration gives arise of the deviation from Gaussian Statistics. Fig. 3-13 shows the correlation function of the square root of normalized total transmission, $\sqrt{s_a}$ for polystyrene quasi-1D sample discussed in this chapter.

CHAPTER 4

DYNAMIC SPATIAL CORRELATION IN QUASI-1D RANDOM SAMPLE

4.1 Introduction

The statistics of steady-state classical wave propagation [2,30,85] and electronic conductance [86] in disordered system reflect the superposition of partial waves following trajectories with a wide distribution of path lengths, s, which is proportional to the particle time-of-flight distribution. The impact of wave interference on average transport with multiple-scattering sample is proportional to the likelihood that a meandering wave trajectory will return to a typical coherent volume, $V_c \sim (\lambda/2)^3$, which increase with s. Mesoscopic transport is characterized by the degree of non-local intensity correlation, which reflects the closeness to the Anderson localization threshold. In the last chapter, we showed that the steady state spatial intensity correlation function is the sum of multiplicative, additive and constant terms with respect to the square of the field correlation function with displacements of source and detector. Similar structure is observed in mesoscopic correlation of transmitted intensity with shift in polarization of microwave transport through a quasi-one-dimensional

resonant random sample [41]. In that study, the higher-order constant contribution can be clearly seen since g ~ 2.3, so that transport is close to the localization threshold. Mesoscopic correlation is linked to the localization, which can be characterized statistically by anomalous large fluctuation of normalized total transmission, $var(s_a)$. The degree of long-range correlation, κ, which is the fractional correlation of fluctuations in intensity at points at which the field correlation function vanishes, is equal to $var(s_a)$, $\kappa=var(s_a)$. Indeed, κ determines the closeness to localization even in the presence of absorption, which alters the distribution of trajectories of partial waves passing through the sample. In the steady-state case, absorption is entangled with localization. Consequently, the conventional localization parameter, g, in absorbing samples breaks down since its value decreases with increasing absorption though the wave is surely not localized by absorption. However, at a given delay time, t, from a narrow exciting pulse, all partial waves have the sample path length, $s = vt$. The intensity change intensively due to absorption becomes a common factor, $e^{-t/\tau a}$, where τ_a is the absorption time within the sample. Therefore, the suppression of transport by weak localization at a fixed time can be examined independently of the effect of absorption, which is given by the simple exponential factor. Furthermore, the path length increases with time and the longer path lengths having a higher probability of forming recurrent loop within the sample. Thus, the impact of weak localization could be expected to build in

time [23,87-96]. In the other word, $\kappa=var(s_a)$ is expected to increase with time. Since the feasibility of studying the isolated path length by carrying out pulse evolution measurement for classical wave, it allows us to investigate the variation of weak localization in time. In weak scattering sample, the pulse profile can be presented by the ensemble average of time-resolved transmitted intensity, <I(t)>. Diffusion theory predicts that transmission will decay exponentially with decay rate $\pi^2 D/(L+z_0)^2$, where D is diffusion coefficient and L is the sample length. However, increasing weak localization with time delay would reduce the rate of transport with time and might be characterized in terms of a time dependent diffusion coefficient $\pi^2 D(t)/(L+z_0)^2$ [93,95-97]. The observation of time dependent diffusion coefficient, D(t), in the transmitted pulse through quasi-1D random sample for microwave radiation has been reported [96].

To achieve a systematic understanding of weak localization in the time domain, it is essential to examine the statistics of propagation in addition to ensemble-average transport. This can be accomplished by parsing transmission according to the delay from an exciting pulse and studying the correlation and probability distribution of intensity as a function of delay time.

In this chapter, we report microwave measurements of the time-resolved field transmitted through random quasi-1D dielectric samples following an exciting pulse. This is achieved by Fourier transforming the

product of the frequency-domain transmitted field spectrum and Gaussian envelope into time domain. The Gaussian envelope is the Fourier transform of Gaussian incident pulse. Section 2 introduces the samples and setup of measurements involved. Section 3 gives main results of dynamic correlation and distribution. We find that the normalized field correlation is independent of time delay and identical to the steady state results shown in chapter 3. We found further that, with single source, the normalized intensity correlation function for an incident narrow pulse of bandwidth σ at delay time t is a function only of field correlation function and $k_\sigma(t)$, the residual degree of intensity correlation function at points at which the field correlation function vanishes. The probability distribution of normalized intensity, $P(s_{ab}(t))$, has the same form as for the steady-state transmitted intensity distribution [38,39], but with $2/3\kappa_\sigma(t)$ substituted for g. We find that even in diffusive samples, $\kappa_\sigma(t)$ may reach values exceeding the steady-state value at Anderson localization threshold[12] of $\kappa \cong 2/3$ [35]. The steady state may be seen as the limiting case of dynamic statistics, in which the incident pulse bandwidth vanishes, $\sigma \to 0$, $\kappa_{\sigma=0} = \kappa$.

4.2 Experimental setup and Data analysis of measurement for the time-resolved field

Spectral measurements of the field transmission coefficient of microwave radiation as a function of displacement and rotation of linear polarization are made with use of HP8722C vector network analyzer in an ensemble of random dielectric samples in which wave is diffusive. The samples are enclosed in a OFHC copper circular waveguide with open ends of length L greatly exceeding its 7.3-cm diameter. New realizations are produced by tumbling the sample briefly about its axis.

Spatial correlation measurements were carried out with the same setup

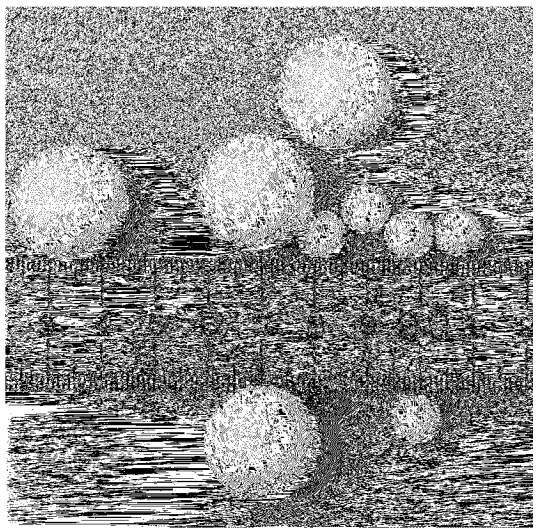

Fig. 4-1: Scheme of the alumina sample with 0.95-cm-diameter alumina sphere embedded in 1.9 cm Styrofoam

and sample as described in chapter 3, in which the steady state degree o f correlation was found to be $\kappa_0 = 0.06$.

Measurements of the dependence of the field and intensity correlation with polarization rotation are for microwave radiation transmitted through a random resonant dielectric sample with use of a pair of conical horns for launching and detecting the field. The source horn, S, emits linear polarized microwave radiation while the detector, D, receives horizontally or vertically

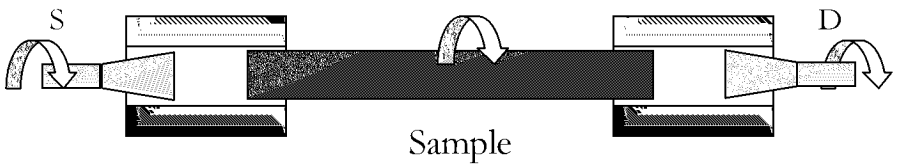

Fig.4-2: Scheme of experiment setup with polarization rotation. Both incident and output sections are enclosed in absorbing chamber.

polarized components of the transmitted field. The source, detector and sample tube are carefully aligned to be coaxial and rotate independently about this axis. Both source and detector are placed about 40 cm from the sample surface and connected with one-direction-transmitted microwave thermo-isolators to prevent multiple reflections within the system. Samples are composed of 0.95-cm-diameter alumina spheres with index of refraction 3.14 embedded in styrofoam spheres of diameter 1.9 cm and index of refraction 1.04 at an alumina volume fraction of 0.068 (see Fig. 4-1). Results are obtained from an

ensemble of 10000 alumina configurations of L = 61 cm (sample A) over the frequency range 14.7 ~ 15.7 GHz in a sweep with steps of 625 kHz for a single orientation of the horn detector. Measurement are also carried out in an ensemble of 12000 alumina configurations of L = 90 cm (sample B) over the frequency range 16.95 ~ 17.05 GHz in 1MHz frequency resolution for seven orientations of the horn detector rotated in step of 15° over a range of 90°. The experimental setup is shown in Fig. 4-2. Steady-state measurements of intensity correlation give $\kappa_0 = 0.09$ in sample A and $\kappa_0 = 0.29$ in sample B [41].

The alumina sample can open a narrow window of photon localization[33] in quasi-1D geometry in frequency. Mie resonances for high-index spherical sphere help to achieve strong scattering. This requires the low concentration of scatterers in order to maintain the resonant peaks. Figure 4-3 shows the frequency dependence of scattering cross section Q_{scat} for alumina sphere with diameter 0.95 and index of refraction 3.14. Peaks correspond to Mie resonances. Slightly above first Mie resonance (9.95 ~ 10.15 GHz) localization is observed. The localization parameter $var(s_a)$ is well above the localization threshold value *2/3* [98]. The frequency range (16.95 ~ 17.05 GHz) for sample B is centered at the peak of forth Mie resonance and is much narrower than the width of the resonance so that propagation parameters within this range are nearly constant. At $\nu = 17$ GHz, the number of transverse channels in the sample tube is $N = Ak^2/2\pi = 84$. The transport mean free path

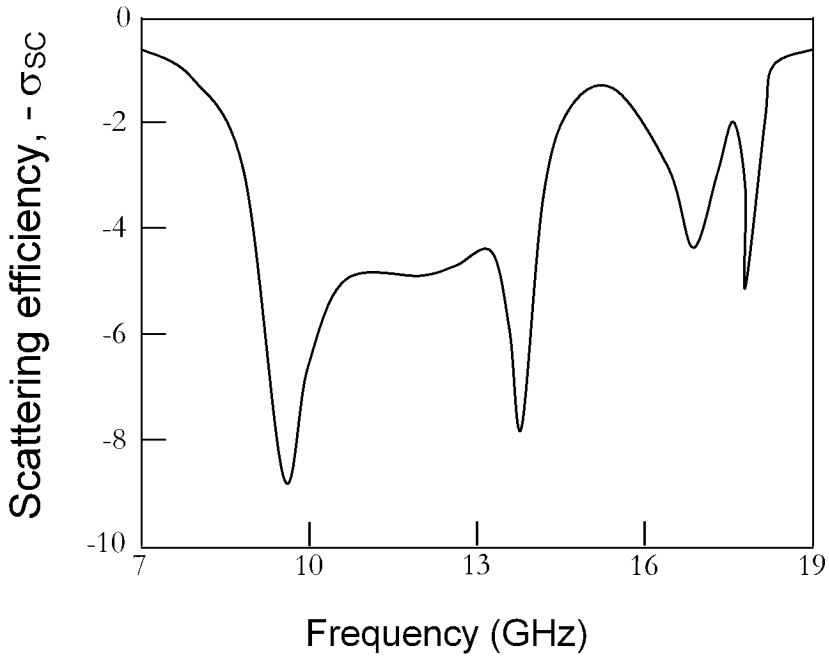

Fig. 4-3: Scattering efficiency $-\sigma_{sc}$ of Mie scattering of 0.98-cm-diam alumina sphere as the function of frequency.

is estimated from Mie theory to be l = 2.34 cm. A fit of diffusion theory to the measured spectral field correlation gives D = 8.0 cm^2/ns and absorption length L_a = 24.9 cm.

The Gaussian pulse profile with carrier frequency ν_0 is obtained by Fourier transformation of the product of the field transmission spectra and a Gaussian spectral envelope with bandwidth σ, $G(\nu) = e^{-\frac{(\nu-\nu_0)^2}{2\sigma^2}}$. An example of this process is shown in Fig. 4-4. The incident pulse excitation then obtained by Fourier transformation of the spectral Gaussian envelope so that the pulse

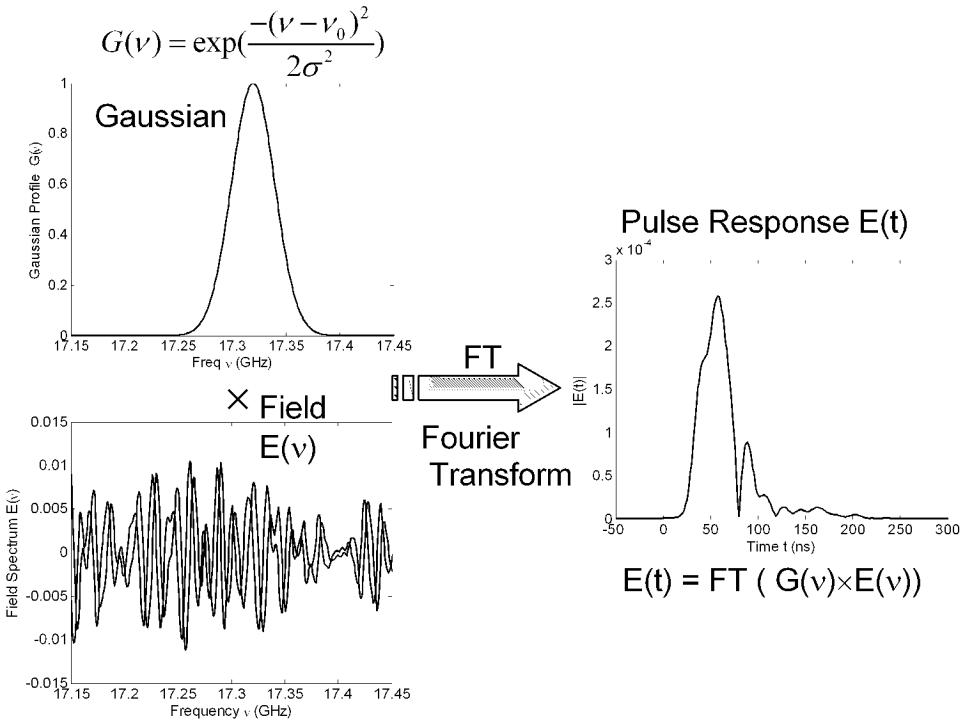

Fig.4-4: Example of Fourier transformation from typical spectral field to pulse responds field respect to the Guassian pulse with carrier frequency ν_0 and bandwidth σ.

width is $\sigma_t = \frac{1}{\sqrt{2\pi}\sigma}$. The temporal response of the intensity is the modulus square of temporal field, E(t), $I(t) = |E(t)|^2$. The ensemble average of time-resolved intensity, $\langle I(t) \rangle$, gives the time-of-flight distribution.

The temporal response to excitation pulses with three different values of σ in a single realization of sample A are shown in Fig. 4-5 (a) as a function of the delay from the center of the incident pulses in units of the diffusion time $t_D = \frac{(L+z_0)^2}{\pi^2 D}$, where D = 39.4 cm^2/ns is the diffusion coefficient and z_0 =

9.6cm is the boundary extrapolation length [96]. The temporal oscillations in transmitted intensity are due to the superposition of randomly phased transmitted waves over the bandwidth σ. The width of fluctuations is seen to

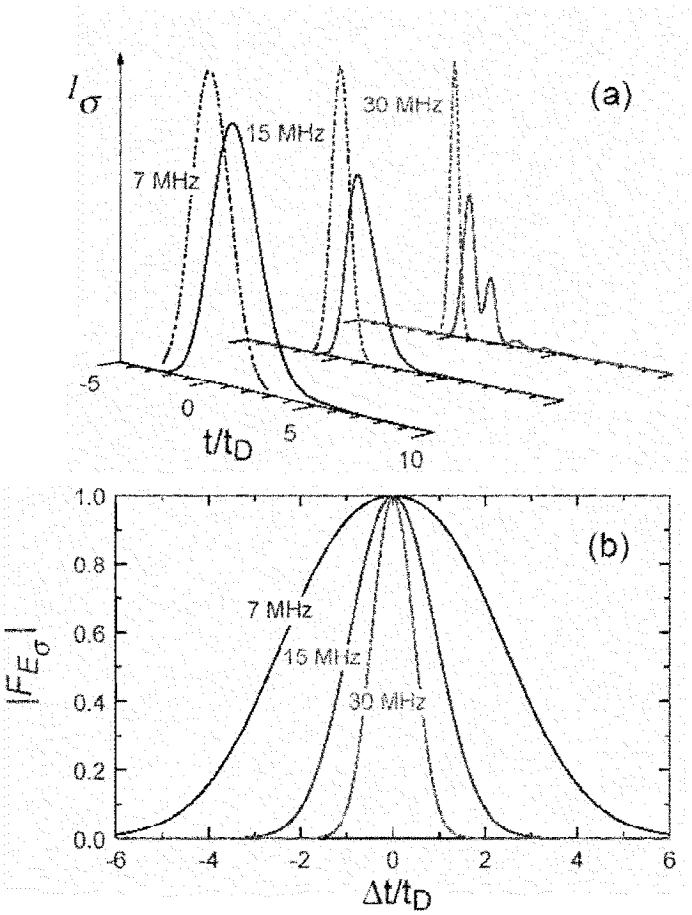

Fig. 4-5: (a) Transmitted intensity through a random realization of sample A (solid line) following incident Gaussian pulses (dashed curve) with σ = 7, 15, 30 MHz. The incident pulses are centered at t = 0 and shown with the same height. (b) Absolute value of the field correlation function $E_\sigma(t)/ <I_\sigma(t)$ with time shift for the values of σ in (a).

be approximately equal to the incident pulse width. This can be expressed quantitatively via the correlation function with time shift Δt of the transmitted field normalized to the square root of the ensemble average of the time varying intensity at time t,

$$F_{E^{\sigma}}(\Delta t) = \frac{< E_{\sigma}(t) E^{*}_{\sigma}(t+\Delta t) >}{\sqrt{< I_{\sigma}(t) >< I_{\sigma}(t+\Delta t) >}}, \quad (4\text{-}1)$$

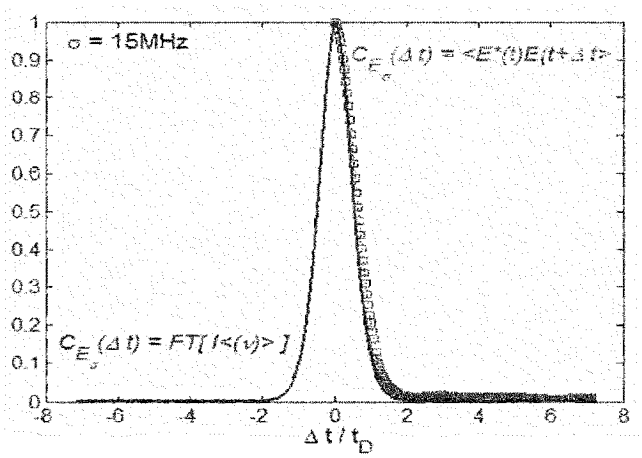

Fig. 4-6: The temporal field correlation function and the power spectrum with Gaussian profile are the Fourier transformation pair. Solid line is the Fourier transformation of Gaussian profile of incident pulse. Square curve is the temporal field correlation function.

which forms the Fourier transformation pair with the power spectrum with Gaussian profile (Fig. 4-6).

In addition, though $I_{\sigma}(t)$ in any given realization depends strongly upon the bandwidth, its ensemble average, $\langle I_{\sigma}(t) \rangle$, depends only weakly upon

bandwidth for $t > t_D$, once $\sigma > 1/\pi^2 t_D$ (Fig. 4-7). However, the noise level increase with decrease of σ.

4.3 Results and discussion

4.3.1 Dynamics of spatial correlation function

In weakly scattering systems excited by a narrow incident pulse, an initial ballistic burst of unscattered radiation is transmitted through the sample followed by a broad pulse of multiple-scattered radiation. The temporal variation of this pulse average over a random ensemble is well approximated

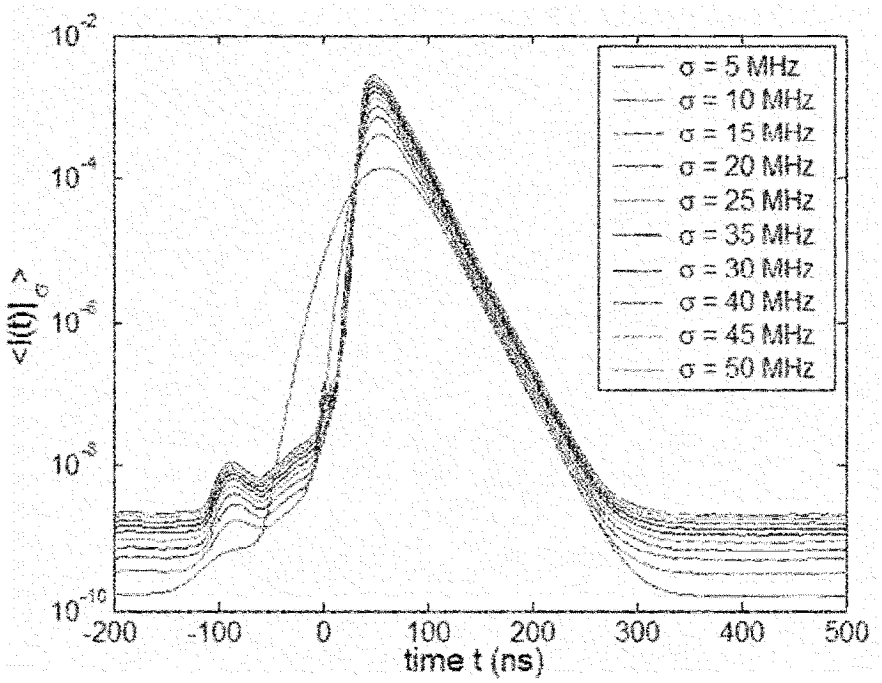

Fig.4-7: Pulse response for Polystyrene random ensemble $<I_\sigma(t)>$ depends weakly upon the bandwidth σ of Gaussian envelope, once $t > t_D$ = 56ns.

by the solution of the time dependent diffusive equation [76,79,99-102]:

$$I(x,t) = \sum_{n=1}^{\infty} \sin\frac{2\pi n(l+z_0)}{(L+2z_0)} \sin\frac{2\pi n(x+z_0)}{(L+2z_0)} e^{-t(n/t_D+1/\tau_a)}, \quad (4-2)$$

where t_D is the transport time through random sample and x is the longitudinal position within the sample of length L and t is the time from the center of the incident pulse. The diffusion intensity reaches an asymptotic single exponential decay shortly after the peak in pulsed transmission with decay rate equal to the sum of leakage rate of energy out of the lowest diffusion mode n = 1, $1/t_D$ and the absorption rate $1/\tau_a$, $1/\tau_a = 1/\tau_D + 1/\tau_a$.

We investigated the spatial correlation function of the field and intensity for waves with different delay time *t* in polystyrene random sample, in which waves propagate diffusively with g ~ 7. Fig. 4 – 8(a) shows the field correlation functions, $F_E^{\sigma}(\Delta r, t)$, where Δr is the detector displacement along the output surface for a single source, at delay times, $t = 3.5t_D$ (triangle curve), $4.8t_D$ (diamond curve) and for monochromatic excitation (CW case) (square curve). For this sample, the averaged transport time is 56 ns. The bandwidth of the Gaussian envelope is 20 MHz, which is greater than the correlation frequency $\delta\nu \sim 7$ MHz for this sample. The logarithm of the average pulsed transmission through the sample normalized by the average steady-state transmitted intensity is shown in the inset. The overlap of these curves

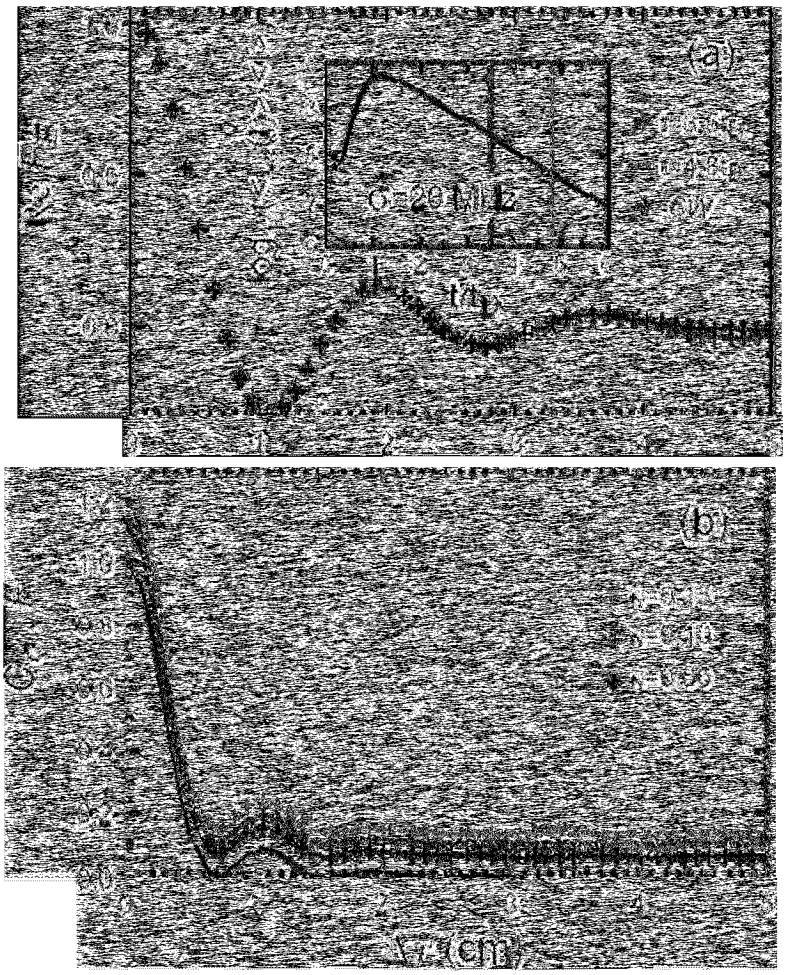

Figure 4-8: (a) Real part of spatial field correlation function at different time delay $t = 3.5t_D$, $4.8t_D$ and corresponding steady-state case. (b) Intensity spatial correlation function at different time delays as shown in (a) give increasing of κ. Solid line is the square of field correlation function. Inset shows the incident Gaussian pulse with bandwidth 20 MHz.

indicates that the field spatial correlation function is independent of time *t* and the same form as with the steady-state field correlation function.

The corresponding intensity correlation functions, shown in Fig.4-8(b), have the functional form as:

$$C_\sigma(\Delta r, t) = F(\Delta r) + \kappa_\sigma(t)(F(\Delta r)+1), \qquad (4-3)$$

with time-dependent parameter, $\kappa_\sigma(t)$. $\kappa_\sigma(t)$ is determined from the residual correlation at displacements $\Delta r > 3.5$ cm, which is greater than the correlation length, and equal to the time-dependent variance of intensity as:

$$\mathrm{var}_{s_{ab}}^{\sigma}(t) = C_\sigma(0,t) = 1 + 2\kappa_\sigma(t), \qquad (4-4)$$

The signal to noise ratio is significant low at long times at the tail of the pulse. Compare to the steady-state result, at time $t = 3.5t_D$, $\kappa_\sigma(t) \sim 0.10$; and $\kappa_\sigma(t) \sim 0.13$ at time $t = 4.8t_D$.

4.3.2 Dynamics of correlation function with polarization rotation

Transmitted fields are depolarized for multiple scattered waves, the average intensity is independent of the polarization of the field at the source or detector, and fields with perpendicular polarization are uncorrelated. Thus the field with polarization rotation $\Delta\theta$ from θ can be express by the superposition of two perpendicular components $E(\theta)$ and $E(\theta+\pi/2)$ as $E(\theta+\Delta\theta) = E(\theta)\cos\Delta\theta + E(\theta+\pi/2)\sin\Delta\theta$ so that the field correlation can be expressed as [41,80]:

$$F_E(\Delta\theta) = \left\langle \frac{E(\theta)}{\sqrt{\langle I(\theta)\rangle}} \frac{E^*(\theta+\Delta\theta)}{\sqrt{\langle I(\theta+\Delta\theta)\rangle}} \right\rangle \qquad (4\text{-}5)$$

$$= \left\langle \frac{E(\theta)}{\sqrt{\langle I(\theta)\rangle}} \frac{E^*(\theta)}{\sqrt{\langle I(\theta)\rangle}} \cos\Delta\theta \right\rangle$$

$$+ < \frac{E(\theta)}{\sqrt{< I(\theta) >}} \frac{E^*(\theta + \pi/2)}{\sqrt{< I(\theta + \pi/2) >}} \sin \Delta\theta > = \cos \Delta\theta$$

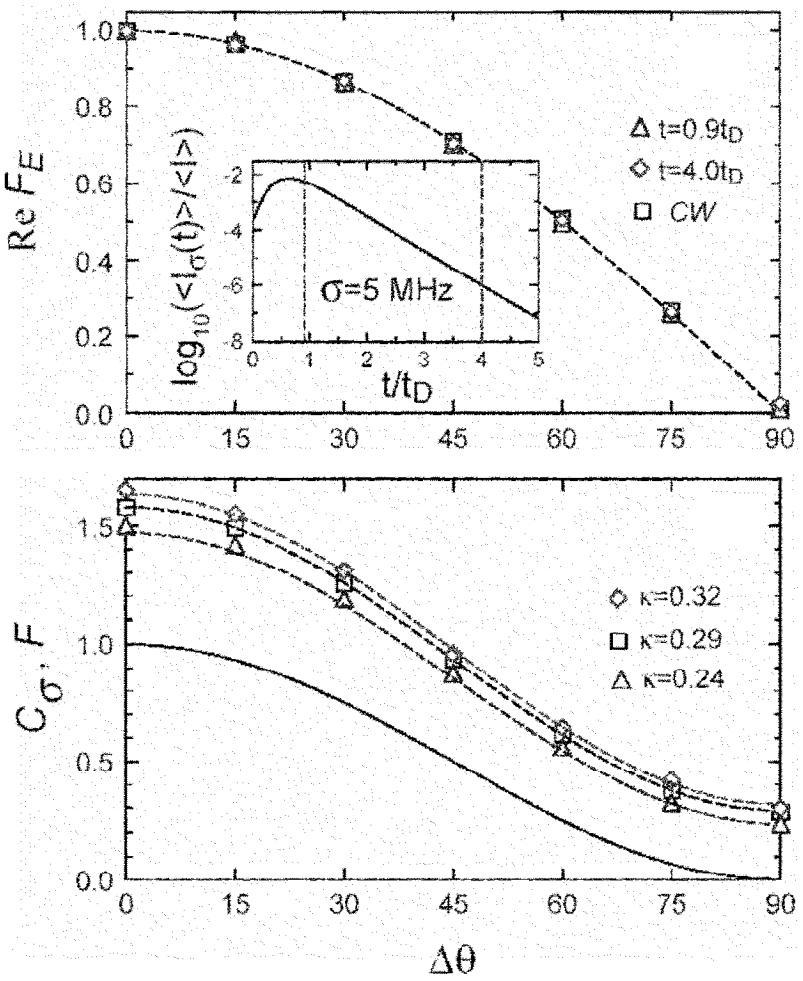

Figure 4 – 9: (a) Field correlation function with polarization rotation at different time delays t = $0.9t_D$, $4.0t_D$ and corresponding steady-state case. (b) Intensity correlation function with polarization rotation at different time delays as shown in (a) give increasing of κ. Solid line is the square of field correlation function. Inset shows the incident Gaussian pulse with bandwidth 5 MHz.

since the second term vanishes. This field correlation function is shown in Fig. 4-9(a) for two delay times indicated by the vertical lines in the inset for the

incident pulse of bandwidth σ = 5 MHz and for the static case. All functions are well described by the steady-state result shown in Eq. 4-3.

The corresponding intensity correlation functions are shown in fig. 4-9(b) with the same form as for the spatial correlation function:

$$C_\sigma(\Delta\theta, t) = F(\Delta\theta) + \kappa_\sigma(t)(F(\Delta\theta)+1), \qquad (4-6)$$

For $t = 0.9t_D$, value of the degree of long range correlation is smaller than that found in steady-state, $\kappa_\sigma(t) = 0.24 < k_0 = 0.29$, while for $t = 4.0t_D > t_D$, value of the degree of long range correlation is greater than that found in steady-state, $\kappa_\sigma(t) = 0.32 > k_0$.

4.3.3 Dynamics of intensity probability distribution

In the limit of large g, the normalized transmission coefficient s_{ab} distributed according to Rayleigh's law [2], which leads to negative exponential decay, $P(s_{ab}) = e^{-sab}$. Non-local correlation leads to higher probabilities at large value of the intensity. The relationship between the probability distribution of intensity and total transmission for quasi-1D sample in absence of absorption was found by Kogan and Keveh [38] from random matrix theory in terms of g:

$$P(s_{ab}) = \int_0^\infty \frac{ds_a}{s_a} P(s_a) \exp(-s_{ab}/s_a). \qquad (4-7)$$

This is equivalent to the relationship between the moments of the distribution of s_a and s_{ab}, $\langle s_{ab}^n \rangle = n! \langle s_a^n \rangle$ for nth moment. When n = 2, this gives the link between the fluctuations of s_{ab} and s_a as

$$2\mathrm{var}(s_a) = \mathrm{var}(s_{ab}) - 1. \qquad (4-8)$$

Experimental studies of the probability distributions of transmitted intensity and total transmission normalized by their respective ensemble average, $s_{ab} = T_{ab}/\langle T_{ab} \rangle$, $s_a = T_a/\langle T_a \rangle$, in the random polystyrene sample confirmed these results [103].

In the limit of weak scattering in the absence of absorption, the distribution of total transmission is found from diagrammatic and from random matrix theory to be [39]:

$$P(s_a) = \int_{-i\infty}^{i\infty} \frac{d\upsilon}{2\pi i} \exp(\upsilon s_a - \Phi(\upsilon)), \qquad (4-8)$$

where

$$\Phi(\upsilon) = g \ln^2(\sqrt{1-\upsilon/g} + \sqrt{\upsilon/g}), \qquad (4-9)$$

is the generation function with the single parameter g. For $s_a >> 1$, $P(s_a)$ has a exponential tail while for $s_a << 1$ it essentially log-normal growth. It follows from Eq. 4-8 and 4-9, that $\mathrm{var}(s_a) = 2/3g$. This together with equivalence of degree of long-range correlation, κ, and fluctuation of total transmission, $\mathrm{var}(s_a)$, lead to a connection between correlation, fluctuation, and average

transmission as $\kappa = \mathrm{var}(s_a)=2/3g$. Therefore, Eq. 4-10 can be rewritten as follows:

$$\Phi(\upsilon) = \frac{2}{3\kappa}\ln^2(\sqrt{1-3\upsilon\kappa/2}+\sqrt{3\upsilon\kappa/2}), \quad (4\text{-}10)$$

which is only depended on the parameter κ.

The time-resolved as well as the corresponding steady-state probability distributions of normalized transmitted intensity $P(s_{ab})$ for three types of samples are shown in Fig. 4–10. The dashed curves in Fig.4–10 is obtained from the theoretical expression for steady-state intensity distribution $P(s_{ab})$ from Eq. 4-7, 8, 10. Curves 1 and 2 show the results for sample A to the same Gaussian incident pulse with bandwidth 15 MHz at different delay time, t/t_D = 13.5 and 8.6, respectively. Curves 2, 3, 4 are that for different Gaussian pulse with bandwidth 15, 7, 30 MHz at the same time delay, t/t_D = 8.6 in sample A. Average over wider bandwidth gives smaller value of κ. Curves 5, 6 show the results of $P(s_{ab})$ for sample B, which has larger κ and closer to localization. Curve 6 is the steady-state probability distribution. Curve 5 is the distribution at delay time $t/t_D = 0.9 < 1$ respected to the Gaussian pulse incidence with bandwidth 5 MHz. For shorter time delay, $\kappa(t)$ is smaller than the steady-state value; while for larger time delay $\kappa(t)$ is larger than the steady-state value. For larger time delay $t/t_D = 3.5 > t_D$, $P(s_{ab})$ for the polystyrene sample for a pulse with a Gaussian bandwidth of 20 MHz is shown in curve 7 and compared to

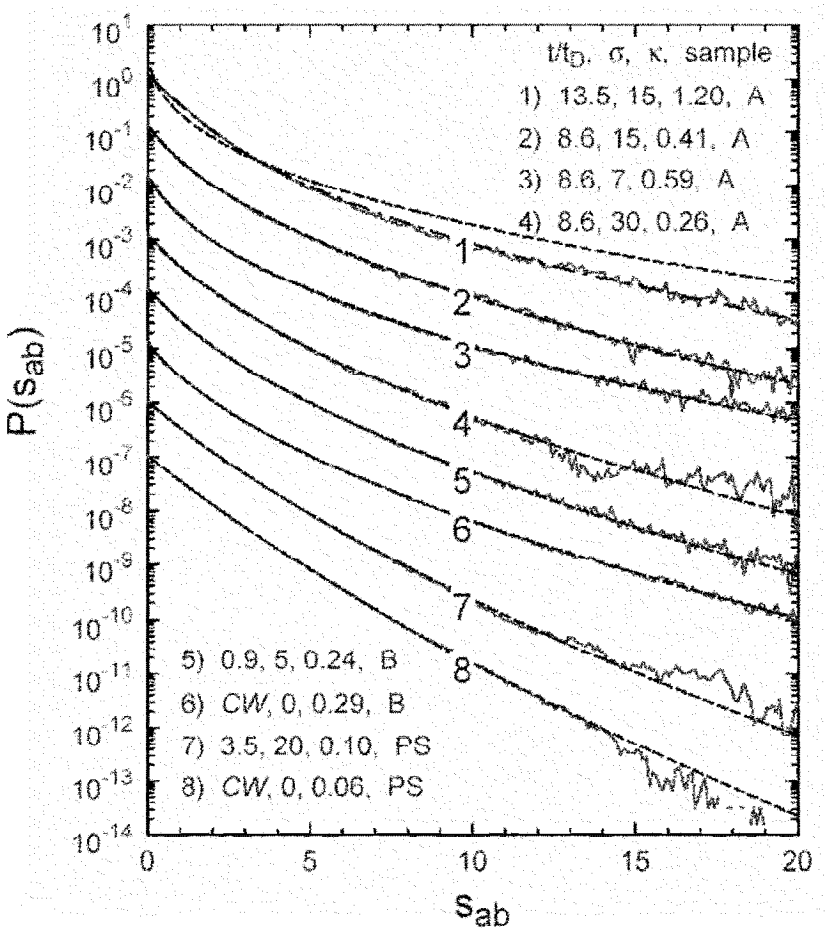

Fig.4–10: The time-resolved and corresponding steady-state probability distribution of normalized transmitted intensity P(Sab) for three types of samples.

the corresponding steady-state result shown in curve 8. Excellent agreement with measured results is obtained in all cases. These encompass both steady-state and dynamic propagation, in the presence of strong and weak absorption, for both weak and strong correlation regimes in which κ exceeds its value at the Anderson localization threshold of 2/3. The properties of these samples are shown in the following table:

	Polystyrene (n = 1.59)	Alumina (Resonant) n = 3.14	
		Sample A	Sample B
Sample Length L	100 cm	61 cm	90 cm
Vol. Filling Factor f	0.52	0.068	0.068
D Diffusion Coef.	33 cm^2/ns	39.4 cm^2/ns	39.4 cm^2/ns
Transport time t_D	56 ns	13 ns	25 ns
g	~7	~5	~ 2.3
# of config.	1380 (50 line scan)	10000	12000 (7 pol.Rotation)
Frequency Range	16.8 ~ 17.8 GHz	14.7 ~ 15.7 GHz	16.95 ~ 17.05 GHz
κ_0	0.06	0.09	0.29

4.4 Conclusion

The form $C = F + \kappa(1 + F)$ for single source introduces the parameter κ which characterizes wave transport and relate to the correlations, fluctuations, and average transport. In this chapter, we have extended this idea to time domain At the same time, $\kappa_\sigma(t)$ reflects the statistics of propagation even in presence of absorption In the limit of $\sigma \to 0$, $\kappa_\sigma \to \kappa_0$ yielding steady-state statistics. Thus, the time-varying degree of correlation, $\kappa_\sigma(t)$, is the controlling function of mesoscopic statistics. It is, therefore, of prime importance to

explore the possibility of a universal formulation of the time variation of the degree of correlation and its relationship to spatial localization.

CHAPTER 5

STATISTICS OF THE PHASE GRADIENT AND TRANSVERSE SPACE CURRENT DENSITY

5.1 Introduction

Each polarization component of the electromagnetic field can be represented by the complex field, $Ae^{i\phi}$, which obeys circular Gaussian statistics [2]. Both real and imaginary parts of the field are described by a normal distribution. Equivalently, the field amplitude A has a Rayleigh distribution while the phase ϕ has a uniform distribution between $-\pi$ and π. However, multiple scattering with crossing of wave trajectories leads to non-Rayleigh distribution, and weak localization modifies average wave transport. The distinct effect of localization on the statistical distribution of intensity [35] and phase[104] have been reported microwave experiments in quasi-1D sample. Large fluctuations are a consequence of interference, which distinguishes the diffusion of particle and waves and reflects the essential role played by the phase in statistics and dynamic aspects of mesoscopic physics.

To study phase statistics, we unwrap the phase so that discontinuous phase jump of $\pm 2\pi$ are removed leading to a phase which is not restricted to

the range of (-π, π). In addition, the occasional phase jumps by π which occur when moving across phase singularities, which are observed at positions at which the amplitude vanishes. At a phase singularity, both real and imaginary parts of complex field vanish and the phase which is tangent of the ratio of the imaginary and real parts of the field is then indeterminate. In our study of spatial the phase derivative, phase jumps of $\pm 2\pi$ are unwrapped in space to eliminate the 2π discontinuity as was done in frequency [105] and time domains [106]. The unwrapped phase may be represented as $\phi = \phi_{2\pi} + 2n\pi$, where n is an integer.

Phase statistics can reveal important details relating to wave dynamics. The single-channel delay time is defined as the first derivative of unwrapped phase delay with frequency for one outgoing channel *b* for one incoming channel **a**, $\phi'_{ab} = \frac{d\phi_{ab}}{d\omega}$. The intensity weighted single channel delay time, $W_{ab} = T_{ab}\frac{d\phi_{ab}}{d\omega}$, called the Wigner single channel delay time [107], is the key variable since that the sum of W_{ab} over all incoming and outgoing channels gives the density of state multiplied by $(\pi/2N)$[108], where N is the number of channels. Both experimental [104,109] and theoretical [104,109,110] results of the probability distributions of delay times for diffusive and localized waves has been studied

and are in excellent agreement. The probability distribution of the normalized delay time $\hat{\phi}' = \frac{\phi'}{<\phi'>}$ for diffusive waves is as following:

$$P(\hat{\phi}') = \frac{Q}{2[Q + (\hat{\phi}' - 1)^2]^{3/2}}, \qquad (5-1)$$

where Q is a dimensionless parameter calculated from the field spectral correlation function which is a function of $\alpha = L/L_a$. The probability distribution of W in the Gaussian approximation is given by:

$$P(\hat{W}) = \frac{1}{\sqrt{1+Q}} \exp\left(\frac{-2\hat{W}}{\Theta(\hat{W}) + \sqrt{1+Q}}\right), \quad (5-2)$$

where $\Theta(\hat{W})$ is the Heaviside step function and $\hat{W} = W / <W>$. As wave propagation approaches the localization regime, $P(\hat{W})$ shows large deviation from the prediction of Eq. 5 -2 in the large delay time limit. This is a dynamic signature of wave localization in dynamics of wave transport.

In this chapter, we investigate the statistical properties of the spatial derivative of phase in the transmitted speckle pattern with monochromatic microwave excitation in the weak scattering limit. The probability distributions, joint distribution with intensity, and spatial correlation of the phase derivative will be considered. One-to-one correspondence exists between the quantum probability current density from the Schrodinger

equation and the Poynting vector $\vec{S} = \vec{E} \times \vec{H} = \mathrm{Im}(E^*(r) < E(r))$ [111]. The current density of a scalar wave in the stationary case can be expressed as[112]:

$$J(r) = \mathrm{Im}(E(r)^* < E(r)), \qquad (5-3)$$

If we substitute the field, $E_v(r) = A(r)e^{i\phi(r)}$, into the equation, it shows that the product of intensity, $I = |A|^2$, we find:

$$J(r) = I(r) < \phi(r). \qquad (5-4)$$

The current can be understood as a flow of energy through the random medium with transport velocity v_E.

Along the horizontal line on the output surface, one component of transverse current density is obtained as: $J_x = I\frac{d\phi}{dx}$. The first spatial derivative of phase obtained from the discrete measurement is indeed the difference with finite step size Δx instead of the infinitesimal increment dx. We investigated the impact of finite step size on the theoretic prediction of the probability distribution $P(\frac{d\phi}{dx})$ and $P(J_x)$. When $\Delta x \to 0$, the continuous case is recovered.

The sample studied in this chapter is the Polystyrene sample described in Chapter 3. The measurements of complex fields for a single polarization component are carried out on the near-field output surface along a straight line with 1mm as well as 100 micron steps. To increase the spatial resolution for a

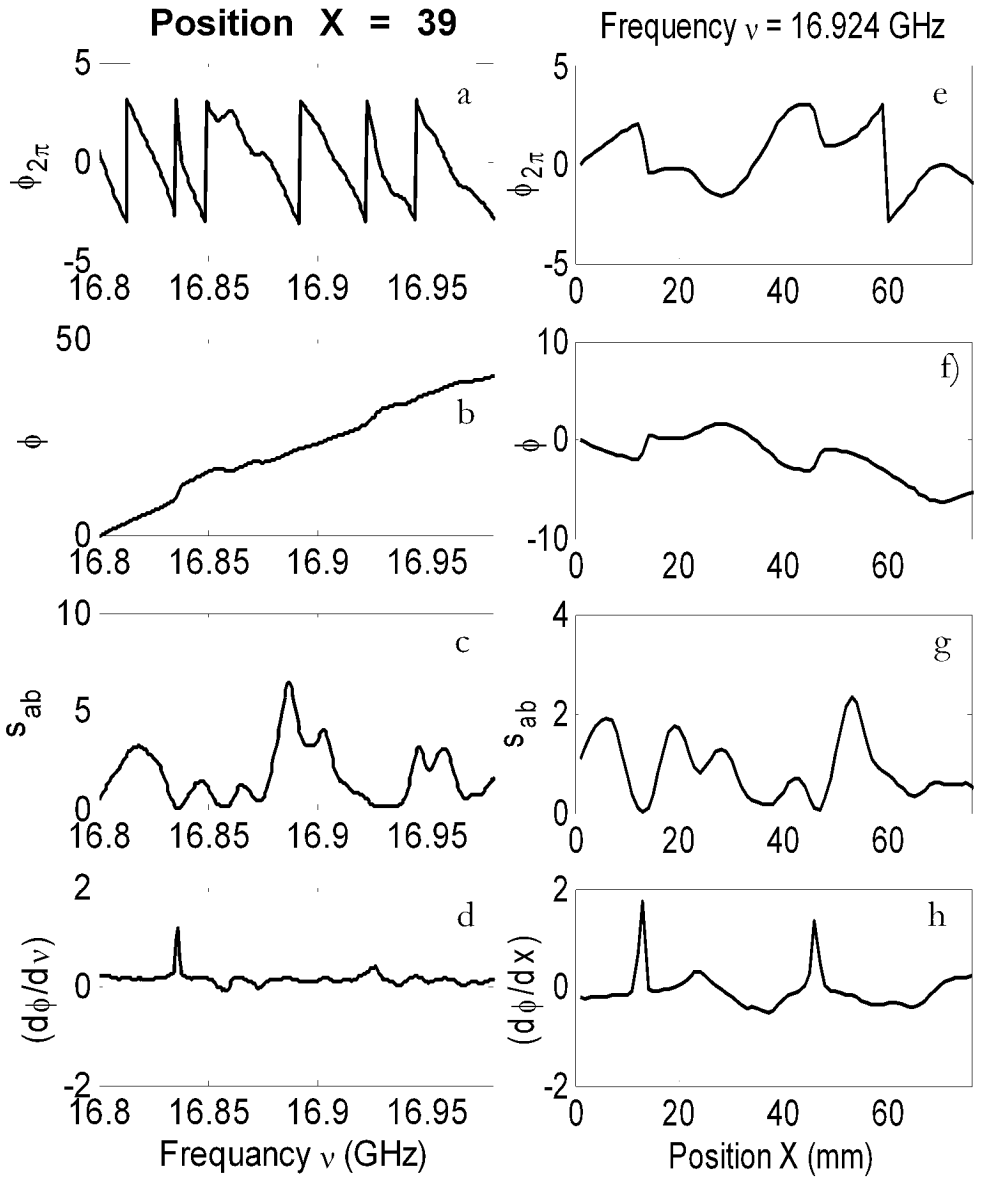

Fig.5 – 1: Phase of complex transmitted field wrapped in [π, π] cross over 5cm spatial range with sudden phase jump(a) and over frequency range (e); Unwrapped phase over space(b) and over frequency (f); Normalized transmission coefficient over space (c) and over frequency (g); corresponding first derivative of phase over space (d) and over frequency (h)

finer line scan of 500 positions with 100 micron step, the thinner wired

detector with core thickness 100 micron is chosen. The detector is perpendicular to the line along which the translation motion.

5.2 Phase map and correlation in space

Fig. 5-1 shows the wrapped phase in $\phi_{2\pi}$ and unwrapped phase ϕ, the intensity normalized by its ensemble average of intensity s_{ab}, and the first derivative of the phase. The four figures on the left presents functions of frequency. The zero of unwrapped phase in frequency domain should occur at frequency $\nu = 0$. The four figures on the right are the corresponding results for variation in space. It is worth to mention, unwrapping phase in space is path dependence. Here we unwrap phase straight along a x-axis along which the measurements were done. Large peaks in the spatial phase derivative are

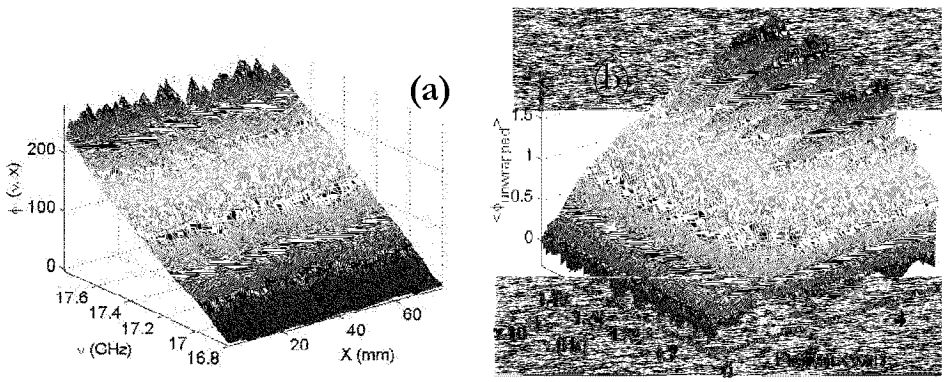

Fig. 5–2: 3D surface plots of unwrapped phases in frequency domain (a) and in space (b) as the function of frequency and position.

associated with small value of intensity. The corresponding surface plots of unwrapped phase in the frequency domain and in space over the frequency range from 16.8 ~ 17.8 GHz as functions of both frequency and position are shown in Fig. 5 – 2 (a), (b) respectively.

Normally, the measured phase of the field $Ae^{i\phi}$ is wrapped in 2π and is uniformly distributed:

$$P(\phi_{2\pi}) = \begin{cases} \frac{1}{2\pi} & (-\pi \le \phi \le \pi) \\ 0 & (other) \end{cases} , (5-5)$$

This is seen in the probability distribution shown in Fig.5–3 for the measurement of phase vs. microwave radiation frequency transmitted through the random Polystyrene sample over single point measurement over 15000 configurations.

For the unwrapped phase ϕ, we could compute the probability distribution $P(\phi)$ from single point field spectra measurement. Fig. 5–4 (a) shows the probability distribution of unwrapped phase fluctuation from its ensemble average, P ($\delta\phi/\sigma$), where $\delta\phi = \phi - \langle\phi\rangle$ and σ is the variance. The ensemble average of the unwrapped phase is seen in the inset of Fig.5-4, to increase monotonically with frequency.

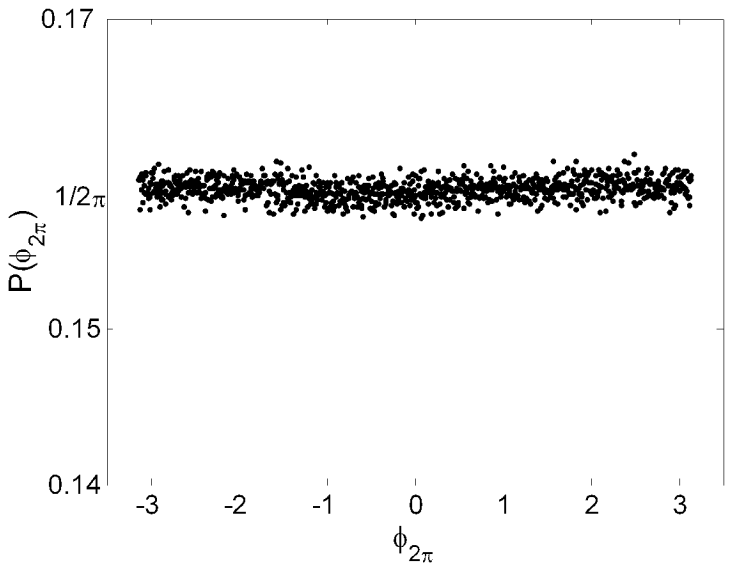

Fig. 5-3: The probability distribution of wrapped phase $P(\phi_{2\pi})$ shows uniform distribution in (π, π).

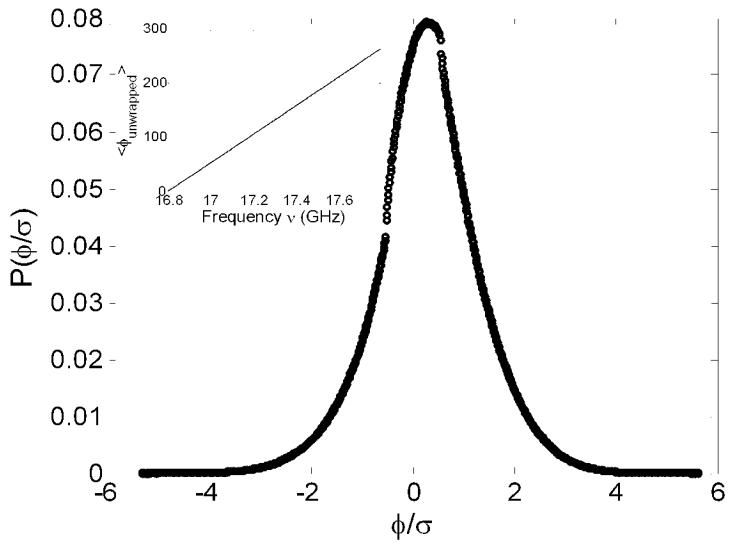

Fig.5–4: The probability distribution of unwrapped phase $P(\delta\phi/\sigma)$ shown in (a) gives Gaussian distribution, where $\delta\phi = \phi - \langle\phi\rangle$, and σ is the standard deviation. And $\langle\phi\rangle$ is the ensemble average of unwrapped phase

5.3 Statistics of the first spatial derivative of phase

5.3.1 Theoretical background

We will start our discussion with a brief summary on the statistical properties of the spatial derivatives of the phase based on Ref. [45] and [113], under the Gaussian approximation.

The monochromatic speckle pattern can be described as the sum of fields associated with a large number of partial waves as:

$$E = Ae^{i\phi} = \frac{1}{\sqrt{N}} \sum_{k=1}^{N} A_k e^{i\phi_k} , \qquad (5-6)$$

where A_k and ϕ_k are the amplitude and the phase of the k^{th} partial wave. Let r and i to be the real and imaginary part of corresponding field, respectively. Then the joint distribution function of four variables r, i, r_x, i_x can be expressed as [114]:

$$P(r,i,r_x,i_x) = \frac{1}{4\pi^2\sqrt{\det M}} \exp[-\frac{1}{2} uM^{-1}u^T], \qquad (5\text{-}7)$$

where $r_x \equiv \frac{dr}{dx}$, $i_x \equiv \frac{di}{dx}$, $u = [r \;\; i \;\; r_x \;\; i_x]$ and M is the 4×4 symmetric covariant matrix, in which each matrix element can be written in terms of correlators of real and imaginary parts of the field as:

$$M = \begin{bmatrix} <rr> & <ri> & <rr_x> & <ri_x> \\ <ir> & <ii> & <ir_x> & <ii_x> \\ <r_x r> & <r_x i> & <r_x r_x> & <r_x i_x> \\ <i_x r> & <i_x i> & <i_x r_x> & <i_x i_x> \end{bmatrix}. \qquad (5-8)$$

For Gaussian field statistics, the real and imaginary parts are uncorrelated to each other. It is also true that r, i, r_x, i_x are jointly Gaussian. So that,

$$<rr> = <ii> = \sigma^2, <ir> = <ri> = 0. \qquad (5-9)$$

By using the relation of $<ff>' = <(ff)'> = 2<ff'>$[115], we obtain:

$$<rr_x> = \frac{1}{2}\frac{\partial}{\partial x}<rr> = \frac{1}{2}\frac{\partial}{\partial x}(\sigma^2) = 0, \text{ and} <ii_x> = 0. \qquad (5\text{-}10)$$

Apply $R_{f^{(n)}g^{(m)}}(\Delta x) = (-1)^m \frac{\partial^{(n+m)}}{\partial \Delta x^{(n+m)}} R_{fg}(\Delta x)$ into the follow elements, obtain (see ref. [114] p317):

$$<r_x r_x> = -\frac{\partial^2}{\partial \Delta x^2} R_{rr}(\Delta x)\Big|_{\Delta x=0} \equiv b_x = <i_x i_x>,$$

$$<ri_x> = -\frac{\partial}{\partial \Delta x} R_{ri}(\Delta x)\Big|_{\Delta x=0} \equiv c_x = -<r_x i>, \qquad (5-11)$$

$$<r_x i_x> = <i_x r_x> = 0.$$

Therefore, substitute Eq. 5-9 to Eq. 5-11 into Eq. 5-8 gives:

$$M = \begin{bmatrix} \sigma^2 & 0 & 0 & c_x \\ 0 & \sigma^2 & -c_x & 0 \\ 0 & -c_x & b_x & 0 \\ c_x & 0 & 0 & b_x \end{bmatrix}, \qquad (5-12)$$

From this form, the determinant and the inverse of M are found to be:

$$M^{-1} = \frac{1}{\sqrt{\det M}} \begin{bmatrix} b_x & 0 & 0 & -c_x \\ 0 & b_x & c_x & 0 \\ 0 & c_x & \sigma^2 & 0 \\ -c_x & 0 & 0 & \sigma^2 \end{bmatrix}, \text{ and}$$

$$\det M = (\sigma^2 b_x - {c_x}^2)^2 . \qquad (5-13)$$

Letting $D = \sqrt{\det M}$, we then obtain:

$$p(r, i, r_x, i_x) = \frac{1}{4\pi^2 D} \exp[-\frac{1}{2D}(b_x(r^2 + i^2) + \sigma^2(r_x^2 + i_x^2) + 2c_x(ir_x - ri_x))], \qquad (5 - 14)$$

Transforming the variables of the probability distribution from *r, i, r_x, i_x to I, ϕ ,I_x ,ϕ_x,* where *,I_x* is the spatial derivative of intensity and ϕ_x is the spatial derivative of the phase gives:

$$\begin{aligned} & p(I, \phi, I_x, \phi_x) \\ & = p(r, i, r_x, i_x)\|J\| \qquad , \qquad (5-15) \\ & = \frac{1}{16\pi^2 D} \exp[-\frac{1}{2D}(b_x I + \sigma^2(\frac{I_x^2}{4I} + I\phi_x^2) - 2c_x I\phi_x)] \end{aligned}$$

where the $\|J\| = 1/4$ is the Jacobian. Integrating over *I,* ϕ*, I_x* to obtain the probability distribution of the first spatial derivative of phase ϕ gives:

$$p(\phi_x) = \frac{1}{2\sigma} \frac{\sigma^2 b_x - {c_x}^2}{\left(\sigma^2 {\phi_x}^2 - 2c_x\phi_x + b_x\right)^{3/2}}, \qquad (5-16)$$

Each of the parameter in this expression is important in our experimental study. The spatial field correlation function can be rewrite as:

$$\begin{aligned} C_E(\Delta x) &= < E^*(x)E(x+\Delta x) > \\ &= (R_{rr}(\Delta x) + R_{ii}(\Delta x)) + i(R_{ri}(\Delta x) - R_{ir}(\Delta x)) \end{aligned}, \qquad (5-17)$$

where $R_{rr}(\Delta x)|_{\Delta x=0} = R_{ii}(\Delta x)|_{\Delta x=0} = \sigma^2 = \frac{1}{2}\mathrm{Re}(C_E(\Delta x))|_{\Delta x=0}$. So at first, σ^2 is the variance of the real or imaginary parts of the field, which can be interpreted as half of the real part of field spatial correlation when the spatial displacement is zero, $\sigma^2 = \frac{1}{2}\mathrm{Re}(C_E(\Delta x))\Big|_{\Delta x=0}$. For the normalized field $C_E(\Delta x=0) = 1$, thus $\sigma^2 = 1/2$. Second, b_x is actually one half of the second derivative of the real part of field spatial correlation when the spatial displacement is zero, $b_x = -\frac{1}{4}\frac{\partial^2}{\partial \Delta x^2}\{\mathrm{Re}(C_E(\Delta x))\}\Big|_{\Delta x=0}$. Here, we can define the parameter $Q \equiv 2b_x$. Third, c_x is half of the first derivative of the imaginary part of the field spatial correlation function when spatial displacement is zero. Since the imaginary part of spatial field correlation function in our isotropic system vanishes, which has been shown is chapter 3, c_x is indeed zero. Therefore, we could write the expression of the probability distribution of the 1D phase gradient, which can be measured experimentally:

$$p(\phi_x) = \frac{1}{2}\frac{Q}{(Q+\phi_x^{\,2})^{3/2}}, \qquad (5\text{ - }18)$$

As a result of this expression, $p(\phi_x)$ only depends on the parameter Q, which can be expressed as half of the second derivative of the spatial field correlation function as $\Delta x \to 0$, $Q = -\frac{1}{2}\frac{\partial^2}{\partial \Delta x^2} C_E(\Delta x)\big|_{\Delta x \to 0}$.

5.3.2 Experimental results and the impact of finite step

The sample studied is composed of randomly positioned 1.27-cm-diam Polystyrene spheres at a volume filling fraction of 0.52 enclosed in a 1-m-long, 7.5-cm-diam copper tube. The amplitude and phase of microwave field

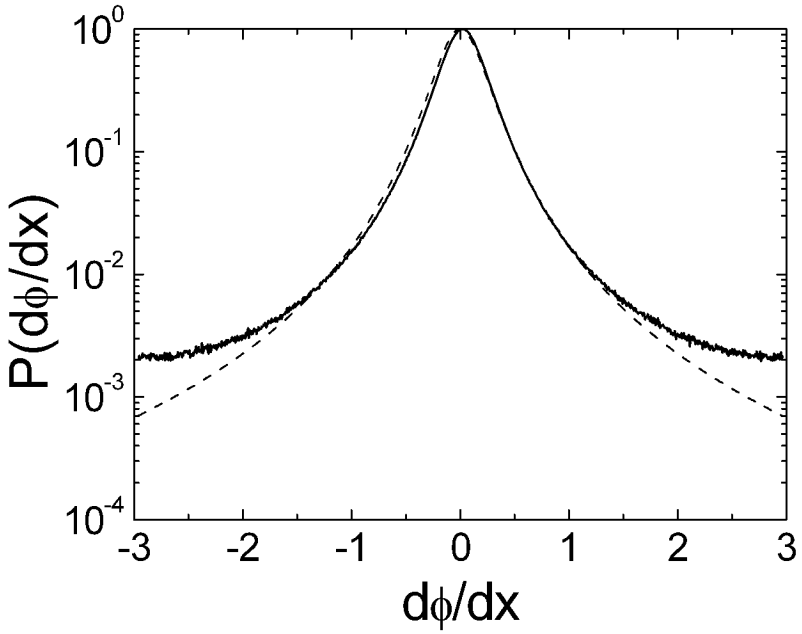

Fig. 5–5: The probability distribution of first derivative of phase $p(\frac{d\phi}{dx})$ with spatial resolution 1mm. Solid line is from experimental data and dashed line is theoretical result.

is measured with use of a Hewlett Packard 8722C vector network analyzer between 16.8 ~ 17.8 GHz, using frequency interval of 625 kHz. The wired detector with core diameter ~1mm is translated to 50 positions along the x-direction on the near-field output surface with 1.06 mm step size.

In order to obtain the first spatial derivative of the phase, phases measured modulus 2π at each frequency was unwrapped in space along the x-axis. The difference in phase at adjacent is then computed. The probability distribution $p(\frac{d\phi}{dx})$ shown in Fig.5 – 5 is computed over 500 configurations and 1600 frequencies. The figure gives a comparison of experimental result (solid curve) and the theoretical prediction (dashed line) by applying Eq.5-18 with parameter Q ~ 0.063 estimated from the second derivative of spatial field correlation function when Δx is zero. Since the $C_E(\Delta x = 0)$ includes higher noise which cannot be average out as uncorrelated correlation of noise at different position, Q is actually hard to determine accurately. The first moment of $\frac{d\phi}{dx}$ vanishes and the deviation at tails attracted our attention.

In the studies in which the detector is of translated with different step sizes such as 0.1 mm, 0.2 mm and 0.5 mm, we find that the finite size of Δx changes the tail of the distribution. Fig.5 -6 shows the $p(\frac{d\phi}{dx})$ with Δx is 0.1 mm, where the deviation of tail becomes much smaller. Thus leads us to

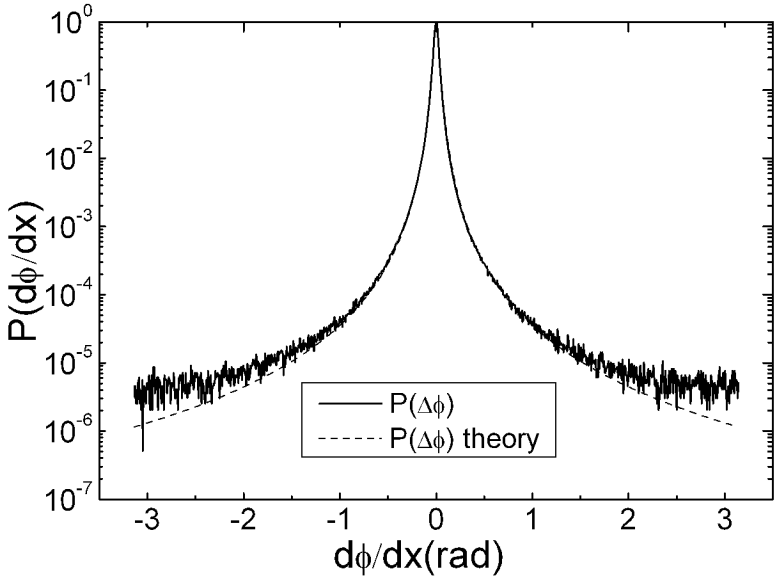

Fig. 5–6: The probability distribution of first derivative of phase $p(\frac{d\phi}{dx})$ with spatial resolution 0.1mm. Solid line is from experimental data and dashed line is theoretical result.

pursue the theoretical result for the probability distribution of $p(\frac{\Delta\phi}{\Delta x})$ with finite step, and eventually to take the limit of $\Delta x \to 0$ to recover Eq. 5 – 18.

In the following, the brief theoretical approach carried out by Bart van tigglen [116] will be shown below. For a finite translation step $\Delta x = x - x'$ is finite and for a field represents as $E(x) = A(x)e^{i\phi(x)}$. The four variable joint distribution of amplitudes and phases at position x and x' can be written as,

$$P(A, A', \phi, \phi')$$
$$= \frac{\mu^2}{\pi^2} AA' e^{-A^2} e^{-|z|^2 A^2 - \mu^2 A'^2 + 2|z|\mu AA'\cos(\phi - \phi' + \gamma)}, \qquad (5-19)$$

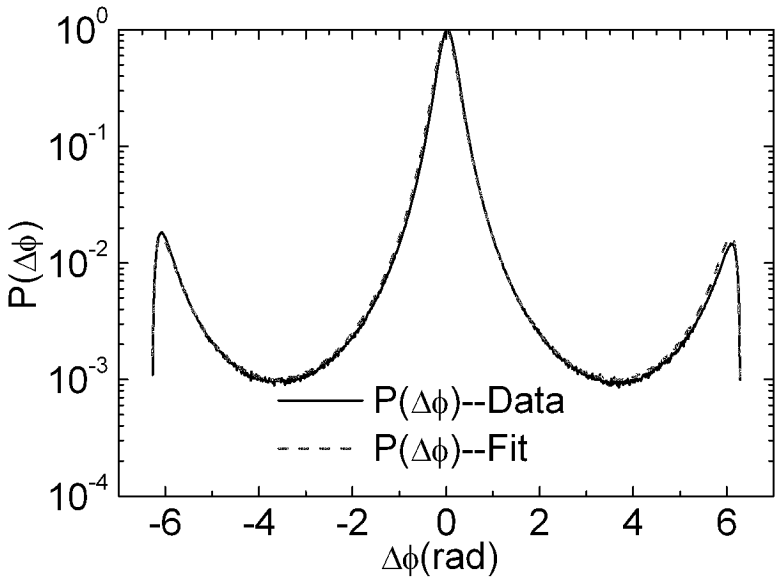

Figure 5 – 7: The probability distribution of first derivative of phase $p(\frac{\Delta\phi}{\Delta x})$ with considering the finite translating step. Black curve is calculated from data and red curve is the fit by using the parameter $C_E(\Delta x=1.06\text{ mm}) = 0.96366$

where z, μ and γ are defined by:

$$\frac{< E(x)E^*(x') >}{< I >} \equiv \frac{\overline{z}}{\sqrt{1+|z|^2}} = C_E(\Delta x) = \frac{\overline{z}}{\mu}, \qquad (5-20)$$

and $\mu^2 = 1+|z|^2$, $\overline{z} = |z|e^{i\gamma}$. The field spatial correlation function is shown to be real value in chapter 3, thus $\gamma = 0$. Then integrate Eq. 5-19 over $A(x)$, $A'(x')$, $\phi'(x')$ at constant $\Delta\phi(x) = \phi(x) - \phi'(x')$. Let $A = A\cos\theta$, $A' = A\sin\theta$, $\int_0^\infty dA \int_0^\infty dA'$ can be written as $\int_0^\infty AdA \int_0^{\pi/2} d\theta$, this gives:

$$p(\Delta\phi) = \frac{2\pi - |\Delta\phi|}{8\pi^2}(1 - C_E{}^2(\Delta x)) \int_0^{\pi} d\theta \frac{\sin\theta}{(1 - C_E(\Delta x)\cos\Delta\phi\sin\theta)^2}$$
$$= \frac{2\pi - |\Delta\phi|}{4\pi^2} \frac{1 - C_E{}^2(\Delta x)}{1 - C_E{}^2(\Delta x)\cos^2\Delta\phi} \times \qquad (5-21)$$
$$[1 + \frac{C_E(\Delta x)\cos\Delta\phi\cos^{-1}(-C_E(\Delta x)\cos\Delta\phi)}{\sqrt{1 - C_E(\Delta x)\cos^2\Delta\phi}}]$$

Note that the single parameter for this expression is the value of spatial field correlation at finite step size Δx. When Δx approaches zero, the expression recovers the expression of the continuous case in Eq. 5-18. Excellent agreement between the experimental result and the above result is shown in Fig. 5-7 with the parameter $C_E(\Delta x = 1.06mm) = 0.964$.

5.4 Statistics of current density

The transverse current density is defined in Eq. 5-4. In our measurements, we only consider x-component, $J_x \equiv I\frac{d\phi}{dx}$, while is the similar in form to the single channel Wigner delay time , $W \equiv I\frac{d\phi}{d\omega}$, but involves the spatial derivative of phase. The theoretical form of $p(J_x)$ [116] obtained by analogy with the one on W for normalized current density $\hat{J}_x \equiv \frac{I}{< I >}\frac{d\phi}{dx}$ as following:

$$p(\hat{J}_x) = \frac{1}{\sqrt{-2b}} \exp\left(\frac{-2|\hat{J}_x|}{\Theta(\hat{J}_x)a + \sqrt{-2b}}\right). \qquad (5-22)$$

Parameters a and b can be calculated from the first and second terms in the

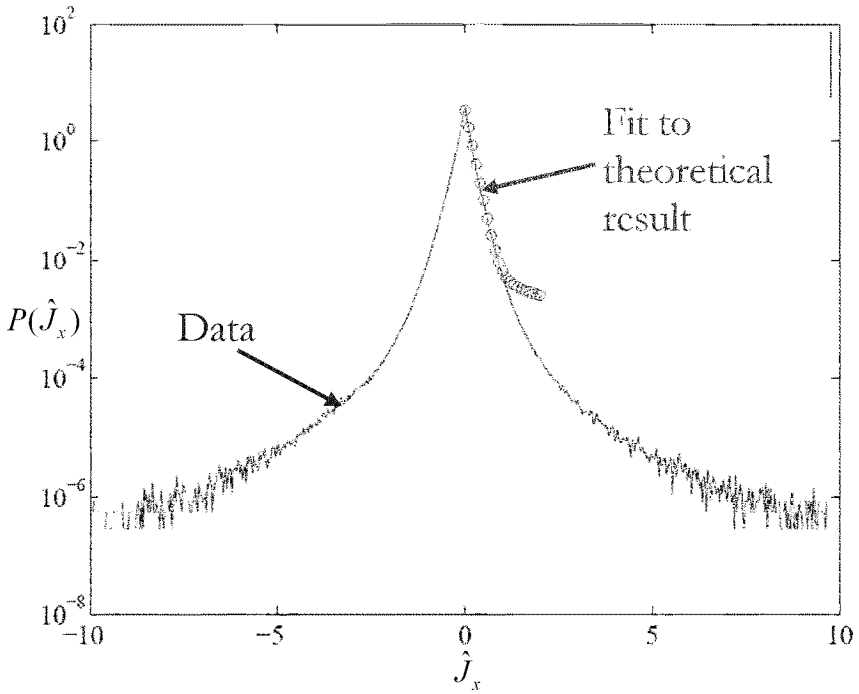

Fig. 5 – 8: The probability distribution of transverse current density $p(\hat{J}_x)$ with spatial resolution 1 mm and the theoretical prediction

Taylor expansion of the field correlation function:

$$C_E(\Delta x) = 1 + ia\Delta x + b(\Delta x)^2 + \mathrm{O}(\Delta x^3), \quad (5-23)$$

which results in $a = <\hat{J}_x>$ and $Q = -2b$ which is the same as Q in Eq.5-18.

Therefore, Eq. 5-22 can be rewritten as:

$$p(\hat{J}_x) = \frac{1}{\sqrt{Q}} \exp\left(\frac{-2|\hat{J}_x|}{\sqrt{Q}}\right). \quad (5-24)$$

Microwave measurements of this probability distribution are shown in Fig. 5-8. In the figure, the fit to the data obtained by applying Eq. 5-24 with Q ~

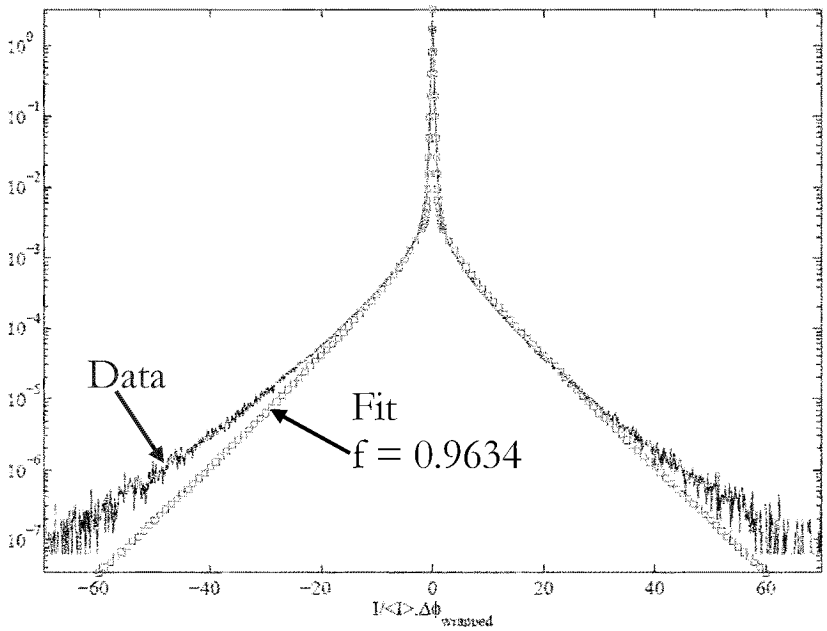

Figure 5 – 9: The probability distribution of transverse current density $p(I\frac{\Delta\phi}{\Delta x})$ with considering the finite translating step.

0.063 is the circle line. Agreement is only down to 10^{-2}.

The numerical calculation of $p(I\frac{\Delta\phi}{\Delta x})$, which is modified by considering the impact of the finite size of Δx, as well as measured $p(I\frac{\Delta\phi}{\Delta x})$ corresponding to wrapping phase are shown in Fig. 5-9 with parameter $C_p(\Delta x = 1.06mm) = 0.964$ applied to the calculation.

Chapter 6

SUMMARY

The main goal of this work was to investigate the statistical character of the field distribution inside and transmitted through random sample to understand the connection between mesoscopic fluctuations, correlations, and wave localization. For this purpose, we developed 1) a one-dimensional random waveguide system allowing us to measure the microwave amplitude and phase inside the sample along the entire length of the waveguide; 2) a microwave field image system to measure the full transmitted speckle pattern at output surface of a quasi-one-dimensional system two orthogonal polarization components. Measurements of field spectra have been carried out with monochromatic incident microwave radiation. We were able to study pulse propagation by Fourier transforming steady-state results into the time domain. Since in real system, impact of ubiquitous absorption intertwines with the impact of localization in steady-state measurements, we explored key aspects of propagation in the time domain and were able to observe the increasing impact of localization separately from the influence of absorption.

After lots of efforts on overcoming technical difficulties of designing the one-dimensional random waveguide system such as optimizing detector

structure to reduce distortion to the system but still pick up sufficient large signal, uniformly improving conductor contact along entire waveguide, the system becomes stable and flexible and allows us to study wave propagation in one-dimensional samples with various arrangements. We have studied 1) the spatial extent of field for Bloch waves and evanescent waves in nearly periodic sample; 2) the spatial extent, linewidth for localized waves in single defect and random samples; 3) the spatially and spectrally overlapping modes which can be decomposed into quasi-normal modes. We studied the relation of these modes to the transmission and impact of absorption. These results suggest that the concept of quasi-normal modes in an open dissipative sample is appropriate even for overlapping modes. When a disordered system exhibiting multiple peaks in the spatial field distribution is modified randomly, level repulsion is observed with the sum of the linewidths of the true coupled modes remaining approximately constant as the separation between the modes changes. We find that modes do not come closer than the linewidths of the modes when they are nearest in frequency. The mechanism for such level repulsion is not yet well understood.

We have presented the results from the measurements of transmitted speckle pattern along a line across the output surface and on a tight grid over the surface: 1) find structures of the spatial intensity correlation function; 2) for a fixed input, organize the intensity correlation function in terms of field

correlation function and single parameter (in steady-state wave propagation and with different time delays; 3) phase statistics such as the probability distributions of phase, phase derivative and transverse current density within speckle pattern; 4) microstatistics in a single speckle pattern and statistics of total transmission. Measurements of full speckle pattern with two polarization components lead to locating phase singularities and polarization singularities. Though the intensity at phase singularity vanishes, the measured fields at points around the singularities are still well defined allowing the phase singularity be accurately located. Since such measurements are extremely time consuming (about three days for each sample realization), the stability of instrument and environment. The temperature fluctuation, sample or cable motions are all of concern.

BIBLIOGRAPHY

[1] P. W. Anderson, Philos. Mag. **52,** 505 (1985).

[2] J. W. Goodman, *Statistical Optics* (John Wiley & Sons, New York, 2000).

[3] S. John, Phys. Rev. Lett. **53,** 2169 (1984).

[4] *Scattering and localization of classical waves in random media*, Vol. Vol. 8 (World Scientific Press, Singapore, 1990).

[5] *Wave and Imaging through complex media*, P. Sebbah ed. (Kluwer Academic Publisher, Dordrecht, 2001).

[6] S. John, Phys. Rev. Lett. **58,** 2486 (1987).

[7] E. Yablonovitch, Phys. Rev. Lett. **58,** 2059-2062 (1987).

[8] *Photonic crystals and light localization in 21st century*, C. Souloulis ed. (Kluwer Academic Publisher, The Netherlands, 2001).

[9] J. D. Joannopoulos, R. D. Mead, and J. N. Winn, *Photonic Crystal: Molding the flow of light* (Princeton Univ. Press, Princeton, 1995).

[10] *Analogies in Optics and Microelectronics*, W. van Haeringen D. Lenstra ed. (North Holland, 1991).

[11] E. Abrahams, P. W. Anderson, D. C. Licciardello, and T. V. Ramakrishnan, Phys. Rev. Lett. **42,** 673 (1979).

[12] P. W. Anderson, Phys. Rev. **109,** 1492 (1958).

[13] D. J. Thouless, Phys. Rev. Lett. **39,** 1167-1169 (1977).

[14] P. A. Lee and T. V. Ramakrishnan, Rev. Mod. Phys. **57,** 287 (1985).

[15] R. A. Webb, S. Washburn, C. P. Umbach, and R. B. Laibowitz, Phys. Rev. Lett. **54,** 2696 (1985).

[16] *Mesoscopic Phenomena in Solids*, Vol. 30 (Elsevier Science & Technology Books, 1991).

[17] B. L. Altshuler and D. E. Khmelnitskii, JETP lett. **42,** 359 (1985).

[18] F. Scheffold and G. Maret, Phys. Rev. Lett. **81,** 5800 (1998).

[19] D. S. Wiersma, P. Bartolini, A. Lagendijk, and R. Righini, Nature **390,** 671 (1997).

[20] E. Akkermans, P. E. Wolf, and R. Maynard, Phys. Rev. Lett. **56,** 1471 (1986).

[21] M. v. Albada and A. Lagendijk, Phys. Rev. Lett. **55,** 2692 (1985).

[22] B. A. v. Tiggelen, D. A. Wiersma, and A. Lagendijk, Europhys. Lett. **30,** 1 (1995).

[23] R. L. Weaver and O. I. Lobkis, Phys. Rev. Lett. **84,** 4942 (2000).

[24] P. E. Wolf and G. Maret, Phys. Rev. Lett. **55,** 2696 (1985).

[25] A. R. Ioffe and A. R. Regel, Prog. Semicond. **4,** 237 (1960).

[26] S. Datta, *Electronic Transport in Mesoscopic systems* (Cambridge University Press, New York, 2001).

[27] M. Janssen, *Fluctuations and localization in mesoscopic electron systems* (World Scientific Publishing Co., 2001).

[28] R. Landauer, Philos. Mag. **21,** 863 (1970).

[29] S. Feng, C. Kane, P. A. Lee, and A. D. Stone, Phys. Rev. Lett. **61,** 834 (1988).

[30] M. C. W. v. Rossum and T. M. Nieuwenhuizen, Review of Modern Physics **71,** 313-371 (1999).

[31] A. Lagendijk and B. A. v. Tiggelen, Phys. Rep. **270,** 143 (1996).

[32] F. Scheffold, R. Lenke, R. Tweer, and G. Maret, Nature **389,** 206 (1999).

[33] A. A. Chabanov and A. Z. Genack, Phys. Rev. Lett. **87,** 153901 (2001).

[34] R. Dalichaouch, J. P. Armstrong, S. Schultz, P. M. Platzman, and S. L. McCall, Nature **354,** 53 (1991).

[35] A. A. Chabanov, M. Stoytchev, and A. Z. Genack, Nature **404,** 850 (2000).

[36] A. Z. Genack, Europhys. Lett. **11,** 733 (1990).

[37] P. W. Anderson, D. J. Thouless, E. Abrahams, and D. S. Fisher, Phys. Rev. B **22,** 3519 (1980).

[38] E. Kogan and M. Kaveh, Phys. Rev. B **52,** R3813 (1995).

[39] T. M. Nieuwenhuizen and M. C. M. v. Rossum, Phys. Rev. Lett. **74,** 2674 (1995).

[40] M. Stoytchev and A. Z. Genack, Phys. Rev. Lett. **79,** 309-312 (1997).

[41] A. A. Chabanov, A. Z. Genack, N. Tregoures, and B. A. v. Tiggelen, Phys. Rev. Lett. **92,** 173902 (2004).

[42] A. A. Chabanov, B. Hu, and A. Z. Genack, Phys. Rev. Lett. **93,** 123904 (2004).

[43] P. Sebbah, B. Hu, A. Z. Genack, R. Pnini, and B. Shapiro, Phys. Rev. Lett. **88,** 123901 (2002).

[44] S.-H. Chang, A. Taflove, A. Yamilov, A. Burin, and H. Cao, Opt. Lett. **29,** 917 (2004).

[45] J. W. Goodman, in *Laser Speckle and Related Phenomena*, edited by J. C. Dainty (Springer-Verlag, Berlin, 1984).

[46] B. Shapiro, Phys. Rev. Lett. **57,** 2168 (1986).

[47] I. Freund and D. Eliyahu, phys. Rev. A **45,** 6133 (1992).

[48] M. J. Stephen and G. Cwilich, Phys. Rev. Lett. **59,** 285 (1987).

[49] U. Kuhl and H.-J. Stockmann, Physica E **9,** 384 (2001).

[50] P. E. Shibaev, V. I. Kopp, and A. Z. Genack, J. Phys. Chem. B **107,** 6961 (2003).

[51] M. V. Berry and S. Klein, Eur.J. Phys **18,** 222 (1997).

[52] V. Milner and A. Z. Genack, Phys. Rev. Lett. **94,** 073901 (2005).

[53] J. Bertolotti, S. Gottardo, D. S. Wiersma, M. Ghulinyan, and L. Pavesi, Phys. Rev. Lett. **94,** 113903 (2005).

[54] C. W. J. Beenakker, Rev. Mod. Phys. **69,** 731-808 (1997).

[55] A. D. Stone, P. A. Mello, K. A. Muttalib, and J. L. Pichard, in *Mesoscopic Phenomena in Solid* (North Holland, Amsterdam, 1991).

[56] A. Z. Genack, A. A. Chabanov, B. Hu, Z.-Q. Zhang, and P. Sebbah, in *Electromagnetic fluctuations, correlations and localization in the time domain*, 2005.

[57] P. Sebbah, B. Hu, J. M. Klosner, and A. Z. Genack, in *Quasimode expansion of spatially extended field distributions with nominally localized random wave*, 2006.

[58] P. Sebbah, B. Hu, A. A. Chabanov, and A. Z. Genack, in *Statistics of the near-field speckle pattern in transmission through random media*, 2005.

[59] S. Noda, A. Chutinan, and M. Imada, Nature **407,** 608 (2000).

[60] O. J. Painter, Science **284,** 1819 (1999).

[61] P. R. Villeneuve, S. Fan, and J. D. Joannopoulous, Phys. Rev. B **54,** 7837 (1996).

[62] M. Y. Azbel, Phys. Rev. B **28,** 4106 (1983).

[63] N. F. Mott, Philos. Mag. **22,** 7 (1970).

[64] J. B. Pendry, J. Phys. C **20,** 733 (1987).

[65] J. B. Pendry, Adv. Phys. **43,** 461 (1994).

[66] H. S. Sozuer and J. P. Dowling, J. Mod. Opt. **41,** 231 (1994).

[67] H. S. Sozuer and J. W. Haus, J. Opt. Soc. Am. B **10,** 296 (1993).

[68] E. Yablonovitch and K. M. Leung, Physica B **175,** 81 (1991).

[69] P. J. Dowling and C. M. Bowden, Phys. Rev. A **46,** 612 (1992).

[70] E. S. C. Ching, P. T. Leung, A. M. v. d. Brink, W. M. Suen, S. S. Tong, and K. Young, Rev. Mod. Phys. **70,** 1545 (1998).

[71] U. Kuhl, H.-J. Stockman, and R. Weaver, J. Phys. A: Math. Gen. **38,** 10433 (2005).

[72] P. Mello, E. Akkermans, and B. Shapiro, Phys. Rev. Lett. **61,** 459 (1988).

[73] M. B. v. d. Mark, M. P. v. Albada, and A. D. Lagendijk, Phys. Rev. B **37,** 3375 (1988).

[74] P. A. Lee and A. D. Stone, Phys. Rev. Lett. **55,** 1622 (1985).

[75] N. Garcia, A. Z. Genack, R. Pnini, and B. Shapiro, Phys. Lett. A **176,** 458 (1993).

[76] A. Z. Genack and J. M. Drake, Europhys. Lett. **11,** 331 (1990).

[77] R. Pnini and B. Shapiro, Phys. Rev. B **39,** 6986 (1989).

[78] A. Z. Genack, J. H. Li, N. Garcia, and A. A. Lisyansky, in *Photonic Band Gap and Localization* (Plenum Press, New York, 1993), p. 23.

[79] P. Sebbah, R. Pnini, and A. Z. Genack, PHys. Rev. E **62,** 7348 (2000).

[80] I. Freund, M. Keveh, R. Berkovits, and M. Rosenbluh, Phys. Rev. B **42,** 2613 (1990).

[81] A. Z. Genack, J. H. Li, N. Garcia, and A. A. Lisyansky, in *Photonic Gand Gaps and Localization* (Plenum Press, New York, 1993), p. 23.

[82] R. Pnini, in *Waves and Imaging through complex media* (Kluwer Academic Publishers, Dordrecht, 2001), p. 391-412.

[83] E. Kogan and M. Kaveh, phys. Rev. B **45** (1992).

[84] A. A. Chabanov and A. Z. Genack, Phys. Rev. E **72,** 055602 (2005).

[85] P. Sheng, *Scattering and localization of classical waves in random media*, Vol. Vol. 8 (World Scientific Press, Singapore, 1990).

[86] *Mesoscopic Phenomena in Solids*, B.L. Altshuler, P.A. Lee, and R.A. Webb ed. (North Holland, Amsterdam, 1991).

[87] R. Weaver, J. Burkhardt, and J. Acoust, Soc. Am. **96,** 3186 (1994).

[88] M. Titov and C. W. J. Beenakker, Phys. Rev. Lett. **85,** 3388 (2000).

[89] S. E. Skipetrov and B. A. v. Tiggelen, Phys. Rev. Lett. **92,** 113901 (2004).

[90] H. Schomerus, K. J. H. v. Bemmel, and C. W. J. Beenakker, Phys. Rev. E **63,** 026605 (2001).

[91] V. N. Prigodin, B. L. Altshuler, K. B. Efetov, and S. Iida, Phys. Rev. Lett. **72,** 546 (1994).

[92] B. A. Muzykantskii and D. E. Khmelnitskii, Phys. Rev. B **51,** 5480 (1995).

[93] A. D. Mirlin, Phys. Rep. **326,** 259 (2000).

[94] M. Haney and R. Snieder, Phys. Rev. Lett. **91,** 093902 (2003).

[95] S. K. Cheung, X. Zhang, Z. Q. Zhang, A. A. Chabanov, and A. Z. Genack, Phys. Rev. Lett. **92,** 173902 (2004).

[96] A. A. Chabanov, Z. Q. Zhang, and A. Z. Genack, Phys. Rev. Lett. **90,** 203903 (2003).

[97] Z. Q. Zhang, S. K. Cheung, X. Zhang, A. A. Chabanov, and A. Z. Genack, Math. and Appl. of Analysis (2004).

[98] A. A. Chabanov and A. Z. Genack, in *Wave Scattering in Complex Media*, edited by B. A. v. Tiggelen and S. E. Skipetrov (Kluwer, Dordrecht, 2003).

[99] J. M. Drake and A. Z. Genack, Phys. Rev. Lett. **63,** 259 (1989).

[100] R. H. J. Kop, P. deVries, R. Sprik, and A. Lagendijk, Phys. Rev. Lett. **79,** 4369 (1997).

[101] G. H. Watson, P. A. Fleury, and S. L. McCall, Phys. Rev. Lett. **58,** 945 (1987).

[102] K. M. Yoo, F. Liu, and R. R. Alfano, Phys. Rev. Lett. **64,** 2647 (1990).

[103] M. Stoytchev and A. Z. Genack, Opt. Lett. **24,** 262 (1999).

[104] A. A. Chabanov and A. Z. Genack, Phys. Rev. Lett. **87,** 233903 (2001).

[105] P. Sebbah, O. Legrand, B. A. v. Tiggelen, and A. Z. Genack, Phys. Rev. E **56,** 3619 (1997).

[106] J. H. Page, M. L. Cowan, and D. A. Weitz, in *Wave scattering in complex media*.

[107] F. T. Smith, Phys. Rev. **98,** 145 (1955).

[108] G. Iannacone, Phys. Rev. B **51,** 4727 (1995).

[109] P. Sebbah, O. Legrand, and A. Z. Genack, Phys. Rev. E **59,** 2406 (1999).

[110] B. A. van Tiggelen, P. Sebbah, M. Stoytchev, and A. Z. Genack, Phys. Rev. E **59,** 7166 (1999).

[111] P. Seba, U. Kuhl, M. Barth, H. J. Stockmann, and J. P. Bird, J. Phys. A: Math. Gen. **32,** 8225 (1999).

[112] U. Frish, *Probabilistic Methods in Applied Mathematics vol. 1*, A. T. Barucha-Reid ed. (Academic, New York, 1968).

[113] I. Freund and N. Shvartsman, Phys. Rev. E **51,** 3770 (1995).

[114] Papoulis, *Probability, Random variable, and Stochastic processes* (McGraw-Hill, New York, 1965).

[115] K. J. Ebeling, Opt. Acta **26,** 1505 (1979).

[116] B. v. Tiggelen. (personal communication)